Polyelectrolyte domains in intrinsically disordered regions differentially regulate intracellular biomolecular condensation

Yoon Jeong Choi[1,2,3], Yujin Lee[1,6], Soojin Cho[1,6], Yaqi Pan [1,6], Yemuk Kang[1,6], Changi Pack[4,5], Youngtae Jeong[2,3], and Kiwon Song[1,*]

[1]Department of Biochemistry, College of Life Science and Biotechnology, Yonsei University, Seoul 03722, Republic of Korea

[2]Department of New Biology, DGIST, Daegu, 43014, Korea

[3]New Biology Research Center, DGIST, Daegu, 43014, Korea

[4]Department of Biomedical Engineering, University of Ulsan College of Medicine, Seoul 05505, South Korea

[5]Convergence Medicine Research Center, Asan Institute for Life Sciences, Asan Medical Center, Seoul 05505, South Korea

[6]These authors contributed equally.

*Correspondence: bc5012@yonsei.ac.kr

SUMMARY

Intracellular condensation is a hallmark of many proteins containing intrinsically disordered regions (IDRs). Decoding the regulatory mechanisms of condensation encoded within the amino acid sequences of condensate-forming proteins is essential for understanding both how intracellular condensates assemble and how they contribute to various disease pathologies. Here, we investigated the budding yeast P-body proteins Nst1 and Edc3, which exhibit pronounced intracellular self-condensation, and identified charged amino acid clusters in the low complexity regions (LCRs) that modulate their phase behavior. Guided by the stickers-and-spacers framework, we hypothesized that clusters of charged residues within IDRs

function in promoting intracellular condensation process. Using a sliding-window approach, we designated and dissected the polyelectrolyte (PE) domains of Nst1 and Edc3 and established their essential contributions to condensate coalescence. In Nst1, the polyanionic (PA) subdomain enhances intermolecular attraction and promotes coalescence, whereas the polyampholyte (PAM) subdomain imparts rigidity to the condensate as a distinct modulatory element and functions as a platform in condensation process of other P-body components. PA of Edc3 also regulates coalescence. Extending these findings to the neurodegenerative disease-associated protein TDP-43, we show that its PA regions are critical for coalescence, consistent with the presence of negatively charged amino acid clusters as potent molecular stickers functioning in condensate coalescence in cells. These results highlight charged-residue clusters as important sequence determinants of protein phase behavior and suggest that they represent promising novel regulatory targets for modulating TDP-43 condensation in cells.

KEYWORDS

biomolecular condensates, intrinsically disordered region (IDR), stickers and spacers model, polyelectrolyte, coalescence, polyampholyte, polyanion, P-body, Nst1, Edc3, TDP-43

INTRODUCTION

Biomolecular condensation observed in cells not only deepens our understanding of molecular dynamics in response to various physiological conditions, but also shed light on the mechanisms underlying protein amyloid formation (Alberti and Hyman, 2021; Alshareedah et al., 2024; Banani et al., 2017; Niu et al., 2023). These condensations occur within the crowded and complex cellular environment, exhibiting diverse physical properties depending on the degree of condensation.

Among these behaviors, liquid-like demixing has been extensively studied as one prominent mechanism of condensate formation, in which dynamic, droplet-like assemblies are distinguished from more rigid, amyloid-like protein aggregates (Ranganathan et al., 2022). Neurodegeneration-associated proteins usually act as scaffolds that drive the formation of liquid-like condensates with self-condensation ability and

high multivalency. Recent studies have increasingly reported the co-occurrence of amyloid fibrils and liquid-like condensates of pathogenic proteins, such as TDP-43, both in the brain tissues of patients with neurodegenerative diseases and in cellular models of these diseases (Ahmad et al., 2022; Alshareedah *et al.*, 2024; Gruijs da Silva et al., 2022; Sneideriene et al., 2025). This observation strongly suggests that the aggregation of pathogenic proteins does not proceed through direct solid aggregation, but rather through prior enrichment into liquid-like condensates, followed by a structural conversion into amyloid assemblies. In other words, dysregulation of these liquid-like condensates is expected to promote the formation of protein amyloids implicated in neurodegenerative disorders (Hurtle et al., 2023; Nam and Gwon, 2023; Visser et al., 2024). Therefore, elucidating the underlying mechanisms of liquid-like condensation is critical both for understanding the molecular dynamics underlying physiological condensate formation, and for discovering therapeutic strategies to regulate pathological condensate formation (Alberti and Hyman, 2021; Choi et al., 2024; Gao et al., 2023; Lu et al., 2024; Mehta and Zhang, 2022).

Stickers-and-spacers model is a leading framework of a molecular mechanism for biomolecular liquid-like condensation (Banjade and Rosen, 2014; Choi et al., 2020; Sood and Zhang, 2024). This model defines “stickers” as molecular elements that mediate attractive interactions, and “spacers” as flexible linkers that separate stickers and modulate condensate properties (Choi *et al.*, 2020). Amino acids in intrinsically disordered regions (IDRs), capable of functioning as stickers, were precisely identified through *in vitro* studies. The cation-π interaction between tyrosine and arginine, as well as the interaction between lysine and RNA, were revealed to act as stickers (Ukmar-Godec et al., 2019; Wang et al., 2018b). The sequential pattern of these components significantly influences the dynamic characteristics of the condensate (Alshareedah *et al.*, 2024; Alshareedah et al., 2021; Wang *et al.*, 2018b). Notably, when sticker amino acids are clustered within the sequence, rather than dispersed, the resultant condensate tends towards solidification (Alshareedah *et al.*, 2024; Alshareedah *et al.*, 2021; Wang *et al.*, 2018b). Thus, the stickers-and-spacers model offers a solid basis for elucidating the condensation characteristics of molecules *in vitro*, offering valuable insights into the behavior of biomolecular condensates.

Despite the explanatory power of the stickers-and-spacers model, the molecular grammar underlying intracellular biomolecular condensation remains enigmatic. First, the morphology and physical properties of condensates depend on the characteristics of condensate-forming proteins and the intracellular

80 environment, and these properties can change over time as condensation progresses. Thus, the stickers
81 that function may vary depending on the phase of condensates. Second, although the molecular grammar
82 of condensation has been extensively characterized for prion-like low-complexity domains (PLCDs) - such
83 as poly Q/N tracts in yeast amyloidogenic proteins and the RGG motifs in disease-related proteins like FUS
84 and TDP-43 (Patel et al., 2015; Sanders et al., 2020; Wang et al., 2018), other intrinsically disordered
85 regions (IDRs) with distinct combinations of sticker amino acids remain largely unexplored. Critically, many
86 IDRs lack canonical PLCD features but still drive phase separation, suggesting the existence of alternative
87 molecular grammars.

88 Recent *in vitro* and simulation studies have reported that the charge distribution within amino acid
89 sequences strongly affects the viscosity, surface tension, and dynamic properties of condensates (Biswas
90 and Potoyan, 2024; Linsenmeier et al., 2023; Sundaravadivelu Devarajan et al., 2024). These reports
91 strongly indicate the need for research on the regulation of cellular condensation process by novel low
92 complexity regions (LCRs) composed of sticker amino acids such as charged amino acid clusters, in
93 addition to the previously studied PLCDs.

94 In this study, we aimed to elucidate the role of the polyelectrolyte region in the cellular condensation of
95 biomolecules via Nst1. Both Nst1 and Edc3, established P-body components in budding yeast, possess
96 intrinsic self-condensation capabilities. Upon Nst1 and Edc3 overexpression, cells initially exhibit numerous
97 small condensates of Nst1 and Edc3, which progressively fuse into larger structures as protein levels
98 accumulate over time, thereby reducing the overall number of observed condensate (Fig. 1A). Utilizing this
99 model, we examined how the polyelectrolyte region affects both the molecular dynamics of NST1
100 condensates and the condensate formation of P-body components mediated by NST1. Furthermore, we
101 investigated whether the function of the polyelectrolyte region in Nst1 condensation could be extrapolated
102 to TDP-43, a stress granule constituent that is closely linked to the pathology of neurodegenerative
103 diseases.

104

105 **RESULTS**

106 ***Overexpression of Nst1 and Edc3 leads to mature condensate formation, whereas overexpression***
107 ***of their polyelectrolyte (PE) domain deletion mutants within the IDR maintains stabilized***
108 ***microphase-separated state***
109

110 In our previous study, we reported that GFP-tagged Nst1 and Edc3, when overexpressed under the
111 control of the GAL promoter, formed condensates that were larger and denser than those formed by Dcp2
112 or Dhh1 (Choi et al., 2022). Here, we monitored the formation dynamics of these condensates from the
113 early phase of Nst1 and Edc3 overexpression until their intracellular expression levels reached saturation
114 (Fig. 1A). Numerous small condensates—here referred to as microphase-separated condensates—began
115 to appear simultaneously throughout the cell as early as 1 hour after galactose induction and were observed
116 in nearly all cells by 2 hours. When we analyze the mean integrated density and the number of condensates
117 of each cell at 4 hours post-induction, the number of condensates per cell had decreased, while their internal
118 density had increased markedly, indicative of a transition to a mature condensate state (Fig. 1B). These
119 observations suggest that microphase Nst1 condensates progressively undergo coalescence as the
120 intracellular concentration of Nst1 rises.

121 Next, we confirmed this distinctive self-condensation potential of Nst1 and Edc3 through analysis of puncta
122 formation patterns in correlation with cytoplasmic protein concentration (Fig. 1C-D). Each protein exhibits
123 a distinct critical concentration for condensation, and a lower critical concentration indicates a higher
124 potential for molecular condensation. By measuring the cytoplasmic concentration of proteins and
125 correlating it with the degree of puncta formation (microphase separation, mature condensates), we can
126 compare condensation patterns between proteins under cellular conditions. Using a galactose promoter,
127 GFP-tagged P-body components such as Nst1, Edc3, Dcp2, and Dhh1, along with the stress granule
128 component Pab1, were overexpressed for 4 hours. Afterward, the cytoplasmic concentration of the
129 overexpressed proteins and the degree of self-condensation were measured using fluorescence correlation
130 spectroscopy (FCS) (Fig.1 A, C-D). We classified the patterns of puncta formation into three categories:
131 diffuse state, microphase separation, and mature condensates (Fig. 1A). GFP control did not exhibit puncta
132 formation at any measured cytoplasmic concentration, whereas Nst1 and Edc3 demonstrated mature

133 condensates at remarkably low concentrations (Fig. 1C-D). Another P-body component, Dcp2 and Dhh1,
134 exhibited microphase separation at higher cytoplasmic concentrations than the concentrations required for
135 mature condensate formation by Nst1 and Edc3. However, mature condensates similar to those observed
136 with Nst1 and Edc3 were not detected for Dcp2 and Dhh1 (Fig. 1C-D). These results confirm that, compared
137 to Dcp2 and Dhh1, Nst1 and Edc3 have a greater intrinsic propensity for self-condensation in cells, which
138 indicates their intrinsic potential for condensation.

139 Next, we hypothesized that a particular charged-amino acid cluster within intrinsically disordered regions
140 (IDRs) in Nst1 protein sequence may function as a "sticker" domain during condensate formation. In our
141 previous study, we identified that PAM (polyampholyte domain, previously described as PD), a segment of
142 a charged-amino acid cluster in Nst1, functions in the condensation of other P-body components in cells
143 overexpressing Nst1 (Choi *et al.*, 2022). However, Nst1 has extended charged amino acid regions beyond
144 PAM. We systematically searched for polyelectrolyte-like clusters of charged amino acids in the IDRs of
145 Nst1 and Edc3 using a sliding window approach, as described in Supplementary Figure 1E (Fig. 1E).
146 Charged amino acids (K, R, H, D, E) were classified, and their proportion within each window was calculated
147 to generate a scoring system. Subsequently, a density plot of charged amino acids was created based on
148 their positions within the sequence (Fig. 1E, S1, S2). Using this method, we segmented polyelectrolyte (PE)
149 amino acid sequence regions spanning residues 65–205 in Edc3 and 460–752 in Nst1 (Fig. 1F, S1, S2).

150 Then, we generated deletion mutant clones of Nst1ΔPE and Edc3ΔPE, overexpressed each protein, and
151 observed the cells after 4 hours of induction. Consistent with previous findings, overexpression of Nst1
152 deleted with the aggregation prone domain (APD), Nst1ΔAPD, did not result in condensate formation (Choi
153 *et al.*, 2022) even at cytoplasmic concentrations comparable to those where wild-type Nst1 forms
154 condensates (Fig. 1G-J). Interestingly, cells overexpressing the PE deletion mutants of both Nst1 and Edc3
155 exhibited microphase separation, even when their cytoplasmic concentrations were comparable with those
156 of wild type Nst1 and Edc3 (Fig. 1G-J). To rule out insufficient expression or time as the cause of
157 microphase separation, we extended the culture to 24 hours in galactose medium. However, even after
158 prolonged induction, both Nst1ΔPE and Edc3ΔPE failed to form mature condensates and continued to
159 exhibit microphase separation (Fig. 1G, H). These results indicate that each polyelectrolyte (PE) is

160 necessary for the coalescence of both Nst1 and Edc3 condensates, thereby facilitating the formation of
161 mature condensates of Nst1 and Edc3.

162

163 ***Polyanion (PA) domain of the Polyelectrolyte (PE) region specifically promotes the coalescence of***
164 ***Nst1 condensates, whereas the polyampholyte (PAM) domain in the PE region does not.***

165

166 Since the PE region of Nst1 exhibits a unique pattern of charged amino acid arrangement compared to
167 the PE region of Edc3, the PE region of Nst1 was further characterized. Analysis of the Nst1 PE region
168 using FELLS (http://protein.bio.unipd.it/fells/ BioComputing UP) revealed two distinct segments: a
169 polyanion (PA) region spanning residues 460–631, a cluster consisting of remarkably high proportion of
170 negatively charged amino acids, and a polyampholyte (PAM) domain spanning residues 632–752 (Fig. 2
171 A, B). In our previous study, we reported that the PAM domain (PD in the previous report) is required for
172 promoting the condensation of other P-body components such as Dcp2 and Dhh1, which is induced by
173 Nst1 condensation, but does not affect the self-condensation of Nst1 (Choi *et al.*, 2022).

174 To validate whether the effects of PE on Nst1 condensation were specifically due to the PA domain, we
175 observed the time-dependent pattern of puncta formation of each GFP-tagged Nst1 domain deletion mutant
176 in *Δnst1* cells. When overexpressed for 1 hour using the galactose induction system, the wild-type Nst1
177 (Nst1 full-length, F.L.), Nst1ΔPA, Nst1ΔPAM, and Nst1ΔPE all exhibited microphase separation (Fig. 2C).
178 After 4 hours of induction, wild-type Nst1 and Nst1ΔPAM exhibited mature condensates with a reduced
179 number of puncta per cell, indicating that the numerous small puncta observed after 1 hour of induction
180 coalesced into fewer, larger puncta as the cytoplasmic concentration increased over time. (Fig. 2C).
181 However, cells overexpressing Nst1ΔPA and Nst1ΔPE failed to undergo coalescence, and showed an
182 increased number of puncta and decreased signal intensities compared to cells overexpressing wildtype
183 Nst1 and Nst1ΔPAM (Fig. 2C). Even after 24 hours of induction, wild-type Nst1 and Nst1ΔPAM formed
184 mature condensates with intense fluorescence signals (Fig. 2C). However, cells expressing Nst1ΔPA and
185 Nst1ΔPE did not show a reduction in puncta number, although some puncta increased in size and intensity
186 compared to those observed after 4 hours of induction (Fig. 2C). This result indicates that PA domain is

187 essential for coalescence of Nst1 condensates. Since several mutations in a protein can alter the physical
188 property of condensates (Banani et al., 2022; Sanfeliu-Cerdan et al., 2023), we also determined whether
189 these condensates exhibit liquid-like or amyloid-like characteristics. Cells overexpressing each domain
190 deletion mutant for 4 hours were treated with 1,6-hexanediol for 1 hour, then observed. Most puncta
191 generated by each mutant dispersed upon treatment, indicating that none of the domains significantly alters
192 the liquid-like properties of these condensates (Fig. 2D).

193 To evaluate the condensation potential of each domain deletion mutant, we measured the protein
194 concentrations associated with each intracellular puncta formation pattern for each Nst1 variant after 4
195 hours of induction by FCS (Fig. 2E). Cells expressing GFP or Nst1ΔAPD remained diffuse, whereas cells
196 expressing Nst1ΔPA or Nst1ΔPE exhibited microphase separation without forming mature condensates,
197 despite having cytoplasmic protein concentrations comparable to those of wild-type Nst1 and Nst1ΔPAM
198 (Fig. 2E).

199 When we initially constructed the Nst1ΔPA mutant, positively charged amino acids near the C-terminal
200 portion of the defined PA region were included in the deletion. To better distinguish the function of negatively
201 charged clusters within this region, we generated an additional mutant called Nst1ΔPA-1 that excluded
202 positively charged amino acids from deletion while maintaining the integrity of the negatively-charged
203 domain within PA. Consistently, cells overexpressing Nst1ΔPA-1 displayed numerous micro-condensates
204 from 1hour to 24 hours induction, similar to cells overexpressing Nst1ΔPA (Fig. S4). These findings indicate
205 that the overexpression phenotype observed in Nst1ΔPA is due to the polyanion located within the PA
206 region.

207 Next, we investigated whether the results from the Nst1 domain deletion mutants could be applied in
208 condensate formation of endogenous Nst1. Since endogenously expressed Nst1 forms condensates from
209 diauxic shift to stationary phase (Fig. 2F), we examined the puncta generation patterns by condensation of
210 endogenously expressed full-length Nst1, the Nst1ΔPA, the Nst1ΔPAM, and the Nst1ΔAPD from early log
211 phase to stationary phase (Fig. 2F).

212 We cultured cells expressing the chromosome-integrated GFP-tagged versions of each domain deletion
213 mutant under the control of the endogenous Nst1 promoter in a *Δnst1* strain and observed them at 16, 30,

214 48, and 80 hours after seeding at an initial OD_{600} = 0.1 (Fig. 2G). These mutants exhibited similar puncta
215 generation patterns to those observed in cells overexpressing these deletion mutants. Endogenously
216 expressed Nst1ΔAPD formed few condensates, confirming that the aggregation-prone region, which is
217 critical for hydrophobic core assembly, is essential for condensate formation (Fig. 2H-I). Among the tested
218 mutants, Nst1ΔPA was the first to initiate condensation, starting at 10 hours during the early log phase (Fig.
219 2H-I), and notably during the mid-log phase (14–18 hours). While the wild-type Nst1 and other mutants had
220 not yet begun puncta formation, Nst1ΔPA condensates increased significantly (Fig. 2H-I). After 18 hours,
221 condensation began for the full-length Nst1 and Nst1ΔPAM. Interestingly, starting at 22 hours, as cells
222 entered the stationary phase, the intensity of Nst1ΔPAM condensates were markedly higher than those of
223 the wild-type Nst1 and Nst1ΔPA condensates (Fig. 2I). At 46 hours, during the stationary phase, we
224 observed that the intensities of Nst1ΔPA condensates were lower than those of wild-type Nst1 and
225 Nst1ΔPAM condensates (Fig. 2J). Together, these findings demonstrate that the differential propensities
226 for condensate formation observed among mutants in overexpression experiments are also recapitulated
227 under physiological conditions.
228
229 ***Polyanion (PA) domain exclusively functions in coalescence of Nst1 condensates.***
230

231 Next, we investigated whether the contribution of the PA domain to Nst1 condensation is unique to the PA
232 region, or whether other sequence regions of similar size can also play a similar role, thereby assessing
233 potential non-specific effects arising from deletions of comparable regions. To clarify this, we generated
234 five additional domain deletion mutants of similar size as the PA domain in Nst1: Nst1ΔD1$^{2\text{-}122}$, Nst1ΔD2$^{123\text{-}}$
235 ^{293}, Nst1ΔD3$^{294\text{-}459}$, Nst1ΔD4$^{753\text{-}844}$, Nst1ΔD5$^{845\text{-}1015}$ (Fig. 3A). The *Δnst1* w303a cells were transformed with
236 plasmids that can overexpress each GFP-tagged Nst1 domain deletion mutant (D1~D5). All strains were
237 induced with galactose and observed over time using a fluorescence microscope at specified time points
238 after the induction (Fig. 3B).

239 Except the Nst1ΔAPD deletion mutant, the overexpression of D1~D5 deletion mutants began to induce
240 condensates approximately 1 hour after galactose induction (Fig. 3B). Similar to the Nst1ΔPAM (Fig. 2C,

241 3B), the condensates of the deletion mutants from D1 to D5, increased in size as the number of
242 condensates per cell decreased, except for the Nst1ΔPA (Fig. 3B). When cytoplasmic protein
243 concentrations were measured by FCS after 4 hours of induction, Nst1ΔPA exhibited microphase
244 separation at all measured concentrations, whereas all other mutants formed mature condensates at similar
245 cytoplasmic concentrations (Fig. 3C). Even after 24 hours of induction, Nst1ΔPA failed to generate mature
246 condensates, while all the other mutants, ΔD1 to ΔD5, successfully formed mature condensates (Fig. 3B).
247 These results further support that the PA region of Nst1 plays a unique and critical role in driving condensate
248 coalescence during biomolecular condensation.

249

250 ***The polyanion (PA) domain of Nst1 enhances intermolecular interaction within condensates,***
251 ***whereas the polyampholyte (PAM) domain of Nst1 increases the rigidity of Nst1 condensates.***

252

253 Next, we examined whether the PA and PAM domains influence the dynamics of Nst1 condensates by
254 employing fluorescence recovery after photobleaching (FRAP). Since the condensates of the
255 overexpressed Nst1ΔPA did not coalescence and retained minimal puncta size, the abnormal function in
256 the coalescence process is likely related to the molecular dynamics affected by the PA domain deletion.

257 We examined GFP-tagged the full-length Nst1, as well as the Nst1ΔPA, Nst1ΔPAM, and Nst1ΔD1
258 mutants, with GFP control after 4 hours of induction (Fig. 4A). Condensates from each mutant were imaged,
259 photobleached, and fluorescence recovery was monitored over time (Fig. 4B). Prior to be analyzed,
260 recovery curves from each mutant FRAP analysis were fitted and normalized (Fig. 4C-D, S6 A-E). Because
261 molecular dynamics can be affected by molecular size (Pack, 2021), the Nst1ΔD1 mutant was also used
262 as a size control for the analyses of Nst1ΔPA and Nst1ΔPAM.

263 We measured the maximal recovery velocity and recovery half-life for each Nst1 domain deletion mutant
264 (Fig. 4C, F-G). The maximal recovery velocity represents the rate at which unbleached fluorescent
265 molecules exchange with bleached molecules within puncta; a lower maximal recovery velocity indicates
266 stronger intermolecular interactions within condensates, while a higher velocity suggests weaker

267 interactions and increased molecular dynamics. The recovery half-life reflects the time required for
268 fluorescence in the bleached region to reach half of its maximum equilibrium intensity, serving as an
269 additional measure of molecular dynamics.

270 The full-length Nst1 exhibited the slowest and lowest maximal recovery velocity among all samples,
271 whereas the PAM-, PA-, and D1-deleted mutants recovered more rapidly (Fig. 4D-F), indicating that
272 molecules with smaller molecular weight are generally more dynamic in the condensates. Notably, Nst1ΔPA
273 puncta showed the fastest maximal recovery velocity among all deletion mutants (Fig. 4F). In contrast, the
274 maximal recovery velocity and half-life of Nst1ΔPAM were comparable to those of Nst1ΔD1 (Fig. 4F-G).
275 These results suggest that Nst1ΔPA exhibits particularly increased molecular dynamics due to weaker and
276 less stable intermolecular interactions compared to Nst1ΔPAM and Nst1ΔD1.

277 Regarding mobile fraction as area under curve (AUC, %), the full-length Nst1 had the lowest AUC
278 compared with these Nst1 deletion mutant proteins (Fig. 4E). The AUC of the Nst1Δ PAM was significantly
279 higher than those of the Nst1ΔPA and Nst1ΔD1 (Fig. 4H). This indicates that puncta formed by Nst1ΔPAM
280 have a higher proportion of mobile fractions compared to those formed by Nst1ΔPA and Nst1ΔD1. This
281 suggests that the PAM domain of Nst1 enhances the rigidity of Nst1 condensates.

282 Overall, our results strongly suggest that polyampholyte (PAM) deletion weakens cohesion of internal
283 networks, increasing overall molecular mobility within the condensate, while the polyanion (PA) deletion
284 specifically enhances single-molecule dynamics by reducing electrostatic molecular affinity. That is,
285 polyanions might participate in intermolecular interactions, enforcing molecular affinity, while
286 polyampholytes contribute to restricting the movement of molecules in the confined state within
287 condensates. These results highlight how different charged domains contribute uniquely to condensate
288 properties and molecular behavior.

289

290 ***The PAM domain is an RNA-independent multivalent interaction domain for interaction with a P-***
291 ***body component, Dcp2.***

292

293 In our previous study, we found that overexpression of Nst1 induces the formation of Nst1 condensates,
294 which simultaneously promote the condensation of other P-body components, including Dcp2 (Choi *et al.*,
295 2022). We suggested that the PAM domain, previously described as PD, is a multivalent interaction region
296 responsible for the condensation of P-body components such as Dcp2 (Choi *et al.*, 2022).

297 Since the function of PAM domain was resolved by measuring endogenously expressing GFP-tagged
298 Dcp2, Dhh1, and Xrn1 in cells overexpressing non-tagged Nst1 variants (Choi *et al.*, 2022), we need to
299 confirm the function of PAM domain using a direct approach that can elucidate its role in inducing Dcp2
300 condensation. We utilized the chromosomally mKate2-tagged Dcp2 strain overexpressing GFP-tagged
301 Nst1 variants, including Nst1ΔPAM, Nst1ΔPA, and Nst1ΔD1. The cells were induced to generate
302 condensates of each Nst1 variant by 4 hour-overexpression, then treated with cycloheximide which binds
303 to the ribosomal A site and inhibits translation elongation, resulting in decrease of free RNA level
304 (Schneider-Poetsch et al., 2010). The reduction of the cytoplasmic concentration of free RNA, thereby
305 eliminates Dcp2 condensates that are formed by free RNA (Teixeira et al., 2005; Van Treeck and Parker,
306 2018). With this strategy, the majority of Dcp2 condensates formed by Nst1 variants could be observed
307 under these conditions (Fig. 5A).

308 Using high-resolution confocal microscopy, we clearly observed the formation of multiphasic condensates
309 composed of Nst1 and Dcp2 (Fig. 5B). Most wild-type Nst1 condensates were co-localized with mKate2-
310 tagged Dcp2, suggesting that Nst1 condensates promote the formation of Dcp2 condensates (Fig. 5C).
311 Interestingly, the fluorescence signals from Nst1 and Dcp2 condensates did not completely overlap; instead,
312 the two signals appeared as if distinct condensates were docked together (Fig. 5B).

313 Both Nst1ΔPA and Nst1ΔD1 condensates also exhibited co-localization with Dcp2-mKate2 condensates
314 (Fig. 5B-C). Although Nst1ΔPA condensates were able to induce Dcp2 condensation, their size was
315 relatively smaller compared to other Nst1 variant condensates, consistent with the unique role of PA in
316 coalescence of Nst1's microphase condensates (Fig. 5B). In contrast, Nst1ΔPAM condensates rarely
317 promoted the formation of Dcp2 condensates, highlighting the critical role of the PAM domain in facilitating
318 Dcp2 condensation upon Nst1 overexpression (Fig. 5B). Condensates formed by overexpression of GFP-
319 tagged Nst1 and its mutants demonstrated no change in the integrated density of puncta before and after

320 CHX treatment (S7. A). This indicates that a decrease in cytoplasmic concentration of ribosomal free RNA
321 induced by CHX treatment does not affect Nst1 condensation.

322 To confirm the role of PAM on Dcp2 condensation, we employed an additional experimental approach to
323 quantitatively measure Dcp2 condensation induced by overexpression of Nst1ΔPA and Nst1ΔPAM in each
324 cell. If the PAM domain induces Dcp2 condensation directly, rather than via RNA, then the number of Dcp2
325 condensates should not be reduced in Nst1ΔPA cells even after cycloheximide treatment, because
326 Nst1ΔPA condensates, which contain the PAM domain, fail to coalesce and instead increase in number. In
327 contrast, Nst1ΔPAM should lead to a significant reduction in the number of Dcp2 condensates (Fig. 5D).
328 For the quantitative analysis of Dcp2 condensates induced by condensation of wild-type Nst1 and its
329 domain deletion mutants, instead of relying on the weak signals from mKate2-tagged Dcp2, we employed
330 a GFP-tagged Dcp2 strain that allowed more robust quantification to further validate the function of the
331 PAM domain (Fig. 5D). Cells overexpressing either non-tagged full-length Nst1 or the deletion mutants
332 (Nst1ΔPA, Nst1ΔPAM) for 4 hours were treated with cycloheximide for 10 minutes prior to imaging.
333 Subsequently, the puncta formed by chromosomally EGFP-tagged Dcp2 in these overexpression
334 conditions were segmented and quantified (Fig. 5D-E). Notably, cells overexpressing Nst1ΔPA exhibited a
335 substantially higher number of Dcp2 puncta per cell compared to cells overexpressing wild-type Nst1 (Fig.
336 5E), suggesting that the increased number of Nst1ΔPA condensates containing the PAM domain may
337 promote the formation of a greater number of Dcp2 condensates than wild-type Nst1. In contrast, the
338 number of Dcp2 puncta per cell was reduced in Nst1ΔPAM-overexpressing cells relative to the wild-type
339 (Fig. 5E), indicating that the PAM domain provides a physical platform necessary for efficient Dcp2
340 condensation.

341

342 ***The Polyanion (PA) domain of human TDP-43 promotes coalescence of condensates, similar to***
343 ***Nst1.***

344

345 We expanded the functional analysis of PA and PAM subdomains to the scaffold protein Edc3 focusing
346 on their roles in biomolecular condensation. Since Edc3 also has a distinctive negative charged amino acid
347 cluster in PE domain, we divided the PE domain of Edc3 into two parts: the PA region, characterized by a
348 cluster of negatively charged amino acids, and the PAM region, where positively and negatively charged
349 amino acids are more evenly distributed (Fig. S2, S8). We constructed plasmids for the overexpression of
350 GFP-tagged Edc3ΔPAM and Edc3ΔPA mutants, and overexpressed them together with GFP-tagged Edc3,
351 Edc3ΔPE, and Edc3ΔAPD in the *Δedc3* strain to examine their condensate phenotypes. Remarkably, as
352 observed with Nst1, after 4 hours of overexpression, Edc3 formed mature condensates, whereas Edc3ΔPA,
353 similar to Edc3ΔPE, exhibited microphase separation in all cells (Fig. S8). Even after 24 hours of induction,
354 Edc3ΔPA failed to form mature condensates in almost all cells, and only microphase-separated
355 condensates were observed, demonstrating the role of PA in coalescence of Edc3 condensates.
356 Edc3ΔAPD, consistent with the result of Nst1, did not form condensates (Fig. S8).

357 We then investigated whether the phenotype of PA deletion mutants observed in the budding yeast
358 proteins Nst1 and Edc3 is also present in proteins with self-condensation potential that are implicated in
359 neurodegenerative diseases. Since TDP-43 are known to undergo self-condensation upon overexpression
360 in budding yeast (Fushimi et al., 2011; Johnson et al., 2008; Outeiro and Lindquist, 2003; Sun et al., 2011),
361 we first confirmed TDP-43 aggregation upon overexpression in budding yeast as been previously reported.
362 Under the same overexpression conditions used for Nst1 and Edc3, TDP-43 also underwent self-
363 condensation in budding yeast (Fig. 6B). Two PA domains (PA1, PA2) in the TDP-43 sequence were
364 designated with using the sliding window approach (Fig. 6A, S3). The low complexity region in the C-
365 terminal domain (CTD) has been known to be critical for TDP-43 amyloid aggregation (Chien et al., 2021;
366 Li et al., 2021; Shenoy et al., 2023). The CTD has a relatively low charged amino acid cluster score, but
367 within the CTD, residues 255-276, which have a relatively high density of charged amino acid, were
368 designated as the PAM domain. To identify intrinsic sequence determinants that consists of charged amino
369 acid cluster of TDP-43 aggregation, we generated and overexpressed those deletion mutants of TDP-43 in
370 the budding yeast system and monitored them over time. Strikingly, the PA1 and PA2 deletion mutants
371 failed to form mature condensates at 4 hours of overexpression compared to the full-length TDP-43,
372 suggesting their roles in coalescence of condensates as observed role of PA in Nst1 and Edc3 (Fig. 6B).

373 The previously characterized CTD deletion mutant having NLS sequence also formed condensates when
374 overexpressed, similar to the reported study (Johnson *et al.*, 2008; Wang et al., 2018a). The morphology
375 of these condensates differed from that of the full-length TDP-43: while the full-length TDP-43 formed both
376 large and small, irregularly shaped condensates, the CTD deletion mutant produced very large, round
377 condensates in much lower numbers per cell (Fig. 6B). Interestingly, the condensate morphology of the
378 TDP-43ΔCTD mutant was recapitulated in the TDP-43ΔPAM mutant in the nucleus, suggesting that the
379 phenotype in the nucleus might be attributable to the loss of the PAM domain within the CTD rather than
380 the entire NTD existence or CTD deletion. This implies that the charged amino acid cluster within the CTD
381 may play a key role in determining the physical properties and dynamics of TDP-43 condensates in the
382 nucleus. Since these TDP-43 mutants generated retain the nuclear localization signal (NLS), all
383 overexpressed mutants predominantly localize to and form condensates in the nucleus. To observe the
384 condensates of mutants in the cytoplasm, we additionally generated NLS-mutated TDP-43 variants. These
385 variants exhibited phenotypes similar to those observed in the nucleus, except for the CTD-deleted TDP-
386 43 variant: the PA1 and PA2 deletion mutants failed to form mature condensates (Fig 6B). Notably, while
387 overexpressed TDP-43ΔCTD forms condensates in the nucleus, it remains diffusely distributed in the
388 cytoplasm (Fig. 6B). The phenotypic pattern observed for each mutant after 4 hours of induction remained
389 unchanged in cells induced for 8, 10, or 12 hours (S9).

390 To determine whether the condensate phenotypes of PA1, PA2, PAM, and CTD deletion mutants of TDP-
391 43 observed in budding yeast are also present in mammalian cells, we overexpressed GFP-fused TDP-43
392 and TDP-43 mutants in U2OS cells. Consistent with our findings in budding yeast, the PA1 and PA2 deletion
393 mutants formed less mature condensates in the nucleus, compared to the wildtype TDP-43 (Fig. 6C). In
394 particular, the PA2 deletion mutant rarely formed condensates in the nucleus among all cells expressing
395 the protein, as indicated by the presence of GFP signal (Fig. 6C).

396 To observe the condensation of TDP-43 derivatives in the cytoplasm, we introduced an additional NLS
397 mutation (K82A, R83A, K84A) into each GFP-fused TDP-43 domain deletion mutant and examined their
398 expression in U2OS cells (Lu et al., 2022). The cytoplasmic expression of these TDP-43 derivatives
399 displayed a similar pattern of puncta formation to their nuclear counterparts. In the case of the ΔPA1ΔPA2

400 double deletion, condensate formation was further inhibited. These data confirm that PA domains are a key
401 contributor to condensation of TDP-43. Notably, the PAM domain deletion mutant exhibited a markedly
402 larger size and higher fluorescence intensity of puncta compared to other mutants both in nucleus and
403 cytoplasm (Fig. 6C).

404 We next investigated whether the TDP-43 coalescence tendency observed for the PA1 and PA2 mutants
405 was attributable to the negative charges of the clustered amino acids. To this end, we generated *PA1-1*,
406 *PA1-2*, *PA2-1*, and *PA2-2* mutants in which the glutamate (E) and aspartate (D) residues in the partial N-
407 and C-terminal regions of PA1 and PA2 were individually substituted with glutamine (Q) and asparagine
408 (N), respectively, as well as *PA1* and *PA2* mutants in which all glutamate and aspartate residues were
409 replaced with glutamine and asparagine (Fig. 6D).

410 Upon galactose induction in budding yeast cells, the PA1 and PA2 mutants with all negatively charged
411 amino acids replaced by uncharged glutamine and asparagine exhibited a completely different profile in
412 puncta formation compared to the wildtype TDP-43 protein (Fig. 6E). Unlike the ΔPA1 mutant, the *PA1*
413 mutant exhibited a distinct phenotype: while the overexpressed ΔPA1 mutant displayed microphase
414 separation, the overexpressed *PA1* showed a pronounced inhibition of condensate seeding (Fig. 6E). The
415 *PA1-1* mutant, with partial N-terminal substitution, exhibited morphology identical to wildtype condensates,
416 whereas *PA1-2* which includes E17Q and E21Q, resembled the *PA1* mutant, suggesting consistency with
417 previous findings that E17 and E21 in the TDP-43 N-terminal domain are critical residues required for
418 oligomerization (Afroz et al., 2017).

419 Notably, the results for the PA2 domain are remarkable. The *PA2* exhibited condensate morphology
420 identical to that of ΔPA2 and displayed a pronounced tendency toward microphase separation, unlike the
421 wildtype TDP-43 which forms mature condensates, (Fig. 6D). Unlike the *PA1-1* and *PA1-2* mutants, both
422 the *PA2-1,* the *PA2-2* mutant which have partial substitutions of negatively charged amino acids in either
423 the N-terminal or C-terminal regions failed to fully recapitulate the puncta generation patterns of ΔPA2 (Fig.
424 6D). These results indicate that it is not specific negatively charged residues within PA2 that are critical, but
425 rather that the overall clusters of negatively charged amino acids in PA2 contribute to TDP-43 coalescence.

426 We introduced the same amino acid substitution mutants into U2OS cells. Microscopic images were
427 captured for each mutant, and the portion of puncta-forming cells was quantified across the GFP-expressing
428 cell population (Fig. 6F–G). While the TDP-43 mutant lacking the NLS but harboring no additional mutations
429 formed small yet distinct cytoplasmic puncta, puncta formation was markedly inhibited in all substitution
430 mutants with the exception of *PA1-1* (Fig. 6F–G). These results suggest the possibility that negative
431 charges within the negatively charged amino acid clusters serve as critical regulators of TDP-43 phase
432 behavior.

433

434 **DISCUSSION**

435 Protein condensation in cell is not a binary switch between soluble and demixed states, but rather a multi-
436 step process involving distinct kinetic phases: evolving from dynamic droplets into more stable, gel-like, or
437 solid states within the cellular environment (Shen et al., 2023; Wang et al., 2021). The maturation of
438 condensates is essentially driven by thermodynamic coarsening mechanisms—such as coalescence and
439 Ostwald ripening—and is not merely a physical hardening but a biochemical cascade that facilitates
440 pathological transitions(Banani *et al.*, 2017). By concentrating condensation-prone proteins through these
441 coarsening dynamics, condensates lower the energetic barrier for amyloidogenesis, creating a fertile
442 environment where initial oligomeric species can form and act as seeds to template the conversion of native
443 proteins into amyloid fibrils (Berry et al., 2015; Dickson and Golding, 2022; Sim and Creamer, 2002; Visser
444 *et al.*, 2024). LCRs are closely associated with phenotypic variation (Fondon and Garner, 2004) and
445 function as multivalent interaction hubs, playing a critical role in protein condensation and amyloidogenesis
446 (Banjade and Rosen, 2014; Linsenmeier *et al.*, 2023). Collectively, these findings strongly suggest that
447 LCRs are physiologically and pathologically important components in complex biological systems.

448 Charged amino acid clusters within LCRs represent one of the most frequently observed sequence motifs
449 within proteins consisting of RNP granules (Niedner-Boblenz et al., 2024; Regy et al., 2020; Saitoh et al.,
450 2004). Within intrinsically disordered regions (IDRs), there have been numerous clues that certain charged
451 amino acids may contribute to the regulation of condensation, either by promoting or inhibiting condensation
452 (Saar et al., 2021). Both negatively and positively charged amino acids are thought to modulate

453 intermolecular affinity via electrostatic interactions, where the pattern of charged residues along the
454 sequence plays a pivotal role. As mentioned previously, when charged residues are uniformly distributed,
455 the driving force for phase separation is attenuated; in contrast, when charged residues are clustered or
456 segregated from other residues, the propensity for phase separation is enhanced (Borcherds et al., 2021;
457 Saitoh *et al.*, 2004; Wang *et al.*, 2018b). This study presents the first report on the differential roles of low-
458 complexity regions (LCRs) composed of charged amino acids as sequence elements specifically
459 regulating phase of the condensates.

460 With budding yeast proteins, Nst1 and Edc3, we demonstrate that the specific deletion and mutation of
461 the negatively charged amino acid clusters termed polyanion (PA) domain in Nst1 and Edc3 lead to a
462 distinct defect in coalescence, without abolishing the initial nucleation capability. This implies that the
463 grammar governing assembly is distinct from the grammar governing fluidity and fusion. While multivalent
464 interactions via PAM domains or RNA binding may drive nucleation (Van Treeck and Parker, 2018), the
465 negative charged amino acid clusters in Nst1 and Edc3 appear to be a prerequisite for this maturation
466 trajectory and act as 'cohesion-tuners' that enable the fusion between microphase condensates. FRAP
467 analysis of Nst1 provides a mechanistic explanation for these phenotypes. The significantly rapid FRAP
468 recovery of the Nst1ΔPA mutant suggests that the failure to coalesce is due to a loss of cohesive force
469 (surface tension) rather than rigidification. Specifically, the observed "hyper-dynamic but non-coalescing"
470 state suggests that this is not merely due to a loss of molecular stickiness, but rather because the interfacial
471 tension between the droplets and the surrounding cytoplasm is reduced to a point where there is no
472 energetic favorability to drive Ostwald ripening or coalescence (Brangwynne et al., 2009).

473 Another important aspect of this study is that this "coalescence grammar" is conserved in the human
474 disease protein TDP-43. While both the ΔPA1 and ΔPA2 mutants exhibited coalescence-inhibited
475 condensates, their corresponding negative charge substitution mutants diverged significantly. The PA1 led
476 to a complete loss of condensates, a phenotype faithfully reproduced by the PA1-2 mutant, which
477 completely suppressed condensate nucleation. This result corroborates previous findings that residues E17
478 and E21 are critical for TDP-43 oligomerization(Afroz *et al.*, 2017; Wang *et al.*, 2018a). In contrast, the *PA2*
479 displayed a phenotype of impaired condensate coarsening, which was identical to that of the ΔPA2.
480 Furthermore, the observation that neither the *PA2-1* nor the *PA2-2* partial substitution mutants could fully

481 recapitulate the complete *PA2* phenotype suggests that the entire negative charge cluster within the PA2
482 region collectively functions in regulating condensate coarsening.

483 Taken together, these findings imply that the functional role of a negatively charged amino acid residue in
484 the condensation process is highly context-dependent. This underscores the necessity for a more nuanced
485 investigation into the diverse functions and positional effects of negative charge clusters in the regulation
486 of protein condensation. Although we did not directly measure the biophysical properties of TDP-43 mutants,
487 the phenotypic similarity strongly suggests a conserved mechanism: these negatively charged residues
488 likely provide the necessary cohesive potential to form and mature TDP-43 condensates in cells (Afroz *et*
489 *al.*, 2017; Conicella et al., 2016). Thus, the negative charge clusters are essential for tuning the phase
490 separation threshold and condensate properties, presumably acting as a molecular rheostat that controls
491 whether TDP-43 achieves sufficient condensate maturation to propagate pathological states or remains in
492 a more soluble, dispersed form.

493 A remarkable region within TDP-43 is the PAM domain, which appears to play a critical role in regulating
494 condensate dynamics. In U2OS cells, we observed an unexpected phenotype: the deletion of the PAM
495 domain—regardless of NLS mutation status—resulted in significantly enlarged condensates. This
496 phenotype, which was not evident in budding yeast, implies that the PAM domain functions to inhibit
497 condensate coarsening, standing in direct contrast to the PA domain.

498 Notably, the PAM domain encompasses Lysine 263 (K263), a residue critical for RNA interaction. The
499 K263E mutation has been identified as a pathogenic variant that drastically reduces RNA binding affinity
500 by disrupting electrostatic interactions with the RNA backbone, leading to severe neurotoxicity (Austin et
501 al., 2014; Imaizumi et al., 2022). Paradoxically, this loss of binding capacity is accompanied by increased
502 thermal stability, rendering the protein structurally rigid and prone to aggregation (Austin *et al.*, 2014; Chen
503 et al., 2019). These findings suggest that the enlarged condensates observed in PAM-deleted TDP-43 are
504 presumably driven by a similar mechanism: a reduction in RNA binding affinity. Therefore, a detailed
505 investigation into the role of charged amino acids within the PAM domain is essential to fully understand
506 the molecular mechanisms underlying these observations. Given its pivotal role in preventing aberrant

507 condensate growth, the PAM domain offers a critical foundation for elucidating TDP-43 phase separation
508 dynamics and represents a promising target for future therapeutic investigations.

509 Finally, our study underscores the indispensability of investigating condensate physics directly within the
510 cellular environment. The distinction between a “matured condensates” and a “hyper-dynamic, non-
511 coalescing seed”, as observed in Nst1, is impossible to discern using static imaging or pure in vitro systems
512 lacking cellular crowding and energy (Snead and Gladfelter, 2019). By employing live-cell biophysical tools,
513 we established a more physiologically relevant framework for understanding condensate dynamics. This
514 approach suggests that future therapeutic strategies should focus on modulating these specific sequence
515 motifs to restore the material properties of condensates within the living cell.

516

517 **STAR★METHODS**

518 **KEY RESOURCES TABLE**

REAGENT OR RESOURCE	SOURCE	IDENTIFIER
Antibodies		
goat anti-GFP	ROCKLAND, USA	Cat# 600-101-215
mouse anti-Tub1	Sigma, USA	Cat# T5168
anti-goat (secondary antibody)	Jackson ImmunoResearch Laboratories, Inc, USA	Cat# 705-035-003
anti-Mouse (secondary antibody)	Santa Cruz Biotechnology, USA	Cat# sc-2005
Bacterial and virus strains		
Escherichia coli DH5α cells One Shot™ TOP10 Chemically Competent *E. coli*	Invitrogen, USA	Cat# C404003
Biological samples		
Salmon sperm DNA (Deoxyribonucleic acid sodium salt from salmon testes)	Sigma, USA	Cat# D1626

Chemicals, peptides, and recombinant proteins		
1,6-Hexanediol	DAEJUNG CHEMICAL & METALS CO., LTD, South Korea	Cat# 629-11-8
4% paraformaldehyde	T&I, South Korea	Cat# BPP-9004
	Cytiva,USA,	Cat# SH30088.03
WestGlowTM PICO PLUS Chemiluminescent Substrate	BIOMAX, South Korea	Cat# BWP0200
20X TBS-T (20X Tris-Buffered Saline/1% Tween-20)	T&I, South Korea	Cat# BTT-9120
Antibiotic-antimycotic solution (Anti-Anti)	Gibco, USA,	Cat# 15240-062
Experimental models: Cell lines		
U2OS cells Human osteosarcoma cell line	ATCC	HTB-96
Experimental models: Organisms/strains		
Saccharomyces cerevisiae W303a *leu2-3,112 trp1-1 can1-100 ura3-1 ade2-1 his3-11,15*	S. Elledge	YSK3549
Saccharomyces cerevisiae W303a except as *Δedc3::KANMX*	this study	YSK3707
Saccharomyces cerevisiae W303a except as *Δnst1::KANMX*	this study	YSK3490
Saccharomyces cerevisiae W303a except as *NST1-EGFP::KANMX*	K.Song	YSK3498
Saccharomyces cerevisiae W303a except as *DCP2-EGFP::HIS3MX6*	K.Song	YSK3527
Saccharomyces cerevisiae W303a except as *EDC3-EGFP::HIS3MX6*	K.Song	YSK3528
Saccharomyces cerevisiae W303a except as *Δnst1::KANMX pNST1-GFP-NST1::URA3*	this study	YSK3700
Saccharomyces cerevisiae W303a except as *Δnst1::KANMX pNST1-GFP-NST1ΔPA::URA3*	this study	YSK3701
Saccharomyces cerevisiae W303a except as *Δnst1::KANMX pNST1-GFP-NST1ΔPAM::URA3*	this study	YSK3702
Saccharomyces cerevisiae W303a except as *Δnst1::KANMX pNST1-GFP-NST1ΔAPD::URA3*	this study	YSK3714
Saccharomyces cerevisiae W303a except as *Δnst1::KANMX PAB1-EGFP::HIS3MX6*	this study	YSK3704
Saccharomyces cerevisiae W303a expect as *Δnst1::KANMX EDC3-EGFP::HIS3MX6*	this study	YSK3694
Saccharomyces cerevisiae W303a expect as *Δnst1::KANMX DHH1-EGFP::HIS3MX6*	this study	YSK3695

Saccharomyces cerevisiae W303a expect as *Δnst1::KANMX DCP2-EGFP::HIS3MX6*	this study	YSK3709
Saccharomyces cerevisiae BY4741expect as *Δnst1::KANMX DCP2-mKate2-sphis5*	this study	YSK3663
Oligonucleotides		
pMW20(U)-pGAL-GFP-NST1Δ2-122 deletion top 5' ATTACACATGGCATGGATGAACGAGCTCAGTTTAATGTCATAAGGAATTACCAGG ACGAT 3'	this study	KS2262
pMW20(U)-pGAL-GFP-NST1Δ2-122 deletion bottom 5' ATCGTCCTGGTAATTCCTTATGACATTAAACTGAGCTCGTTCATCCATGCCATGTG TAAT 3'	this study	KS2263
pMW20(U)-pGAL-GFP-NST1Δ123-293 deletion top 5' ACTATTCTACGAATCGAAAAGGAGGAAGTACAAAAAATGATGATGTATCCGAATAT TAGA 3'	this study	KS2384
pMW20(U)-pGAL-GFP-NST1Δ123-293 deletion bottom 5' TCTAATATTCGGATACATCATCATTTTTTGTACTTCCTCCTTTTCGATTCGTAGAAT AGT 3'	this study	KS2385
pMW20(U)-pGAL-GFP-NST1Δ294-459 deletion top 5' TCACATCCCAAAATAGCAGAGGAGTATGTAGAAGATGAAGATGAGGAAGACTATG ATGAC 3'	this study	KS2386
pMW20(U)-pGAL-GFP-NST1Δ294-459 deletion bottom 5' GTCATCATAGTCTTCCTCATCTTCATCTTCTACATACTCCTCTGCTATTTTGGGATG TGA 3'	this study	KS2387
pMW20(U)-pGAL-GFP-NST1Δ460-630 deletion top 5' GATACTTCGTTAGATACTGATTCTATATATCTAGAAGAAGAAAAAAGAAAGAAAAG AGAG 3'	this study	KS2280
pMW20(U)-pGAL-GFP-NST1Δ460-630 deletion bottom 5' CTCTCTTTTCTTTCTTTTTTCTTCTTCTAGATATATAGAATCAGTATCTAACGAAGTA TC 3'	this study	KS2281
pMW20(U)-pGAL-GFP-NST1Δ755-844 deletion top 5' AGAGAACAGAAAAGGCTAGAACAAGAAAAGGATCTACTTCTTCCTTCAACTAACAA CCAG 3'	this study	KS2397

pMW20(U)-pGAL-GFP-NST1Δ755-844 deletion bottom 5' CTGGTTGTTAGTTGAAGGAAGAAGTAGATCCTTTTCTTGTTCTAGCCTTTTCTGTT CTCT 3'	this study	KS2398
pMW20(U)-pGAL-GFP-NST1Δ845-1015 deletion top 5' CCAGTTTCACCCACAGGCTTTAACGTTCATGATCAAAAAAGCTCATTTTCGGGACC GTCG 3'	this study	KS2388
pMW20(U)-pGAL-GFP-NST1Δ845-1015 deletion bottom 5' CGACGGTCCCGAAAATGAGCTTTTTTGATCATGAACGTTAAAGCCTGTGGGTGAA ACTGG 3'	this study	KS2389
pMW20(U)-pGAL-GFP-NST1Δ460-596 deletion top 5' GATACTTCGTTAGATACTGATTCTATATATCGGAAATTGATTCAGATAGCCATTACA AAG 3'	this study	KS2437
pMW20(U)-pGAL-GFP-NST1Δ460-596 deletion bottom 5'GATACTTCGTTAGATACTGATTCTATATATCGGAAATTGATTCAGATAGCCATTA CAAAG 3'	this study	KS2438
pMW20(U)-pGAL-GFP-EDC3Δ65-205 deletion top 5' AGGTTCTAACTGTTGCCTCTCCCAAATACCTACCAATAAC 3'	this study	KS2360
pMW20(U)-pGAL-GFP-EDC3Δ65-205 deletion bottom 5' GTTATTGGTAGGTATTTGGGAGAGGCAACAGTTAGAACCT 3'	this study	KS2361
pMW20(U)-pGAL-GFP-EDC3Δ65-180 deletion top 5' AAGGACTTAAAGGTTCTAACTGTTGCCTCTCCGCAACAAGATGCTCAAGATGATCT GGTT 3'	this study	KS2446
pMW20(U)-pGAL-GFP-EDC3Δ65-180 deletion bottom 5' AACCAGATCATCTTGAGCATCTTGTTGCGGAGAGGCAACAGTTAGAACCTTTAAG TCCTT 3'	this study	KS2447
pMW20(U)-pGAL-GFP-EDC3Δ181-205 deletion top 5' AGAAATGAGCAAAGCACACACCAATCTCAGCCCAAATACCTACCAATAACTCAGT CTTTG 3'	this study	KS2444
pMW20(U)-pGAL-GFP-EDC3Δ181-205 deletion bottom 5' CAAAGACTGAGTTATTGGTAGGTATTTGGGCTGAGATTGGTGTGTGCTTTGCTCAT TTCT 3'	this study	KS2445
pMW20(U)-pGAL-GFP-EDC3Δ330-380 deletion top 5' AACTAGGTGGCCGTGCACGTCTACAGGATTCCATGGTCAA 3'	this study	KS2362

pMW20(U)-pGAL-GFP-EDC3Δ330-380 deletion bottom 5' TTGACCATGGAATCCTGTAGACGTGCACGGCCACCTAGTT 3'	this study	KS2363
pMW20(U)-pGAL-GFP-TARDBP infusion cloning top 5' GCATGGATGAACGAGCTTCTGAATATATTCGGGTAAC 3'	this study	KS2401
pMW20(U)-pGAL-GFP-TARDBP infusion cloning bottom 5' GTCGACTCTAGAGGATCCCTACATTCCCCAGCCAGAAG 3'	this study	KS2402
pMW20(U)-pGAL-GFP-TARDBPΔ2-29 deletion top 5' GGGATTACACATGGCATGGATGAACGAGCTACGGTTACAGCCCAGTTTCCAGGG GCGTGT 3'	this study	KS2429
pMW20(U)-pGAL-GFP-TARDBPΔ2-29 deletion bottom 5' ACACGCCCCTGGAAACTGGGCTGTAACCGTAGCTCGTTCATCCATGCCATGTGTA ATCCC 3'	this study	KS2430
pMW20(U)-pGAL-GFP-TARDBPΔ197-220 deletion top 5' CCTTTGAGAAGCAGAAAAGTGTTTGTGGGGTTCATCCCCAAGCCATTCAGGGCCT TTGCC 3'	this study	KS2448
pMW20(U)-pGAL-GFP-TARDBPΔ197-220 deletion bottom 5' GGCAAAGGCCCTGAATGGCTTGGGGATGAACCCCACAAACACTTTTCTGCTTCTC AAAGG 3'	this study	KS2449
pMW20(U)-pGAL-GFP-TARDBPΔ255-276 deletion top 5' GGAGAGGACTTGATCATTAAAGGAATCAGCGGTGGTAATCCAGGTGGCTTTGGG AATCAG 3'	this study	KS2431
pMW20(U)-pGAL-GFP-TARDBPΔ255-276 deletion bottom 5' CTGATTCCCAAAGCCACCTGGATTACCACCGCTGATTCCTTTAATGATCAAGTCCT CTCC 3'	this study	KS2432
pMW20(U)-pGAL-GFP-TARDBPΔ255-414 deletion top 5' GGACTTGATCATTAAAGGAATCAGCTAGGGATCCTCTAGAGTCGACCTGC 3'	this study	KS2439
pMW20(U)-pGAL-GFP-TARDBPΔ255-414 deletion bottom 5' GCAGGTCGACTCTAGAGGATCCCTAGCTGATTCCTTTAATGATCAAGTCC 3'	this study	KS2440
TARDBPΔNLS (K82A, R83A, K84A) top 5' GTGTATGTTGTCAACTATCCAAAAGATAACGCAGCAGCAATGGATGAGACAGATG CTTCATCAGCAGTG 3'	this study	KS2472

TARDBPΔNLS (K82A, R83A, K84A) bottom 5' CACTGCTGATGAAGCATCTGTCTCATCCATTGCTGCTGCGTTATCTTTTGGATAGT TGACAACATACAC 3'	this study	KS2473
pRS306-pNST1-GFP-NST1 infusion cloning top 5' CGTCCCGGGATGAGTAAAGGAGAAGAACTTTTC 3'	this study	KS2238
pRS306-pNST1-GFP-NST1 infusion cloning bottom 5' CGTCTCGAGCAAATTTAAGACGTTTGCGTAG 3'	this study	KS2239
pRS306-pNST1-GFP-NST1Δ460-630 top 5' GATACTTCGTTAGATACTGATTCTATATATCTAGAAGAAGAAAAAAGAAAGAAAAG AGAG 3'	this study	Ks2280
pRS306-pNST1-GFP-NST1Δ460-630 bottom 5' CTCTCTTTTCTTTCTTTTTTCTTCTTCTAGATATATAGAATCAGTATCTAACGAAGTA TC 3'	this study	Ks2281
pRS306-pNST1-GFP-NST1Δ631-752 top 5' GATAATAACAGACTAAAACTTCTACAAGAACTACAGAAAGAAAAAGAAGAAGAAGA GAGA 3'	this study	KS2176
pRS306-pNST1-GFP-NST1Δ631-752 bottom 5' TCTCTCTTCTTCTTCTTTTTCTTTCTGTAGTTCTTGTAGAAGTTTTAGTCTGTTATTA TC 3'	this study	KS2177
pRS306-pNST1-GFP-NST1Δ1016-1240 top 5' GGCATGGATGAACGAGCTCAGGATCAAAAAAGCTCATTTTCG 3'	this study	KS2194
pRS306-pNST1-GFP-NST1Δ1016-1240 bottom 5' CGAAAATGAGCTTTTTTGATCCTGAGCTCGTTCATCCATGCC 3'	this study	KS2195
pcDNA3.1myc-HisA-GFP-TARDBP infusion cloning top 5'AGCTGGCTAGTTAAGCTTGGTACCATGAGTAAAGGAGAAGAACTTTTC 3'	this study	KS2455
pcDNA3.1myc-HisA-GFP-TARDBP infusion cloning bottom 5'GCGGCCGCCACTGTGCTGGATATCCTACATTCCCCAGCCAGAAGACTT 3'	this study	KS2456
TARDBP *PA1-1* (E3Q, E9Q, D10N, E11Q) ΔNLS (K82A, R83A, K84A) top 5' GCATGGATGAACGAGCTTCTCAGTATATTCGGGTAACCCAGAACCAGAACGATGA GCCCATTGAAAT 3'	this study	KS2492
TARDBP *PA1-1* (E3Q, E9Q, D10N, E11Q) ΔNLS (K82A, R83A, K84A) bottom 5' ATTTCAATGGGCTCATCGTTCTGGTTCTGGGTTACCCGAATATACTGAGAAGCTC GTTCATCCATGC 3'	this study	KS2493

TARDBP *PA1-2* (D13N, E14Q, E17Q, E21Q, D22N, D23N) ΔNLS (K82A, R83A, K84A) top 5' GGGTAACCGAAGATGAGAACAACCAGCCCATTCAGATACCATCGCAGAACAACG GGACGGTGCTGCTCTCCAC 3'	this study	KS2494
TARDBP *PA1-2* (D13N, E14Q, E17Q, E21Q, D22N, D23N) ΔNLS (K82A, R83A, K84A) bottom 5' GTGGAGAGCAGCACCGTCCCGTTGTTCTGCGATGGTATCTGAATGGGCTGGTTG TTCTCATCTTCGGTTACCC 3'	this study	KS2495
TARDBP *PA1-1PA1-2* (E3Q, E9Q, D10N, E11Q, D13N, E14Q, E17Q, E21Q, D22N, D23N) ΔNLS (K82A, R83A, K84A) top 5' GCATGGATGAACGAGCTTCTCAGTATATTCGGGTAACCCAGAACCAGAACAACCA GCCCATTCAGAT 3'	this study	KS2500
TARDBP *PA1-1PA1-2* (E3Q, E9Q, D10N, E11Q, D13N, E14Q, E17Q, E21Q, D22N, D23N) ΔNLS (K82A, R83A, K84A) bottom 5' ATCTGAATGGGCTGGTTGTTCTGGTTCTGGGTTACCCGAATATACTGAGAAGCTC GTTCATCCATGC 3'	this study	KS2501
TARDBP *PA2-1* (E200Q, D201N, E204Q, D205N, E206Q, E209Q) ΔNLS (K82A, R83A, K84A) top 5' TGTTTGTGGGGCGCTGTACACAGAACATGACTCAGAACCAGCTGCGGCAGTTCTT CTCTCAGTACGGGGA 3'	this study	KS2484
TARDBP *PA2-1* (E200Q, D201N, E204Q, D205N, E206Q, E209Q) ΔNLS (K82A, R83A, K84A) bottom 5' TCCCCGTACTGAGAGAAGAACTGCCGCAGCTGGTTCTGAGTCATGTTCTGTGTAC AGCGCCCCACAAACA 3'	this study	KS2485
TARDBP *PA2-2* (D216N, D219N) ΔNLS (K82A, R83A, K84A) top 5' AGTTCTTCTCTCAGTACGGGAACGTGATGAACGTCTTCATCCCCAAGCCATT 3'	this study	KS2486
TARDBP *PA2-2* (D216N, D219N) ΔNLS (K82A, R83A, K84A) bottom 5' AATGGCTTGGGGATGAAGACGTTCATCACGTTCCCGTACTGAGAGAAGAACT 3'	this study	KS2487
Recombinant DNA		
pMW20(U)-pGAL-GFP	This study	
pMW20(U)-pGAL-GFP-NST1	This study	
pMW20(U)-pGAL-GFP-NST1Δ2-122	This study	
pMW20(U)-pGAL-GFP-NST1Δ123-293	This study	
pMW20(U)-pGAL-GFP-NST1Δ294-459	This study	
pMW20(U)-pGAL-GFP-NST1Δ460-752	This study	
pMW20(U)-pGAL-GFP-NST1Δ460-630	This study	
pMW20(U)-pGAL-GFP-NST1Δ631-752	This study	

pMW20(U)-pGAL-GFP-NST1Δ753-844	This study	
pMW20(U)-pGAL-GFP-NST1Δ845-1015	This study	
pMW20(U)-pGAL-GFP-NST1Δ1016-1240	This study	
pMW20(U)-pGAL-GFP-NST1Δ460-596	This study	
pMW20(U)-pGAL-GFP-EDC3	This study	
pMW20(U)-pGAL-GFP-EDC3Δ65-205	This study	
pMW20(U)-pGAL-GFP-EDC3Δ65-180	This study	
pMW20(U)-pGAL-GFP-EDC3Δ181-205	This study	
pMW20(U)-pGAL-GFP-EDC3Δ330-380	This study	
pMW20(U)-pGAL-GFP-TARDBP	This study	
pMW20(U)-pGAL-GFP-TARDBPΔ2-29	This study	
pMW20(U)-pGAL-GFP-TARDBPΔ197-220	This study	
pMW20(U)-pGAL-GFP-TARDBPΔ255-276	This study	
pMW20(U)-pGAL-GFP-TARDBPΔ255-414	This study	
pMW20(U)-pGAL-GFP-TARDBPΔNLS (K82A, R83A, K84A)	This study	
pMW20(U)-pGAL-GFP-TARDBPΔ2-29ΔNLS (K82A, R83A, K84A)	This study	
pMW20(U)-pGAL-GFP-TARDBPΔ197-220ΔNLS (K82A, R83A, K84A)	This study	
pMW20(U)-pGAL-GFP-TARDBPΔ255-276ΔNLS (K82A, R83A, K84A)	This study	
pMW20(U)-pGAL-GFP-TARDBPΔ255-414ΔNLS (K82A, R83A, K84A)	This study	
pRS306-pNST1-GFP-NST1	This study	
pRS306-pNST1-GFP-NST1Δ460-630	This study	
pRS306-pNST1-GFP-NST1Δ631-752	This study	
pRS306-pNST1-GFP-NST1Δ1016-1240	This study	
pcDNA3.1myc-HisA-GFP-TARDBP	This study	
pcDNA3.1myc-HisA-GFP-TARDBPΔ2-29	This study	
pcDNA3.1myc-HisA-GFP-TARDBPΔ255-276	This study	
pcDNA3.1myc-HisA-GFP-TARDBPΔ255-414	This study	
pcDNA3.1myc-HisA-GFP-TARDBPΔ197-220	This study	
pcDNA3.1myc-HisA -GFP-TARDBPΔNLS(K82A, R83A, K84A)	This study	
pcDNA3.1myc-HisA -GFP-TARDBPΔ2-29ΔNLS(K82A, R83A, K84A)	This study	
pcDNA3.1myc-HisA -GFP-TARDBPΔ197-220ΔNLS(K82A, R83A, K84A)	This study	
pcDNA3.1myc-HisA -GFP-TARDBPΔ255-276ΔNLS(K82A, R83A, K84A)	This study	

pcDNA3.1myc-HisA -GFP-TARDBPΔ255-414ΔNLS(K82A, R83A, K84A)	This study	
pMW20(U)-pGAL-GFP-TARDBP *PA1-1*(E3Q, E9Q, D10N, E11Q) ΔNLS (K82A, R83A, K84A)	This study	
pMW20(U)-pGAL-GFP-TARDBP *PA1-2*(D13N, E14Q, E17Q, E21Q, D22N, D23N) ΔNLS (K82A, R83A, K84A)	This study	
pMW20(U)-pGAL-GFP-TARDBP *PA1* (E3Q, E9Q, D10N, E11Q, D13N, E14Q, E17Q, E21Q, D22N, D23N) ΔNLS (K82A, R83A, K84A)	This study	
pMW20(U)-pGAL-GFP-TARDBP *PA2-1* (E200Q, D201N, E204Q, D205N, E206Q, E209Q) ΔNLS (K82A, R83A, K84A)	This study	
pMW20(U)-pGAL-GFP-TARDBP *PA2-2* (D216N, D219N) ΔNLS (K82A, R83A, K84A)	This study	
pMW20(U)-pGAL-GFP-TARDBP *PA2* (E200Q, D201N, E204Q, D205N, E206Q, E209Q, D216N, D219N) ΔNLS (K82A, R83A, K84A)	This study	
pcDNA3.1myc-HisA -GFP-TARDBP *PA1-1*(E3Q, E9Q, D10N, E11Q) ΔNLS(K82A, R83A, K84A)	This study	
pcDNA3.1myc-HisA -GFP-TARDBP *PA1-2*(D13N, E14Q, E17Q, E21Q, D22N, D23N) ΔNLS(K82A, R83A, K84A)	This study	
pcDNA3.1myc-HisA -GFP-TARDBP *PA1*(E3Q, E9Q, D10N, E11Q, D13N, E14Q, E17Q, E21Q, D22N, D23N) ΔNLS(K82A, R83A, K84A)	This study	
pcDNA3.1myc-HisA -GFP-TARDBP *PA2-1*(E200Q, D201N, E204Q, D205N, E206Q, E209Q) ΔNLS(K82A, R83A, K84A)	This study	
pcDNA3.1myc-HisA -GFP-TARDBP *PA2-2*(D216N, D219N) ΔNLS(K82A, R83A, K84A)	This study	
pcDNA3.1myc-HisA -GFP-TARDBP *PA2*(E200Q, D201N, E204Q, D205N, E206Q, E209Q, D216N, D219N) ΔNLS(K82A, R83A, K84A)	This study	
Software and algorithms		
AIUPRed – Prediction of Intrinsically Unstructured Proteins	Eötvös Loránd University (ELTE), MTA-ELTE Momentum Bioinformatics Research Group, Hungary	AIUPred
Disopred3	University College London (UCL), Bioinformatics Group	PSIPRED Workbench

PrDOS – Protein Disorder Prediction System	Osaka University, Graduate School of Information Science and Technology	PrDOS - Protein disorder prediction server
PASTA 2.0 – prediction of amyloid structural aggregation	University of Padova, Department of Biomedical Sciences, INFN, Italy	Aggregation Prediction with PASTA
Aggrescan – prediction of “hot spot” of aggregation on polypeptides	Autònoma University of Barcelona, Institute of Biotechnology and Biomedicine, Department of Biochemistry and Molecular Biology, Spain	Aggrescan: Prediction of "hot spots" of aggregation in polypeptides
FELLS – Fast Estimator of Latent Local Structure	BioComputing Up, University of Padua, Italy	FELLS > Submit
GraphPad Prism 5	GraphPad	https://www.graphpad.com/
GraphPad Prism 10	GraphPad	https://www.graphpad.com/
ImageJ	Schindelin et al. Fiji: an open-source platform for biological-image analysis. *Nat. Methods.* 2012; 9:676-682	https://imagej.nih.gov/ij/
Custom Python scripts	This paper	Available upon request
Other		
1.8 ml bead-beating tube	SIMPORT, Canada	Cat# T335-6SPR
Acid-washed 0.5 mm bead	Biospec, USA	Cat# 11079105
Polyvinylidene difluoride (PVDF) membrane	Merk Millipore, USA	Cat# IPVH00010

METHOD DETAILS

521 **Yeast cell culture and transformation**

522 *Saccharomyces cerevisiae* yeast cells were grown in YPAD medium until reaching the exponential growth
523 phase (OD_{600} 0.5). Cells were harvested by centrifugation at 4,000 rpm for 5 min at room temperature (RT).
524 The cell pellet was gently resuspended in 1 mL of 0.1 M LiOAc (Sigma-Aldrich, USA, L6883-250G) and
525 incubated at RT for 5 min, followed by another centrifugation under the same condition. For transformation,
526 cells were gently resuspended in 360 μL of yeast transformation mixture consisting of 50% polyethylene
527 glycol (Sigma-Aldrich, USA, P4338-500G), 1 M LiOAc, 2 mg/mL salmon sperm DNA (Sigma, USA, D1626),
528 and ddH_2O. 100 ng plasmid DNA was added to the cell suspension, and the mixture was incubated at RT
529 for 30 min. Heat shock was performed by incubating the cells at 42°C for 30 min, followed by cooling at RT
530 for 3 min. Cells were harvested again by centrifugation at 4,000 rpm for 5 min at RT, and plated onto SC-
531 Ura plates. Plates were incubated at 25°C until colonies appeared typically 2–3 days.

532 **Protein overexpression in yeast**

533 The cells transformed with plasmids containing NST1, EDC3, *TARDBP* and their deletion mutants were
534 cultured in a SC-U + 2% glucose medium up to the exponential growth phase (OD_{600} 0.5) and harvested.
535 The cells were washed with a SC-U + 2% raffinose + 0.1% glucose medium three times, diluted to half its
536 concentration, and cultured for an additional 3 hours in SC-U + 2% raffinose + 0.1% glucose. Thereafter,
537 galactose was added to a final 2% concentration and incubated for designated hours.

538 **1,6-Hexanediol treatment of yeast**

539 Yeast cells induced for protein overexpression in 2% galactose for 4 hours were harvested by centrifugation
540 at 4000 rpm for 5 minutes, and the resulting pellet was collected. The cell pellet was then resuspended and
541 incubated in SC-U medium supplemented with 2% galactose, 2% raffinose, 0.1% glucose, and 10% 1,6-
542 hexanediol (Daejung Chemical & Metals Co., LTD, South Korea, 629-11-8) for 1 hour.

543 **Chromosomal integration of genes in yeast**

544 Various NST1 deletion mutants were acquired by PCR-mediated deletion cloning with the full length
545 pRS306-pNST1-NST1 and verified by sequencing. Plasmids pRS306-pNST1-NST1 and its deletion

546 mutants were treated with EcoRV to make a single cut at the URA3 and were transformed into *Δnst1* cells
547 (YSK3490) by 42 ˚C heat shock. Integration into the chromosome occurred at low frequency
548 via homologous recombination at the URA3. The transformed cells were plated on the SC plate without
549 uracil and colony PCR was performed to confirm whether the fragment was successfully transformed.

550 **Infusion cloning of genes**

551 The PCR-amplified coding sequences were generated using primers containing 15-bp extensions
552 homologous to the vector ends. The destination vector pcDNA3.1-myc-His was linearized by restriction
553 enzyme digestion at 37°C for 3 h. The digested vector and PCR fragments were then subjected to infusion
554 cloning reaction (EZ-HT cloning kit, Enzynomics, Korea, EZ016TM), which utilizes single-strand annealing
555 activity to join DNA fragments with complementary ends, circumventing the need for conventional ligation.
556 The reaction products were transformed into chemically competent *E. coli* DH5α cells, and transformants
557 were selected on LB agar plates supplemented with ampicillin (100 μg/ml). The integrity of the resulting
558 constructs was verified by DNA sequencing.

559 **TDP-43 PA1 and PA2 Domain Mutagenesis**

560 PCR-based site-directed mutagenesis was performed using the plasmid pMW20(U)-pGAL-GFP-
561 TARDBPΔNLS (K82A, R83A, K84A) and pcDNA3.1-myc-hisA-GFP-TARDBPΔNLS (K82A, R83A, K84A)
562 as a template to introduce targeted amino acid substitutions within the TDP-43 PA1 and PA2 domain. The
563 *PA1-1* mutant was generated with primers KS2492 and KS2493, and the *PA1-2* mutant with KS2494 and
564 KS2495. The *PA2-1* mutant was generated with primers KS2484 and KS2485, and the *PA2-2* mutant with
565 primers KS2486 and KS2487. The *PA1-1PA1-2* and *PA2-1PA2-2* mutants, which harbor both the *PA1-1*
566 and *PA1-2* mutations or *PA2-1* and *PA2-2* mutations, were constructed using the *PA1-2* or *PA2-1* plasmid
567 as a template with the *PA1-1PA1-2* primers (KS2500 and KS2501) or the *PA2-2* primers (KS2486 and
568 KS2487), respectively. The sequences of all primers were listed in the KEY RESOURCES TABLE. All
569 mutant strains were verified by DNA sequencing.

570 **Widefield microscopy of cells and image analysis**

571 GFP-labeled proteins expressed in the cells were visualized using an Axioplan2 microscope (Carl
572 Zeiss,Jena, Germany) equipped with a 100x Plan-Neofluar oil immersion objective. Consistent culture
573 conditions, exposure times, and fluorescence intensities were maintained across all strains in this study to
574 ensure a comparative analysis of puncta intensity. Image analysis was performed using FIJI ImageJ
575 (https://imagej.nih.gov/ij/).

576 **Confocal microscopy of cells and image analysis**

577 GFP-labeled proteins expressed in the cells were imaged using both a ZEISS LSM900 laser scanning
578 confocal microscope (Carl Zeiss, Jena, Germany) equipped with high-sensitivity GaAsP-PMT detectors (2
579 standard and 1 additional GaAsP-PMT), and a ZEISS LSM980 confocal microscope with an Airyscan 2
580 detector (Carl Zeiss, Jena, Germany). For Airyscan super-resolution imaging with the LSM980, the Airyscan
581 Joint Deconvolution mode was utilized, achieving lateral resolution down to ~90 nm. Both systems were
582 fitted with a 63x/1.4 NA oil immersion objective, and all images were acquired at room temperature.
583 Microscope settings, including laser power, detector gain, and pinhole size, were kept identical for all
584 samples to ensure quantitative comparability. Image acquisition and processing were performed using
585 ZEISS Zen software (version 3.9, Carl Zeiss).

586 **FCS measurements and data analysis**

587 All FCS measurements were performed at 25°C on a confocal microscope (LSM780; Carl Zeiss, Inc.
588 Germany) combined with a ConfoCor3 and a 40×/1.2 NA water-immersion objective (Carl Zeiss, Inc.).
589 Details of the analysis of fluorescence auto-correlation functions (FAFs) were described in the previous
590 study (Kawai-Noma et al., 2006; Pack et al., 2014), FAFs were fitted to a two-component model with a
591 triplet term.

592 For each cell, the cytoplasmic region was identified by visual inspection of the fluorescence image, avoiding
593 the GFP visualized puncta. At least five independent measurements (each lasting 10 s) were recorded per
594 cell. Over 15 cells were analyzed per condition.

595 Autocorrelation curves were generated using ZEN black software (Carl Zeiss, Inc.) and fitted with two-
596 component 3D diffusion model including a triplet term:

597 $$G_x(\tau) = 1 + \frac{1}{N}\sum_i F_i(1+\frac{\tau}{\tau_i})^{-1}(1+\frac{\tau}{s^2\tau_i})^{-1/2}$$

598 Where F_i and τ_i are the fraction and diffusion time of component I, respectively; N is the average number
599 of fluorescent molecules in the confocal volume defined by the radius w_0 and the length $2z_0$; and s is the
600 structure parameter representing the ratio $s = z_0/w_0$ (axial/lateral radius ratio of the confocal volume). The
601 structural parameter was calibrated using a known concentration of Rh6G standard solution at room
602 temperature. The relationship between absolute concentration and calculated N was calibrated using a
603 known concentration of Rh6G or recombinant mGFP solution. The effect of photobleaching on evaluation
604 of concentration was determined according to a previous study. Fluoprescence correlation functions (FCFs)
605 in live cells were measured sequentially 6 times with duration of 10s to minimize photobleaching effect.

606 The cytoplasmic concentration of the target protein was calculated as

607 $$C = \frac{N}{N_A V_{eff}}$$

608 Where N_A is Avogadro's number and V_{eff} is the effective confocal volume determined from calibration
609 measurements with Rhodamine 6G solutdion.

610 **Fluorescence recovery after photobleaching (FRAP) in living yeast cells**

611 Fluorescence recovery after photobleaching (FRAP) was performed on puncta induced by GAL promoter
612 using a Zeiss LSM900 laser scanning confocal microscope with a 100×/1.40 NA oil immersion objective
613 (Carl Zeiss AG, Oberkochen, Germany). Cells were mounted on agarose pads, composed of SC 2%
614 raffinose/ 2% galactose media and 1~3% agarose, to minimize the delicate movements of cells. For the
615 confocal imaging, 0.6% 488 nm wavelength laser and GaAsP-PMT detector were used. Due to the low
616 GFP signals of proteins and the small size of yeast, the pinhole was opened to 3 Airy units, about 240 μm.
617 For fast imaging, the acquisition mode was set to 512 px X 512 px frame size, 8 bits per pixel, 9 (about 1
618 μs of pixel times) scan speed, one-way, and none averaging scanning. For the FRAP experiments, the
619 region of interest (ROI) was selected, and 200 cycles with no interval of time series were set. After snapping

620 five images, bleaching on ROI was performed repeatedly three times with the power of 10~100% 488 nm
621 laser beam. Bleached signals on ROI were recovered, and these signals were acquired for the left 194
622 cycles. All the experiment was repeated about 20~30 foci of each strain. If the foci were out of focus for
623 200 cycles, these data were discarded.

624 **Image analysis for FRAP**

625 The mean intensity in ROI at each cycle was analyzed and drawn as graphs using Fiji with the Stowers
626 plugin. All the graphs were normalized to 0-1, and the average curves of these graphs were calculated
627 with GraphPad Prism 10 (GraphPad Software, CA, USA). These normalized curves were fitted with Eq.1.

628 $$y = y_{max} \times (1 - e^{-\frac{t}{\tau}}) \quad (1)$$

629 In Eq.1, y_{max} is the y value at infinite time ($t \approx \infty$), and τ (tau) is the time point when the y value is equal
630 to 63.2% of y_{max} value. The first derivative functions of the fitted curves were analyzed with GraphPad
631 Prism 10 to calculate the maximum velocity of the recovery curves.

632 **Fixation and DAPI staining of yeast cells**

633 Following 4 hours of galactose-mediated induction, yeast cells were harvested by centrifugation at 4,000
634 rpm for 5 minutes at RT. The supernatant was carefully removed, and cell pellets were resuspended in 4%
635 paraformaldehyde (PFA) dissolved in Dulbecco's phosphate-buffered saline (DPBS) (T&I, South Korea,
636 BPP-9004) for fixation by gentle inversion mixing for 1 h at RT. To remove residual PFA, cells were
637 subjected to two successive wash cycles consisting of centrifugation (4,000 rpm, 2 minutes) and
638 resuspension in fresh DPBS (Welgene, South Korea, LB 001-02). The final cell pellet was reconstituted in
639 DPBS and evenly distributed onto microscope slides. Vectashield mounting medium for fluorescence with
640 DAPI (Vector Laboratories, Inc., USA, H-1200) was applied to each sample, followed by gentle mixing using
641 a pipette tip to ensure homogeneous distribution of cells. Cellular morphology and fluorescence signals
642 were subsequently analyzed using a Axioplan2 microscope (Carl Zeiss, Jena, Germany) equipped with a
643 DAPI-specific filter set.

644 **U2OS cell culture and transfection**

645 U2OS cells (ATCC, CRL-1427, HTB 96, Manassas, VA, USA) were cultured in Dulbecco's Modified Eagle
646 Medium (DMEM with high glucose; Cytiva, USA SH30023.01) supplemented with 10% fetal bovine serum
647 (FBS; Cytiva, USA, SH30088.03) and 1X antibiotic-antimycotic solution (Anti-Anti; Gibco, USA ,15240-062)
648 at 37°C in a humidified incubator with 5% CO_2. Once the cells reached 70% confluence, they were
649 transfected with pcDNA3.1-myc-hisA expression vectors encoding GFP-TDP-43, its IDR deletion mutants
650 and charge neutralized mutants using Lipofectamine 3000 (Invitrogen, USA, L300015), following the
651 manufacturer's protocol. After transfection, the cells were selected with 600 ng/μL Geneticin™ Selective
652 Antibiotic (G418 Sulfate) （Gibco, USA, 10131035）.

653 **Fixation and DAPI staining of U2OS cells**

654 Forty-eight hours after transfection, U2OS cells cultured on a cover slide were fixed with 4%
655 paraformaldehyde (PFA, T&I, South Korea, BPP-9004) at RT for 1 h, washed three times with phosphate-
656 buffered saline (PBS, WELGENE, South Korea, LB 001-02)., and mounted using a DAPI-containing
657 mounting solution (Vector Laboratories, Inc., USA, H-1200). Fluorescence images were acquired using an
658 Axioplan2 fluorescence microscope (Carl Zeiss, Jena, Germany) equipped with a 20x/0.5 Ph2 Plan-
659 Neofluar objective.

660 **Western blotting analysis**

661 Protein extraction from yeast cells was obtained using the alkaline lysis as described in Choi and Song
662 （*Int. J. Mol. Sci. 2022*, *23*, 2501）U2OS cell extract was obtained as previously described (PLOS ONE |
663 https://doi.org/10.1371/journal.pone.0302936 May 7, 2024). Protein samples were separated by sodium
664 dodecyl sulfate–polyacrylamide gel electrophoresis (SDS-PAGE) and transferred onto polyvinylidene
665 difluoride (PVDF) membranes (Merck Millipore, Burlington, MA, USA) using a semi-dry transfer system.
666 Anti-GFP antibody (600-101-215 ROCKLAND, Limerick, PA, USA, 1:1000 dilution) was used for Western
667 blotting. To confirm equal protein loading, the membranes were stripped of the anti-GFP antibody prior to
668 re-probing with an anti-Tubulin antibody anti-Tubulin (Mouse, Sigma-Aldrich, Cat# T5168, 1:10000 dilution)
669 and subsequently with HRP-conjugated anti-mouse secondary antibody (Santa Cruz Biotechnology, Cat#
670 sc-2005, 1:10000 dilution).

QUANTIFICATION AND STATISTICAL ANALYSIS

Only statistically analyzed data are shown as mean ± SEM. Statistical analyses were performed using GraphPad Prism. Statistical significance was determined using unpaired two-tailed Student's t-test with Welch's correction. $P < 0.05$ was considered statistically significant.

DATA AND CODE AVAILABILITY

Custom algorithms were implemented in Python 3.10 by the authors. The analysis pipeline included modules written with NumPy and SciPy and was used to process experimental data shown in Figure 1. The code used in this study was written by the authors and is available from the corresponding author upon reasonable request.

ADDITIONAL RESOURCES

N/A

DISCLOSURE

A preprint version of this manuscript is available on bioRxiv (DOI:)

DECLARATION OF INTERESTS

The authors (K.S., Y.J.C., S.C., and Y.P.) have applied for a patent entitled "Specific Amino Acid Sequence Deletion Mutants for Inhibiting TDP-43 Aggregation Causing Degenerative Brain Diseases, and Method for Identifying Mutant Sequences (DP 2025-0349)" with the Korean Intellectual Property Office. The authors declare no other competing interests.

694 **ACKNOWLEDGMENTS**

695 We thank the Cellular Imaging Core Facility at the ConveRgence mEDIcine research cenTer (CREDIT),
696 Asan Medical Center, for technical support. The authors would like to thank Ewha Women's University
697 Fluorescence Core Imaging Center for valuable guidance in FRAP analysis. We specially appreciate the
698 technical assistance provided by professor Dongmin Kang, the Director, and Research Technician Sinae
699 Jang, of Ewha Fluorescence Core Imaging Center. TDP-43 gene clone was kindly provided by Dr. Hyung-
700 Jun Kim in Korea Brain Research Institute. This work was in part supported by the National Research
701 Foundation of Korea (NRF) grant provided to K. Song (RS-2023-00243284).

702

703 **AUTHOR CONTRIBUTIONS**

704 Conceptualization, K.S. and Y.J.C.; methodology, K.S., Y.J.C, and C.P.; Investigation, Y.J.C, Y.L., S.C.,
705 and Y.P.; writing—original draft, K.S. and Y.J.C.; writing—review & editing, K.S., Y.J.C, C.P, and Y.J.;
706 funding acquisition, K.S.; resources, K.S. and C.K.B.; supervision, K.S., and Y.J.C

707

708 **REFERENCES**

709 Afroz, T., Hock, E.M., Ernst, P., Foglieni, C., Jambeau, M., Gilhespy, L.A.B., Laferriere, F., Maniecka, Z.,
710 Pluckthun, A., Mittl, P., et al. (2017). Functional and dynamic polymerization of the ALS-linked protein
711 TDP-43 antagonizes its pathologic aggregation. Nat Commun *8*, 45. 10.1038/s41467-017-00062-0.
712 Ahmad, A., Uversky, V.N., and Khan, R.H. (2022). Aberrant liquid-liquid phase separation and amyloid
713 aggregation of proteins related to neurodegenerative diseases. Int J Biol Macromol *220*, 703-720.
714 10.1016/j.ijbiomac.2022.08.132.
715 Alberti, S., and Hyman, A.A. (2021). Biomolecular condensates at the nexus of cellular stress, protein
716 aggregation disease and ageing. Nat Rev Mol Cell Biol *22*, 196-213. 10.1038/s41580-020-00326-6.
717 Alshareedah, I., Borcherds, W.M., Cohen, S.R., Singh, A., Posey, A.E., Farag, M., Bremer, A., Strout, G.W.,
718 Tomares, D.T., Pappu, R.V., et al. (2024). Sequence-specific interactions determine viscoelasticity and
719 aging dynamics of protein condensates. Nat Phys *20*, 1482-1491. 10.1038/s41567-024-02558-1.
720 Alshareedah, I., Moosa, M.M., Pham, M., Potoyan, D.A., and Banerjee, P.R. (2021). Programmable
721 viscoelasticity in protein-RNA condensates with disordered sticker-spacer polypeptides. Nat Commun
722 *12*, 6620. 10.1038/s41467-021-26733-7.
723 Austin, J.A., Wright, G.S., Watanabe, S., Grossmann, J.G., Antonyuk, S.V., Yamanaka, K., and Hasnain, S.S.
724 (2014). Disease causing mutants of TDP-43 nucleic acid binding domains are resistant to aggregation and
725 have increased stability and half-life. Proc Natl Acad Sci U S A *111*, 4309-4314.
726 10.1073/pnas.1317317111.

727 Banani, S.F., Afeyan, L.K., Hawken, S.W., Henninger, J.E., Dall'Agnese, A., Clark, V.E., Platt, J.M., Oksuz,
728 O., Hannett, N.M., Sagi, I., et al. (2022). Genetic variation associated with condensate dysregulation in
729 disease. Dev Cell *57*, 1776-1788 e1778. 10.1016/j.devcel.2022.06.010.
730 Banani, S.F., Lee, H.O., Hyman, A.A., and Rosen, M.K. (2017). Biomolecular condensates: organizers of
731 cellular biochemistry. Nat Rev Mol Cell Biol *18*, 285-298. 10.1038/nrm.2017.7.
732 Banjade, S., and Rosen, M.K. (2014). Phase Transitions of Multivalent Proteins Can Promote Clustering of
733 Membrane Receptors. Elife *3*. ARTN e04123

734 10.7554/eLife.04123.
735 Berry, J., Weber, S.C., Vaidya, N., Haataja, M., and Brangwynne, C.P. (2015). RNA transcription
736 modulates phase transition-driven nuclear body assembly. Proc Natl Acad Sci U S A *112*, E5237-5245.
737 10.1073/pnas.1509317112.
738 Biswas, S., and Potoyan, D.A. (2024). Decoding Biomolecular Condensate Dynamics: An Energy
739 Landscape Approach. bioRxiv. 10.1101/2024.09.24.614805.
740 Borcherds, W., Bremer, A., Borgia, M.B., and Mittag, T. (2021). How do intrinsically disordered protein
741 regions encode a driving force for liquid-liquid phase separation? Curr Opin Struc Biol *67*, 41-50.
742 10.1016/j.sbi.2020.09.004.
743 Brangwynne, C.P., Eckmann, C.R., Courson, D.S., Rybarska, A., Hoege, C., Gharakhani, J., Jülicher, F., and
744 Hyman, A.A. (2009). Germline P Granules Are Liquid Droplets That Localize by Controlled
745 Dissolution/Condensation. Science *324*, 1729-1732. 10.1126/science.1172046.
746 Chen, H.J., Topp, S.D., Hui, H.S., Zacco, E., Katarya, M., McLoughlin, C., King, A., Smith, B.N., Troakes, C.,
747 Pastore, A., and Shaw, C.E. (2019). RRM adjacent TARDBP mutations disrupt RNA binding and enhance
748 TDP-43 proteinopathy. Brain *142*, 3753-3770. 10.1093/brain/awz313.
749 Chien, H.M., Lee, C.C., and Huang, J.J. (2021). The Different Faces of the TDP-43 Low-Complexity
750 Domain: The Formation of Liquid Droplets and Amyloid Fibrils. Int J Mol Sci *22*. 10.3390/ijms22158213.
751 Choi, C.H., Lee, D.S.W., Sanders, D.W., and Brangwynne, C.P. (2024). Condensate interfaces can
752 accelerate protein aggregation. Biophysical Journal *123*, 1404-1413. 10.1016/j.bpj.2023.10.009.
753 Choi, J.M., Holehouse, A.S., and Pappu, R.V. (2020). Physical Principles Underlying the Complex Biology
754 of Intracellular Phase Transitions. Annu Rev Biophys *49*, 107-133. 10.1146/annurev-biophys-121219-
755 081629.
756 Choi, Y.J., Lee, Y., Lin, Y., Heo, Y., Lee, Y.H., and Song, K. (2022). The Multivalent Polyampholyte Domain
757 of Nst1, a P-Body-Associated Saccharomyces cerevisiae Protein, Provides a Platform for Interacting with
758 P-Body Components. Int J Mol Sci *23*. 10.3390/ijms23137380.
759 Conicella, A.E., Zerze, G.H., Mittal, J., and Fawzi, N.L. (2016). ALS Mutations Disrupt Phase Separation
760 Mediated by α-Helical Structure in the TDP-43 Low-Complexity C-Terminal Domain. Structure *24*, 1537-
761 1549. 10.1016/j.str.2016.07.007.
762 Dickson, Z.W., and Golding, G.B. (2022). Low Complexity Regions in Mammalian Proteins are Associated
763 with Low Protein Abundance and High Transcript Abundance. Mol Biol Evol *39*.
764 10.1093/molbev/msac087.
765 Fondon, J.W., 3rd, and Garner, H.R. (2004). Molecular origins of rapid and continuous morphological
766 evolution. Proc Natl Acad Sci U S A *101*, 18058-18063. 10.1073/pnas.0408118101.
767 Fushimi, K., Long, C., Jayaram, N., Chen, X., Li, L., and Wu, J.Y. (2011). Expression of human FUS/TLS in
768 yeast leads to protein aggregation and cytotoxicity, recapitulating key features of FUS proteinopathy.
769 Protein Cell *2*, 141-149. 10.1007/s13238-011-1014-5.
770 Gao, G., Sumrall, E.S., Pitchiaya, S., Bitzer, M., Alberti, S., and Walter, N.G. (2023). Biomolecular
771 condensates in kidney physiology and disease. Nat Rev Nephrol *19*, 756-770. 10.1038/s41581-023-
772 00767-0.

773 Gruijs da Silva, L.A., Simonetti, F., Hutten, S., Riemenschneider, H., Sternburg, E.L., Pietrek, L.M., Gebel,
774 J., Dotsch, V., Edbauer, D., Hummer, G., et al. (2022). Disease-linked TDP-43 hyperphosphorylation
775 suppresses TDP-43 condensation and aggregation. EMBO J *41*, e108443. 10.15252/embj.2021108443.
776 Hurtle, B.T., Xie, L., and Donnelly, C.J. (2023). Disrupting pathologic phase transitions in
777 neurodegeneration. J Clin Invest *133*. 10.1172/JCI168549.
778 Imaizumi, K., Ideno, H., Sato, T., Morimoto, S., and Okano, H. (2022). Pathogenic Mutation of TDP-43
779 Impairs RNA Processing in a Cell Type-Specific Manner: Implications for the Pathogenesis of ALS/FTLD.
780 eNeuro *9*. 10.1523/ENEURO.0061-22.2022.
781 Johnson, B.S., McCaffery, J.M., Lindquist, S., and Gitler, A.D. (2008). A yeast TDP-43 proteinopathy
782 model: Exploring the molecular determinants of TDP-43 aggregation and cellular toxicity. Proc Natl Acad
783 Sci U S A *105*, 6439-6444. 10.1073/pnas.0802082105.
784 Kawai-Noma, S., Ayano, S., Pack, C.G., Kinjo, M., Yoshida, M., Yasuda, K., and Taguchi, H. (2006).
785 Dynamics of yeast prion aggregates in single living cells. Genes Cells *11*, 1085-1096. 10.1111/j.1365-
786 2443.2006.01004.x.
787 Li, Q., Babinchak, W.M., and Surewicz, W.K. (2021). Cryo-EM structure of amyloid fibrils formed by the
788 entire low complexity domain of TDP-43. Nat Commun *12*, 1620. 10.1038/s41467-021-21912-y.
789 Linsenmeier, M., Faltova, L., Morelli, C., Capasso Palmiero, U., Seiffert, C., Kuffner, A.M., Pinotsi, D.,
790 Zhou, J., Mezzenga, R., and Arosio, P. (2023). The interface of condensates of the hnRNPA1 low-
791 complexity domain promotes formation of amyloid fibrils. Nat Chem *15*, 1340-1349. 10.1038/s41557-
792 023-01289-9.
793 Lu, B., Qiu, R., Wei, J., Wang, L., Zhang, Q., Li, M., Zhan, X., Chen, J., Hsieh, I.Y., Yang, C., et al. (2024).
794 Phase separation of phospho-HDAC6 drives aberrant chromatin architecture in triple-negative breast
795 cancer. Nat Cancer. 10.1038/s43018-024-00816-y.
796 Lu, S., Hu, J., Arogundade, O.A., Goginashvili, A., Vazquez-Sanchez, S., Diedrich, J.K., Gu, J., Blum, J.,
797 Oung, S., Ye, Q., et al. (2022). Heat-shock chaperone HSPB1 regulates cytoplasmic TDP-43 phase
798 separation and liquid-to-gel transition. Nat Cell Biol *24*, 1378-1393. 10.1038/s41556-022-00988-8.
799 Mehta, S., and Zhang, J. (2022). Liquid-liquid phase separation drives cellular function and dysfunction in
800 cancer. Nat Rev Cancer *22*, 239-252. 10.1038/s41568-022-00444-7.
801 Nam, J., and Gwon, Y. (2023). Neuronal biomolecular condensates and their implications in
802 neurodegenerative diseases. Front Aging Neurosci *15*, 1145420. 10.3389/fnagi.2023.1145420.
803 Niedner-Boblenz, A., Monecke, T., Hennig, J., Klostermann, M., Hofweber, M., Davydova, E., Gerber,
804 A.P., Anosova, I., Mayer, W., Muller, M., et al. (2024). Intrinsically disordered RNA-binding motifs
805 cooperate to catalyze RNA folding and drive phase separation. Nucleic Acids Res *52*, 14205-14228.
806 10.1093/nar/gkae1107.
807 Niu, X., Zhang, L., Wu, Y., Zong, Z., Wang, B., Liu, J., Zhang, L., and Zhou, F. (2023). Biomolecular
808 condensates: Formation mechanisms, biological functions, and therapeutic targets. MedComm (2020) *4*,
809 e223. 10.1002/mco2.223.
810 Outeiro, T.F., and Lindquist, S. (2003). Yeast cells provide insight into alpha-synuclein biology and
811 pathobiology. Science *302*, 1772-1775. 10.1126/science.1090439.
812 Pack, C.G. (2021). Application of quantitative cell imaging using label-free optical diffraction
813 tomography. Biophys Physicobiol *18*, 244-253. 10.2142/biophysico.bppb-v18.027.
814 Pack, C.G., Yukii, H., Toh-e, A., Kudo, T., Tsuchiya, H., Kaiho, A., Sakata, E., Murata, S., Yokosawa, H.,
815 Sako, Y., et al. (2014). Quantitative live-cell imaging reveals spatio-temporal dynamics and cytoplasmic
816 assembly of the 26S proteasome. Nat Commun *5*, 3396. 10.1038/ncomms4396.
817 Ranganathan, S., Liu, J., and Shakhnovich, E. (2022). Different states and the associated fates of
818 biomolecular condensates. Essays Biochem *66*, 849-862. 10.1042/EBC20220054.

819 Regy, R.M., Dignon, G.L., Zheng, W., Kim, Y.C., and Mittal, J. (2020). Sequence dependent phase
820 separation of protein-polynucleotide mixtures elucidated using molecular simulations. Nucleic Acids Res
821 *48*, 12593-12603. 10.1093/nar/gkaa1099.
822 Saar, K.L., Morgunov, A.S., Qi, R., Arter, W.E., Krainer, G., Lee, A.A., and Knowles, T.P.J. (2021). Learning
823 the molecular grammar of protein condensates from sequence determinants and embeddings. Proc Natl
824 Acad Sci U S A *118*. 10.1073/pnas.2019053118.
825 Saitoh, N., Spahr, C.S., Patterson, S.D., Bubulya, P., Neuwald, A.F., and Spector, D.L. (2004). Proteomic
826 analysis of interchromatin granule clusters. Mol Biol Cell *15*, 3876-3890. 10.1091/mbc.e04-03-0253.
827 Sanfeliu-Cerdan, N., Catala-Castro, F., Mateos, B., Garcia-Cabau, C., Ribera, M., Ruider, I., Porta-de-la-
828 Riva, M., Canals-Calderon, A., Wieser, S., Salvatella, X., and Krieg, M. (2023). A MEC-2/stomatin
829 condensate liquid-to-solid phase transition controls neuronal mechanotransduction during touch
830 sensing. Nat Cell Biol *25*, 1590-1599. 10.1038/s41556-023-01247-0.
831 Schneider-Poetsch, T., Ju, J., Eyler, D.E., Dang, Y., Bhat, S., Merrick, W.C., Green, R., Shen, B., and Liu, J.O.
832 (2010). Inhibition of eukaryotic translation elongation by cycloheximide and lactimidomycin. Nat Chem
833 Biol *6*, 209-217. 10.1038/nchembio.304.
834 Shen, Y., Chen, A., Wang, W., Shen, Y., Ruggeri, F.S., Aime, S., Wang, Z., Qamar, S., Espinosa, J.R.,
835 Garaizar, A., et al. (2023). The liquid-to-solid transition of FUS is promoted by the condensate surface.
836 Proc Natl Acad Sci U S A *120*, e2301366120. 10.1073/pnas.2301366120.
837 Shenoy, J., Lends, A., Berbon, M., Bilal, M., El Mammeri, N., Bertoni, M., Saad, A., Morvan, E., Grelard, A.,
838 Lecomte, S., et al. (2023). Structural polymorphism of the low-complexity C-terminal domain of TDP-43
839 amyloid aggregates revealed by solid-state NMR. Front Mol Biosci *10*, 1148302.
840 10.3389/fmolb.2023.1148302.
841 Sim, K.L., and Creamer, T.P. (2002). Abundance and distributions of eukaryote protein simple sequences.
842 Mol Cell Proteomics *1*, 983-995. 10.1074/mcp.m200032-mcp200.
843 Snead, W.T., and Gladfelter, A.S. (2019). The Control Centers of Biomolecular Phase Separation: How
844 Membrane Surfaces, PTMs, and Active Processes Regulate Condensation. Mol Cell *76*, 295-305.
845 10.1016/j.molcel.2019.09.016.
846 Sneideriene, G., Gonzalez Diaz, A., Adhikari, S.D., Wei, J., Michaels, T., Sneideris, T., Linse, S.,
847 Vendruscolo, M., Garai, K., and Knowles, T.P.J. (2025). Lipid-induced condensate formation from the
848 Alzheimer's Abeta peptide triggers amyloid aggregation. Proc Natl Acad Sci U S A *122*, e2401307122.
849 10.1073/pnas.2401307122.
850 Sood, A., and Zhang, B. (2024). Preserving condensate structure and composition by lowering sequence
851 complexity. Biophys J *123*, 1815-1826. 10.1016/j.bpj.2024.05.026.
852 Sun, Z., Diaz, Z., Fang, X., Hart, M.P., Chesi, A., Shorter, J., and Gitler, A.D. (2011). Molecular
853 determinants and genetic modifiers of aggregation and toxicity for the ALS disease protein FUS/TLS.
854 PLoS Biol *9*, e1000614. 10.1371/journal.pbio.1000614.
855 Sundaravadivelu Devarajan, D., Wang, J., Szala-Mendyk, B., Rekhi, S., Nikoubashman, A., Kim, Y.C., and
856 Mittal, J. (2024). Sequence-dependent material properties of biomolecular condensates and their
857 relation to dilute phase conformations. Nat Commun *15*, 1912. 10.1038/s41467-024-46223-w.
858 Teixeira, D., Sheth, U., Valencia-Sanchez, M.A., Brengues, M., and Parker, R. (2005). Processing bodies
859 require RNA for assembly and contain nontranslating mRNAs. RNA *11*, 371-382. 10.1261/rna.7258505.
860 Ukmar-Godec, T., Hutten, S., Grieshop, M.P., Rezaei-Ghaleh, N., Cima-Omori, M.S., Biernat, J.,
861 Mandelkow, E., Soding, J., Dormann, D., and Zweckstetter, M. (2019). Lysine/RNA-interactions drive and
862 regulate biomolecular condensation. Nat Commun *10*, 2909. 10.1038/s41467-019-10792-y.
863 Van Treeck, B., and Parker, R. (2018). Emerging Roles for Intermolecular RNA-RNA Interactions in RNP
864 Assemblies. Cell *174*, 791-802. 10.1016/j.cell.2018.07.023.
865 Visser, B.S., Lipinski, W.P., and Spruijt, E. (2024). The role of biomolecular condensates in protein
866 aggregation. Nat Rev Chem *8*, 686-700. 10.1038/s41570-024-00635-w.

867 Wang, A., Conicella, A.E., Schmidt, H.B., Martin, E.W., Rhoads, S.N., Reeb, A.N., Nourse, A., Ramirez
868 Montero, D., Ryan, V.H., Rohatgi, R., et al. (2018a). A single N-terminal phosphomimic disrupts TDP-43
869 polymerization, phase separation, and RNA splicing. EMBO J *37*. 10.15252/embj.201797452.
870 Wang, B., Zhang, L., Dai, T., Qin, Z., Lu, H., Zhang, L., and Zhou, F. (2021). Liquid-liquid phase separation
871 in human health and diseases. Signal Transduct Target Ther *6*, 290. 10.1038/s41392-021-00678-1.
872 Wang, J., Choi, J.M., Holehouse, A.S., Lee, H.O., Zhang, X., Jahnel, M., Maharana, S., Lemaitre, R.,
873 Pozniakovsky, A., Drechsel, D., et al. (2018b). A Molecular Grammar Governing the Driving Forces for
874 Phase Separation of Prion-like RNA Binding Proteins. Cell *174*, 688-699 e616. 10.1016/j.cell.2018.06.006.

875

Figure 1

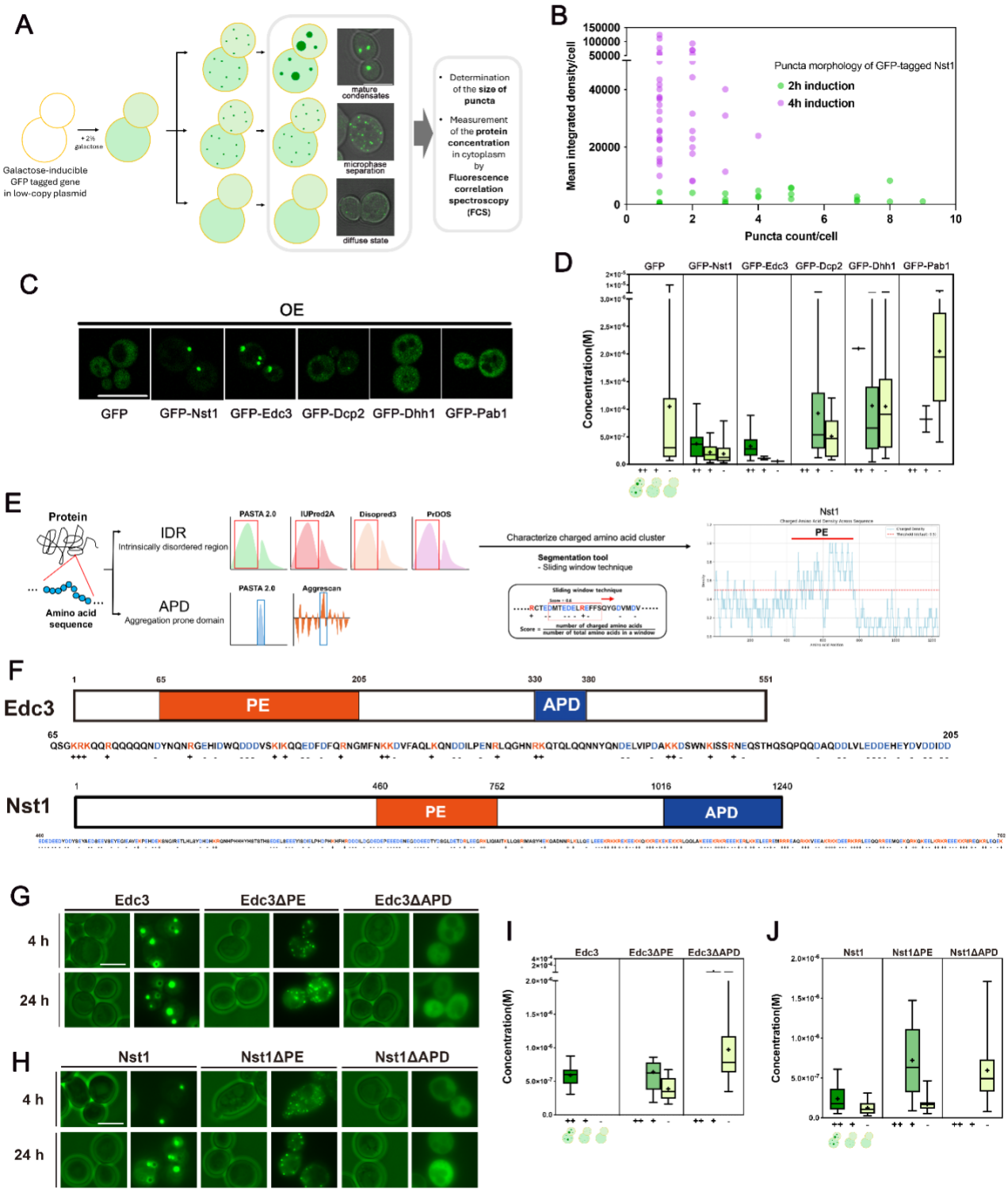
A
Galactose-inducible GFP tagged gene in low-copy plasmid
+2% galactose
mature condensates
microphase separation
diffuse state
Determination of the size of puncta
Measurement of the protein concentration in cytoplasm by Fluorescence correlation spectroscopy (FCS)
B
Mean integrated density/cell
Puncta count/cell
Puncta morphology of GFP-tagged Nst1
2h induction
4h induction
C
OE
GFP
GFP-Nst1
GFP-Edc3
GFP-Dcp2
GFP-Dhh1
GFP-Pab1
D
Concentration(M)
E
Protein
IDR
Intrinsically disordered region
APD
Aggregation prone domain
Amino acid sequence
PASTA 2.0
IUPred2A
Disopred3
PrDOS
Aggrescan
Characterize charged amino acid cluster
Segmentation tool
- Sliding window technique
Nst1
PE
F
Edc3
PE
APD
Nst1
PE
APD
G
Edc3
Edc3ΔPE
Edc3ΔAPD
4 h
24 h
H
Nst1
Nst1ΔPE
Nst1ΔAPD
4 h
24 h
I
Edc3
Edc3ΔPE
Edc3ΔAPD
Concentration(M)
J
Nst1
Nst1ΔPE
Nst1ΔAPD
Concentration(M)

876

877 **Figure 1.** ***Overexpression of Nst1 and Edc3 leads to mature condensate formation, whereas***
878 ***overexpression of their polyelectrolyte (PE) domain deletion mutants within the IDR maintains a***
879 ***stabilized microphase-separated state.***
880
881 (A) Schematic representation of budding yeast overexpression system to observe intracellular
882 condensates.

883 (B) Diagram of puncta generation pattern of cells overexpressing GFP tagged Nst1 for 2 h (green) and 4 h
884 (purple). *Δnst1* (YSK3490) cells transformed with pMW20-pGAL-GFP-NST1 were induced for 2 hours
885 (green) and 4 hours (purple) under the GAL promoter. Cells were imaged and analyzed; mean integrated
886 density and the number of puncta of each cell were measured and plotted.

887 (C-D) Representative fluorescence microscopy images and quantitative phase separation analysis of cells
888 overexpressing GFP and GFP-tagged Nst1, Edc3, Dcp3, Dhh1, and Pab1. (C) Scale bar: 10 μm. (D)
889 Cytoplasmic protein concentrations were measured via fluorescence correlation spectroscopy (FCS) as
890 described in Materials and Methods. The puncta formation patterns in cells were classified into three
891 categories: diffuse phase, microphase separation, and mature condensates. Box plot analysis of the
892 correlation between the pattern of protein puncta formation and cytoplasmic concentration was presented.

893 (E) Schematic representation of polyelectrolyte (PE) domain segmentation.

894 (F) Sequence diagram of Nst1 and Edc3. The red box indicates the polyelectrolyte (PE) region, while the
895 blue box represents the aggregation-prone domain (APD). Each sequence shown corresponds to the PE
896 region. Positively charged amino acids, lysine (K) and arginine (R),, are highlighted in red and marked with
897 a (+) sign below, whereas negatively charged amino acids, glutamic acid (E) and aspartic acid (D), are
898 highlighted in blue and marked with a (–) sign below.

899 (G) Fluorescence microscopy images showing puncta formation in cells overexpressing Edc3 and each
900 domain deletion mutant after 4 and 24 hours of galactose induction. In *Δedc3* cells (YSK3707), GFP-tagged
901 full-length Edc3 (pMW20-pGAL-GFP-EDC3), Edc3ΔPE (pMW20-pGAL-GFP-EDC3ΔPE), and Edc3ΔAPD

902 (pMW20-pGAL-GFP-EDC3ΔAPD) were overexpressed. Representative images were selected from an
903 average of more than 100 cells per strain at each time point. Scale bar: 5 μm.

904 (H) Fluorescence microscopy images showing puncta formation in cells expressing Nst1 and each Nst1
905 domain deletion mutant after 4 and 24 hours of induction as in (E). GFP-tagged full-length Nst1 (pMW20-
906 pGAL-GFP-NST1), Nst1ΔPE (pMW20-pGAL-GFP-NST1ΔPE), and Nst1ΔAPD (pMW20-pGAL-GFP-
907 NST1ΔAPD) were overexpressed in *Δnst1* (YSK3490) cells. Representative images were selected from an
908 average of more than 100 cells per strain at each time point. Scale bar: 5 μm.

909 (I) Box plot analysis of the correlation between the puncta formation pattern and cytoplasmic concentration
910 of the Edc3 and Edc3 derivatives. The puncta formation patterns in cells were classified into three
911 categories: diffuse phase, microphase separation, and mature condensates. Cytoplasmic concentrations
912 were measured in cells expressing each Edc3 domain deletion mutant after 4 hours of induction by
913 fluorescence correlation spectroscopy (FCS) as described in Materials and Methods. The measured
914 cytoplasmic concentrations of cells were analyzed with respect to puncta formation patterns.
915 (J) Box plot analysis of the correlation between the puncta formation pattern and cytoplasmic concentration
916 of the Nst1 and Nst1 derivatives. The cytoplasmic protein concentration measurement and puncta formation
917 analysis were performed same as (F).

Figure 2

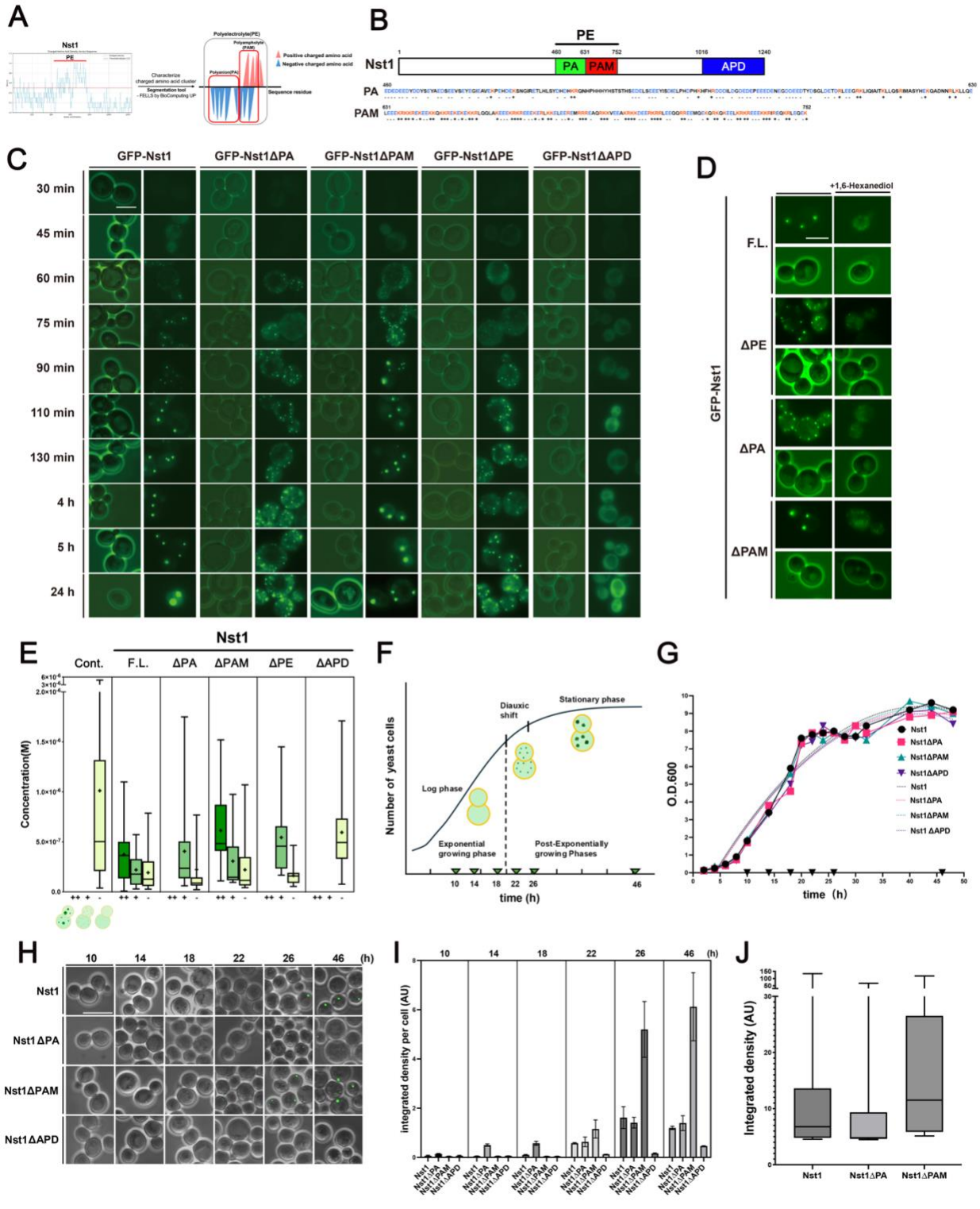
A
Nst1
PE
Characterize charged amino acid cluster
Segmentation tool - FELLS by BioComputing UP
Polyelectrolyte(PE)
Polyampholyte (PAM)
Polyanion(PA)
Positive charged amino acid
Negative charged amino acid
Sequence residue
B
PE
Nst1
PA
PAM
APD
C
GFP-Nst1
GFP-Nst1ΔPA
GFP-Nst1ΔPAM
GFP-Nst1ΔPE
GFP-Nst1ΔAPD
30 min
45 min
60 min
75 min
90 min
110 min
130 min
4 h
5 h
24 h
D
+1,6-Hexanediol
GFP-Nst1
F.L.
ΔPE
ΔPA
ΔPAM
E
Nst1
Cont.
F.L.
ΔPA
ΔPAM
ΔPE
ΔAPD
Concentration(M)
F
Number of yeast cells
Diauxic shift
Stationary phase
Log phase
Exponential growing phase
Post-Exponentially growing Phases
time (h)
G
O.D.600
Nst1
Nst1ΔPA
Nst1ΔPAM
Nst1ΔAPD
time (h)
H
10
14
18
22
26
46
(h)
Nst1
Nst1ΔPA
Nst1ΔPAM
Nst1ΔAPD
I
integrated density per cell (AU)
J
Integrated density (AU)
Nst1
Nst1ΔPA
Nst1ΔPAM

918

919 **Figure 2.** ***Polyanion (PA) domain of the Polyelectrolyte (PE) region specifically promotes the***
920 ***coalescence of Nst1 condensates, whereas the polyampholyte (PAM) domain in the PE region does***
921 ***not.***
922
923 (A) Schematic representation of Polyanion (PA) and Polyampholyte (PAM) domain segmentation with a
924 sliding window approach.
925 (B) Diagram of Nst1 with its domain architectures and sequences. The black line indicates the PE region,
926 while the green, red, and blue boxes denote the PA, PAM, and APD regions, respectively. The amino acid
927 sequences of the PA and PAM regions are shown below the diagram. Charges were annotated as
928 described in Figure 1D.

929 (C) Fluorescence microscopy images of condensate formation in cells overexpressing each GFP-tagged
930 Nst1 and its domain deletion mutants. Expression of GFP-tagged full-length Nst1 (pMW20-pGAL-GFP-
931 NST1) or NST1 lacking specific domains - Nst1ΔPE (pMW20-pGAL-GFP-NST1ΔPE), Nst1ΔPA (pMW20-
932 pGAL-GFP-NST1ΔPA), Nst1ΔPAM (pMW20-pGAL-GFP-NST1ΔPAM), and Nst1ΔAPD (pMW20-pGAL-
933 GFP-NST1ΔAPD) - was induced in *Δnst1* (YSK3490) cells. Each domain deletion mutant was
934 overexpressed by galactose induction for the indicated time periods. At each time point, fluorescence
935 images were collected from at least 100 cells to ensure representativeness. Scale bar: 5 μm.

936 (D) Fluorescence microscopy images of GFP-tagged Nst1 condensates induced for 4 hours, followed by a
937 1-hour treatment with 1,6-hexanediol. Scale bar: 5 μm.

938 (E) Box plot analysis of the correlation between the puncta formation pattern and cytoplasmic concentration
939 of cells overexpressing GFP-tagged Nst1, Nst1ΔPA, Nst1ΔPAM, Nst1ΔPE, and Nst1ΔAPD. Cytoplasmic
940 protein concentrations were measured via fluorescence correlation spectroscopy (FCS). The puncta
941 formation patterns in cells were classified into three categories: diffuse phase, microphase separation, and
942 mature condensates.

943 (F-J) Biomolecular condensate formation of endogenously expressed GFP-tagged Nst1, Nst1ΔPA,
944 Nst1ΔPAM and Nst1ΔAPD during chronological aging in yeast. (F) The growth phase diagram of general

945 budding yeast with observation time points designated. The inverted triangles (▼) on the x-axis represent
946 the observed time points (10, 14, 18, 22, 26, and 46 hours). (G) Line chart showing the optical densities
947 (O.D.600) of cell cultures endogenously expressing GFP-tagged Nst1, Nst1ΔPA, Nst1ΔPAM and
948 Nst1ΔAPD under native NST1 promoter. The growth of *Δnst1* (YSK3490) cells integrated with pRS306-
949 pNST1-GFP-NST1 full-length and various NST1 deletion mutants (YSK3700, YSK3701, YSK3702,
950 YSK3714) was monitored over time. The 10 h,14 h and 18 h time points represent the log phase, 22 h the
951 diauxic shift, and 26 h and 46 h the stationary phase. (H) Condensates were segmented using Fiji (ImageJ)
952 and visualized in green. Shown are GFP images merged with corresponding phase-contrast images. Scale
953 bar: 10 μm. (I) Bar plot showing the average integrated GFP fluorescence density per cell for each yeast
954 strain expressing full-length Nst1 and its deletion mutants (Nst1ΔPA, Nst1ΔPAM, Nst1ΔAPD), as shown in
955 (H). For each condition, more than 300 cells were analyzed using Fiji (ImageJ). Results are presented using
956 GraphPad Prism 10. (J) Box plot showing the integrated GFP intensity of condensates in stationary-phase
957 (46 h) yeast cells expressing Nst1, Nst1ΔPA and Nst1ΔPAM. For each condition, more than 300 cells were
958 quantified using Fiji (ImageJ). Data from three independent biological replicates were plotted with GraphPad
959 Prism 10.

Figure 3

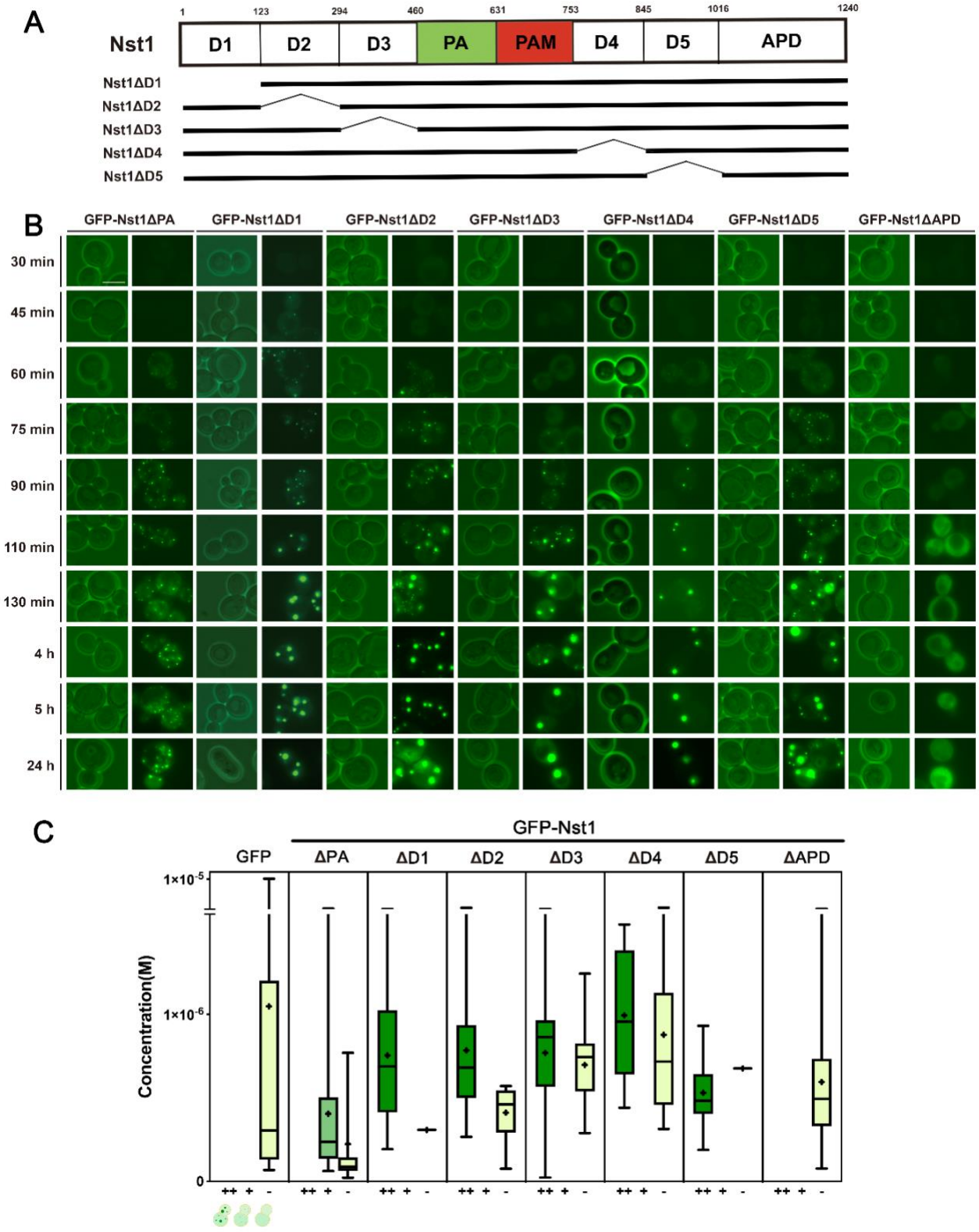
A
Nst1
D1
D2
D3
PA
PAM
D4
D5
APD
1
123
294
460
631
753
845
1016
1240
Nst1ΔD1
Nst1ΔD2
Nst1ΔD3
Nst1ΔD4
Nst1ΔD5
B
GFP-Nst1ΔPA
GFP-Nst1ΔD1
GFP-Nst1ΔD2
GFP-Nst1ΔD3
GFP-Nst1ΔD4
GFP-Nst1ΔD5
GFP-Nst1ΔAPD
30 min
45 min
60 min
75 min
90 min
110 min
130 min
4 h
5 h
24 h
C
GFP-Nst1
GFP
ΔPA
ΔD1
ΔD2
ΔD3
ΔD4
ΔD5
ΔAPD
Concentration(M)
1×10-5
1×10-6
0
++ + -

961 **Figure 3.** ***Polyanion (PA) domain exclusively functions in coalescence of Nst1 condensates.***

962

963 (A) A diagram of Nst1 with domain architectures. Residues 2-122 were designated as D1, 123-293 as D2,
964 294-459 as D3, 753-844 as D4, and 845-1015 as D5. The lengths of D1-D5 are similar to that of PA, and
965 all of the domains are comparable in size.

966 (B) Representative fluorescence microscopy images comparing time-dependent condensate formation in
967 the PA deletion mutant and other domain deletion mutants (ΔD1-D5, ΔAPD). In *Δnst1* (YSK3490) cells,
968 GFP-tagged Nst1ΔPA (pMW20-pGAL-GFP-NST1ΔPA), Nst1ΔD1 (pMW20-pGAL-GFP-NST1ΔD1),
969 Nst1ΔD2 (pMW20-pGAL-GFP-NST1ΔD2), Nst1ΔD3 (pMW20-pGAL-GFP-NST1ΔD3), Nst1ΔD4 (pMW20-
970 pGAL-GFP-NST1ΔD4), Nst1ΔD5 (pMW20-pGAL-GFP-NST1ΔD5), and Nst1ΔAPD (pMW20-pGAL-GFP-
971 NST1ΔAPD) were overexpressed. Overexpression of each Nst1 derivative was induced by galactose, and
972 images were obtained at the designated time point after the induction. Representative images were
973 selected among more than 100 cells. Scale bar: 5 μm.

974 (C) Box plot analysis showing the correlation between puncta formation patterns and cytoplasmic
975 concentrations in the cells overexpressing GFP-tagged Nst1, Nst1ΔPA, NstΔD1-ΔD5, and Nst1ΔAPD after
976 4 hours of induction. Cytoplasmic protein concentrations were measured via fluorescence correlation
977 spectroscopy (FCS). The puncta formation patterns in cells were classified into three categories: diffuse
978 phase, microphase separation, and mature condensates.

Figure 4

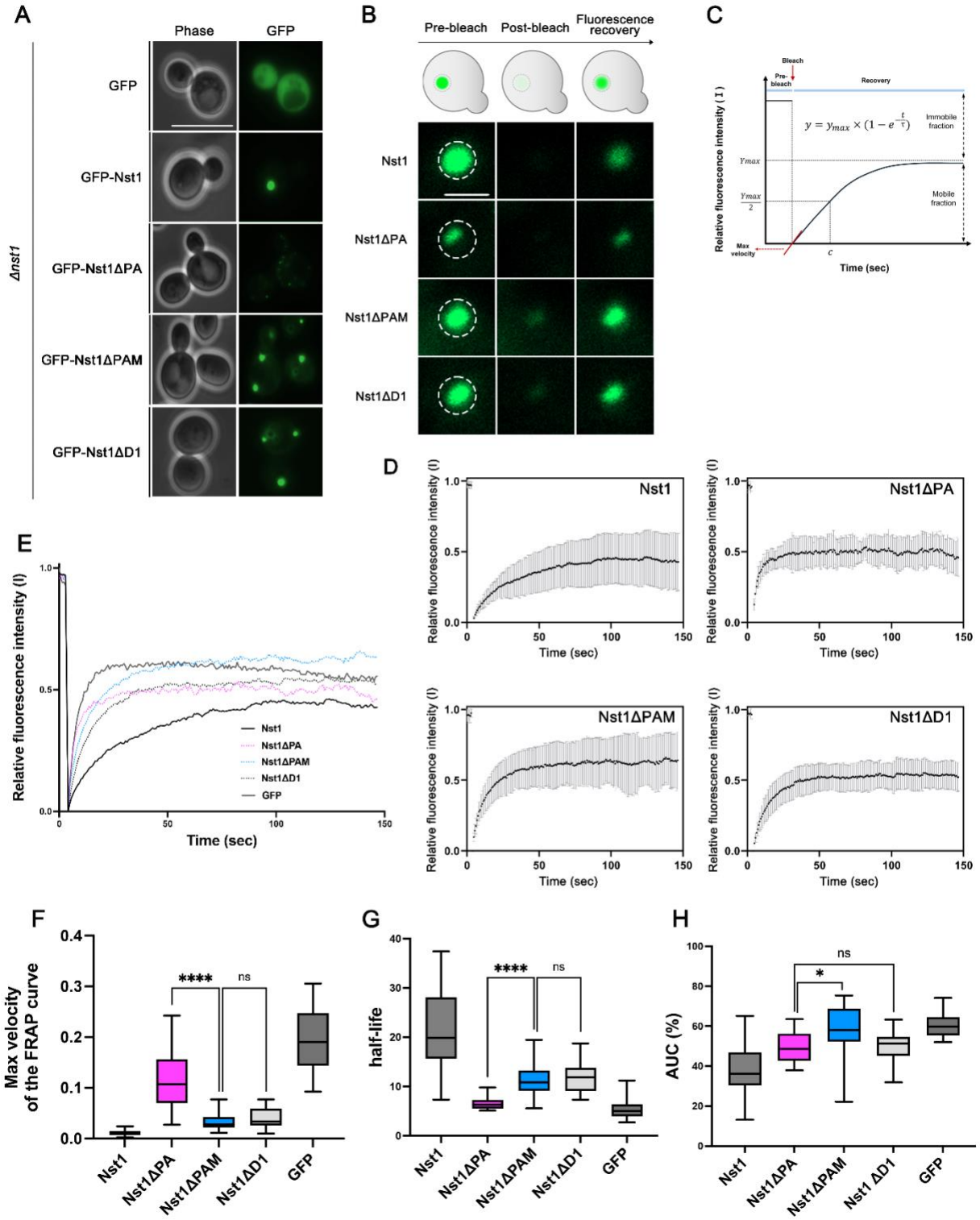
A
Phase
GFP
Δnst1
GFP
GFP-Nst1
GFP-Nst1ΔPA
GFP-Nst1ΔPAM
GFP-Nst1ΔD1
B
Pre-bleach
Post-bleach
Fluorescence recovery
Nst1
Nst1ΔPA
Nst1ΔPAM
Nst1ΔD1
C
Bleach
Pre-bleach
Recovery
Immobile fraction
Mobile fraction
Max velocity
Relative fluorescence intensity (I)
Time (sec)
D
Nst1
Nst1ΔPA
Nst1ΔPAM
Nst1ΔD1
Relative fluorescence intensity (I)
Time (sec)
E
Relative fluorescence intensity (I)
Time (sec)
Nst1
Nst1ΔPA
Nst1ΔPAM
Nst1ΔD1
GFP
F
Max velocity of the FRAP curve
****
ns
Nst1
Nst1ΔPA
Nst1ΔPAM
Nst1ΔD1
GFP
G
half-life
****
ns
Nst1
Nst1ΔPA
Nst1ΔPAM
Nst1ΔD1
GFP
H
AUC (%)
ns
*
Nst1
Nst1ΔPA
Nst1ΔPAM
Nst1 ΔD1
GFP

979

980 **Figure 4.** ***The polyanion (PA) domain of Nst1 enhances intermolecular interaction within***
981 ***condensates, whereas the polyampholyte (PAM) domain increases the rigidity of Nst1 condensates.***

982

983 (A-H) GAL promoter induction was performed for *Δnst1* (YSK3490) cells transformed with pMW20-pGAL -
984 GFP-NST1, pMW20-pGAL-GFP-NST1ΔPA, pMW20-pGAL-GFP-NST1ΔPAM, pMW20-pGAL-GFP-
985 NST1ΔD1. Fluorescence Recovery After Photobleaching (FRAP) experiments were performed on induced
986 condensates of these cells as described in Materials and Methods.

987 (A) Representative fluorescence microscopy images of cells overexpressing GFP-tagged full-length Nst1,
988 Nst1ΔPA, Nst1ΔPAM, Nst1ΔD1, and GFP alone (control) in the *Δnst1* strain. Scale bar: 10 μm.

989 (B) Representative fluorescence microscopy images at pre-beach point (cycle 1 of 200), post-bleach (cycle
990 6 of 200), and fluorescence recovery (cycle 200 of 200) during FRAP analysis. The stitched lines indicate
991 the region of interest (ROI) selected for bleaching the puncta in cells. All experiments were performed with
992 more than 20 puncta each. Scale bar: 1 μm.

993 (C) Predicted FRAP recovery curve modeled as a single exponential function. t is time, y_{max} is the y value
994 at infinite time ($t \approx \infty$), τ (tau) is the time point when the y value is equal to 63.2% of y_{max} value, and c is
995 half-life.

996 (D) The average FRAP recovery curves of Nst1 and its mutants shown in (B). Each graph for full-length
997 Nst1, Nst1ΔPA, Nst1ΔPAM, and Nst1ΔD1. The x-axis of these average graphs represents the time (sec)
998 taken in 200 cycles, and the y-axis indicates the relative fluorescence intensity.

999 (E) The average FRAP recovery curves for Nst1 and all Nst1 mutants in (D) were plotted together for direct
1000 comparison. Full-length Nst1 (black line), Nst1ΔPA (pink dotted line), Nst1ΔPAM (blue dotted line),
1001 Nst1ΔD1 (black dotted line), and GFP (grey line) as a control. The x-axis and y-axis represent the same
1002 values as in (D).

1003 (F) The maximum recovery rate of the FRAP curves for condensates of full-length Nst1, Nst1ΔPA,
1004 Nst1ΔPAM, and Nst1ΔD1. Akima spline interpolation was applied to all FRAP curves. For each Nst1
1005 mutant, the first derivative (slope) at the point of maximal recovery rate was calculated using GraphPad

1006 Prism 10. The y-axis represents the maximum recovery rate (maximum slope) of the fitted FRAP curve.
1007 Statistical significance was determined using unpaired two-tailed Student's t-test (**** $p<0.0001$) with
1008 Welch's correction. $P < 0.05$ was considered statistically significant.

1009 (G) The half-lives of FRAP curves for condensates of full-length Nst1, Nst1ΔPA, Nst1ΔPAM, and Nst1ΔD1.
1010 The x-values corresponding to half-maximal recovery ($y = 0.5$) were calculated and averaged using
1011 GraphPad Prism 10. Statistical significance was determined using unpaired two-tailed Student's t-test (****
1012 $p<0.0001$) with Welch's correction. $P < 0.05$ was considered statistically significant.

1013 (H) The area under the curve (AUC) of the FRAP recovery curves for condensates of full-length Nst1,
1014 Nst1ΔPA, Nst1ΔPAM, and Nst1ΔD1. The AUC was calculated for each normalized FRAP recovery curve
1015 using GraphPad Prism 10. Statistical significance was determined using unpaired two-tailed Student's t-
1016 test (* $p<0.01$) with Welch's correction. $P < 0.05$ was considered statistically significant.

Figure 5

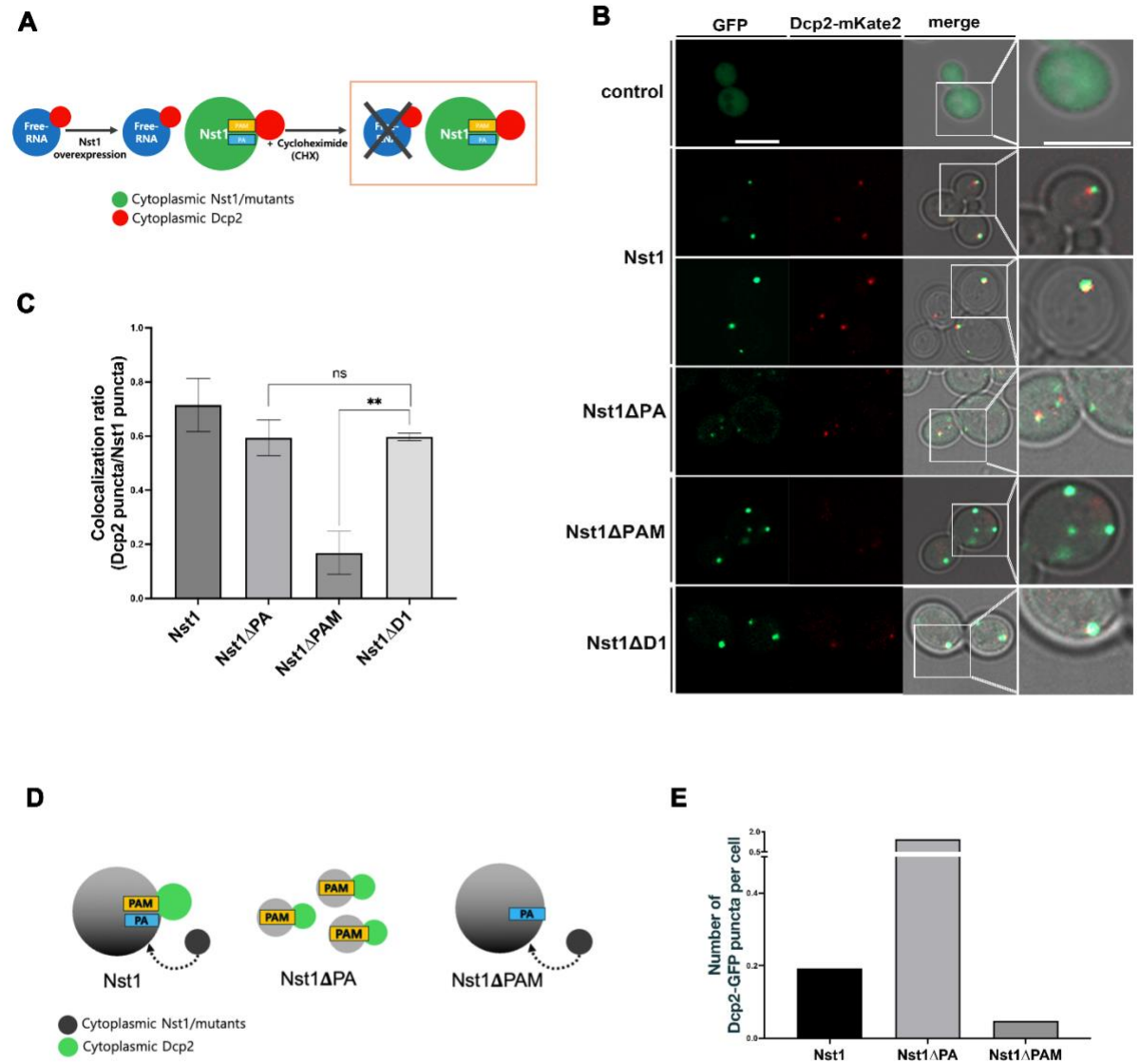

1017

1018 **Figure 5.** ***The PAM domain is an RNA-independent multivalent interaction domain for interaction***
1019 ***with the P-body component Dcp2.***
1020
1021 (A) Schematic representation of the experiments (B-C) designed to examine the effect of RNA on P-body
1022 condensate formation of Nst1 and its PA and PAM deletion mutants.

1023 (B) High-resolution confocal microscopy images showing the formation of mKate2-tagged Dcp2
1024 condensates induced by condensates of GFP-tagged Nst1, Nst1ΔPA, Nst1ΔPAM, and Nst1ΔD1. W303a
1025 *Δnst1* cells endogenously expressing Dcp2-mKate2 (YSK3663) were transformed with pMW20-pGAL-
1026 GFP-NST1, pMW20-pGAL-GFP-NST1ΔPA, pMW20-pGAL-GFP-NST1ΔPAM, or vector only (control).
1027 Following galactose induction for 4 hours, cells were treated with cycloheximide (CHX, 100 μg/ml) for 10
1028 minutes and imaged using a Zeiss LSM 980 confocal microscope equipped with an Airyscan 2 detector
1029 (Carl Zeiss). The right panel shows a 2× magnified view of selected puncta in the merged images. GFP
1030 and mKate2 channels are shown in green and red, respectively. Scale bar: 5 μm. Representative images
1031 are shown.

1032 (C) Quantitative analysis of the spatial co-localization between Dcp2 and Nst1 condensates shown in (B)
1033 after CHX-treatment. The co-localization ratio was calculated as the proportion of Dcp2 condensates
1034 overlapping with Nst1 and its mutants-derived puncta. Puncta were segmented and quantified using Fiji
1035 (ImageJ) software. For each Nst1 and its mutants, at least 100 condensates were analyzed per experiment
1036 across three independent replicates. Statistical significance was determined by unpaired t-test
1037 (***$p < 0.001$) using GraphPad Prism 10.

1038 (D) Schematic representation of the proposed Dcp2 condensation model based on the functional roles of
1039 the PA and PAM domains of Nst1.

1040 (E) Quantification of Dcp2-EGFP puncta formation in yeast cells (YSK3709) imaged by widefield
1041 epifluorescence microscopy. Cells endogenously expressing Dcp2-EGFP were transformed to overexpress
1042 Nst1, Nst1ΔPA, or Nst1ΔPAM for 4 hours. Images were acquired using identical microscope settings for all
1043 conditions. Dcp2-EGFP puncta were segmented in FIJI (ImageJ) by intensity thresholding. The number of

puncta per cell was quantified and normalized by cell number, with more than 300 cells analyzed for each condition. Data are presented as bar graphs generated using GraphPad Prism 10.

Figure 6

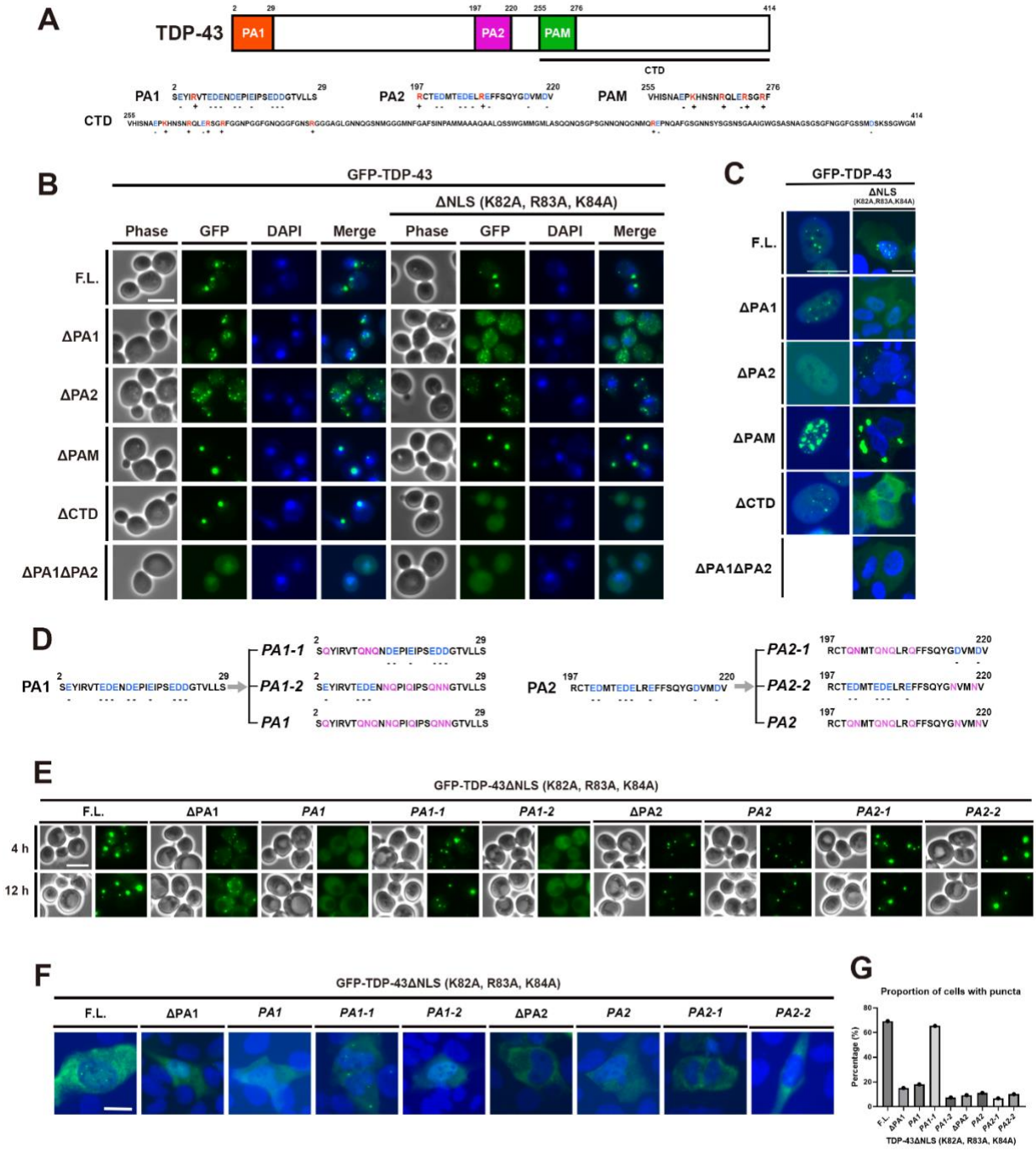

1046

1047 **Figure 6.** ***The Polyanion (PA) domain of Edc3 and human TDP-43 promote coalescence of***

1048 ***condensates, similar to Nst1.***

1049

1050 (A) Schematic representation of TDP-43 domain architecture. Residues 2–29 and 197–220 were identified
1051 as clusters of negatively charged amino acids, designated PA1 and PA2, based on a sliding window
1052 approach and prediction tools, as described in Supplementary Figure 3. The region spanning residue 255-
1053 276 was denoted as PAM, while residues 255-414 were characterized as the C-terminal domain. See also
1054 Supplementary figure 3.

1055 (B) Representative widefield fluorescence microscopy images of budding yeast (W303a) cells after 4 hours
1056 of overexpression of TDP-43 and its domain deletion mutants (ΔPA1, ΔPA2, ΔPAM, ΔCTD and ΔPA1ΔPA2)
1057 with or without NLS (Nuclear localization signal) sequence under a galactose-inducible promoter. Cells
1058 were fixed and stained with DAPI to visualize nuclei. Scale bar: 5 μm.

1059 (C) Representative wildfield fluorescence microscopy images of cells expressing GFP-tagged TDP-43 and
1060 its variants (ΔPA1, ΔPA2, ΔPAM, ΔCTD and ΔPA1ΔPA2) in U2OS cells at 48 hours after transfection.
1061 U2OS cells were transfected with plasmids encoding GFP-tagged TDP-43 variants under CMV promoter
1062 as described in Materials and Methods. After 48 hours, cells were observed using fluorescence microscopy
1063 to assess condensation pattern of each TDP-43 variant. Scale bar: 20 μm.

1064 (D) The amino acid sequence of the PA1 and PA2 domains of TDP-43, along with its *PA1-1, PA1-2, PA1,*
1065 *PA2-1, PA2-2,* and *PA2* mutant variants, is depicted at the top. In the *PA1-1, PA1-2, PA1, PA2-1, PA2-2,*
1066 and *PA2* mutants, the negatively charged glutamic acid (E) and aspartic acid (D) residues were individually
1067 substituted with glutamine (Q) and asparagine (N), respectively, as indicated.

1068 (E) Representative widefield fluorescence microscopy images are shown for budding yeast (W303a) cells
1069 overexpressing ΔNLS TDP-43 full-length (F.L.), each PA domain deletion mutants (ΔPA1 and ΔPA2), as
1070 well as the *PA1, PA1-1, PA1-2, PA2, PA2-1*, and *PA2-2* variants, all of which lack the NLS. Images were

1071 taken following 4 and 12 hours of galactose induction. For each strain and time point, more than 100 cells
1072 were examined, and representative images are presented. Scale bar: 5 μm.

1073 (F) Representative fluorescence microscopy images of U2OS cells expressing GFP-tagged ΔNLS TDP-43
1074 and its variants (ΔPA1, *PA1*, *PA1-1*, *PA1-2*, ΔPA2, *PA2*, *PA2-1* and *PA2-2*) 48 hours post-transfection.
1075 U2OS cells were transfected with plasmids encoding each GFP-tagged ΔNLS TDP-43 construct under the
1076 control of the CMV promoter, as detailed in the Materials and Methods. After 48 hours, cells were imaged
1077 by fluorescence microscopy to evaluate the condensation behavior of each variant.

1078 (G) Bar plot showing the percentage of cells containing TDP-43 puncta in U2OS cells expressing TDP-43
1079 lacking the NLS and its charge-removal mutants. Scale bar, 20 μm.

1080 **Supplementary Figures**

Supplementary Figure 1

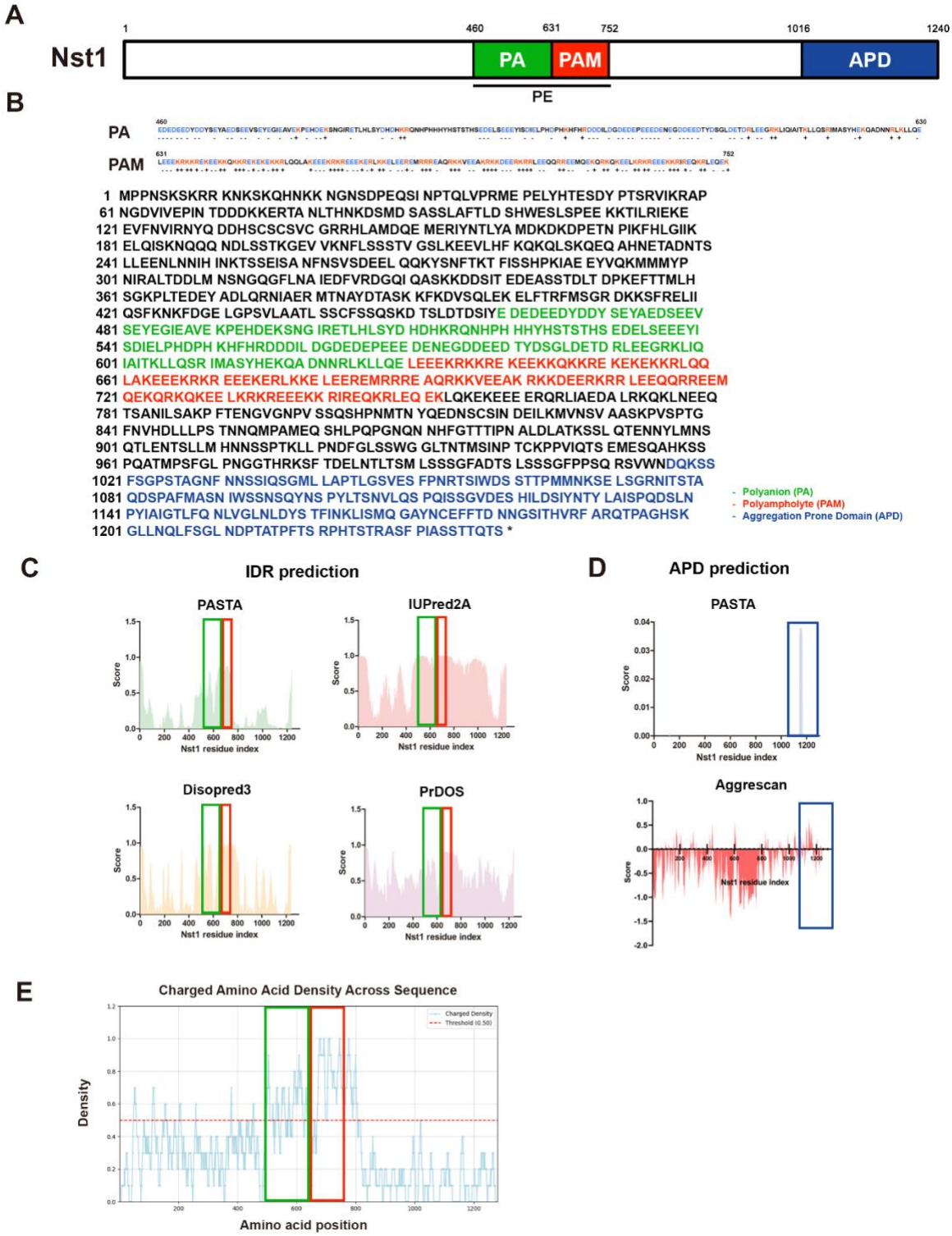

1083 (A) A diagram of Nst1 showing domain architecture predicted by prediction tools. The PE region spanning
1084 residues 460–752 is indicated by a black line, while the PA region (residues 460–630), PAM region
1085 (residues 631–752), and APD region (residues 1016–1240) are denoted by green, red, and blue,
1086 respectively.

1087 (B) Diagram illustrating the full amino acid sequence of Nst1, highlighting the charge-rich regions
1088 designated as PA and PAM. In the PA and PAM sequence shown above, lysine (K) and arginine (R)
1089 residues, which are positively charged, are indicated in red with a (+) sign shown beneath each residue,
1090 while negatively charged glutamic acid (E) and aspartic acid (D) residues are indicated in blue with a (–)
1091 sign displayed below. In the full-length sequence, the PA, PAM, and APD regions are highlighted in green,
1092 red, and blue, respectively.

1093 (C-D) Data analysis and graph generation were conducted using GraphPad Prism 5.

1094 (C) Prediction of Intrinsically Disordered Regions (IDRs) using multiple computational tools: PASTA 2.0
1095 (green), IUPred2A (pink), Disopred3 (yellow), and PrDOS (purple). Residues with scores > 0.5 consistently
1096 predicted by all four tools were classified as IDRs. The red box denotes the PAM region, while the green
1097 box indicates the PA region.

1098 (D) Prediction of Aggregation Prone Domains (APDs) utilizing PASTA 2.0 (blue) and Aggrescan (red).
1099 Regions exhibiting high positive scores were designated as APDs, as indicated by the blue box.

1100 (E) The density of charged amino acids along the Nst1 sequence was analyzed using a sliding window
1101 approach. A window of 10 consecutive amino acids was moved along each sequence in single-residue
1102 steps. For each window, the proportion of charged residues—defined as lysine (K), arginine (R), histidine
1103 (H), aspartic acid (D), and glutamic acid (E)—was calculated by dividing the number of these residues by
1104 the window size. Regions with a ratio equal to or greater than 0.5 were designated as high-density charged
1105 segments. The red and green boxes indicate the PAM and PA regions, respectively.

Supplementary Figure 2

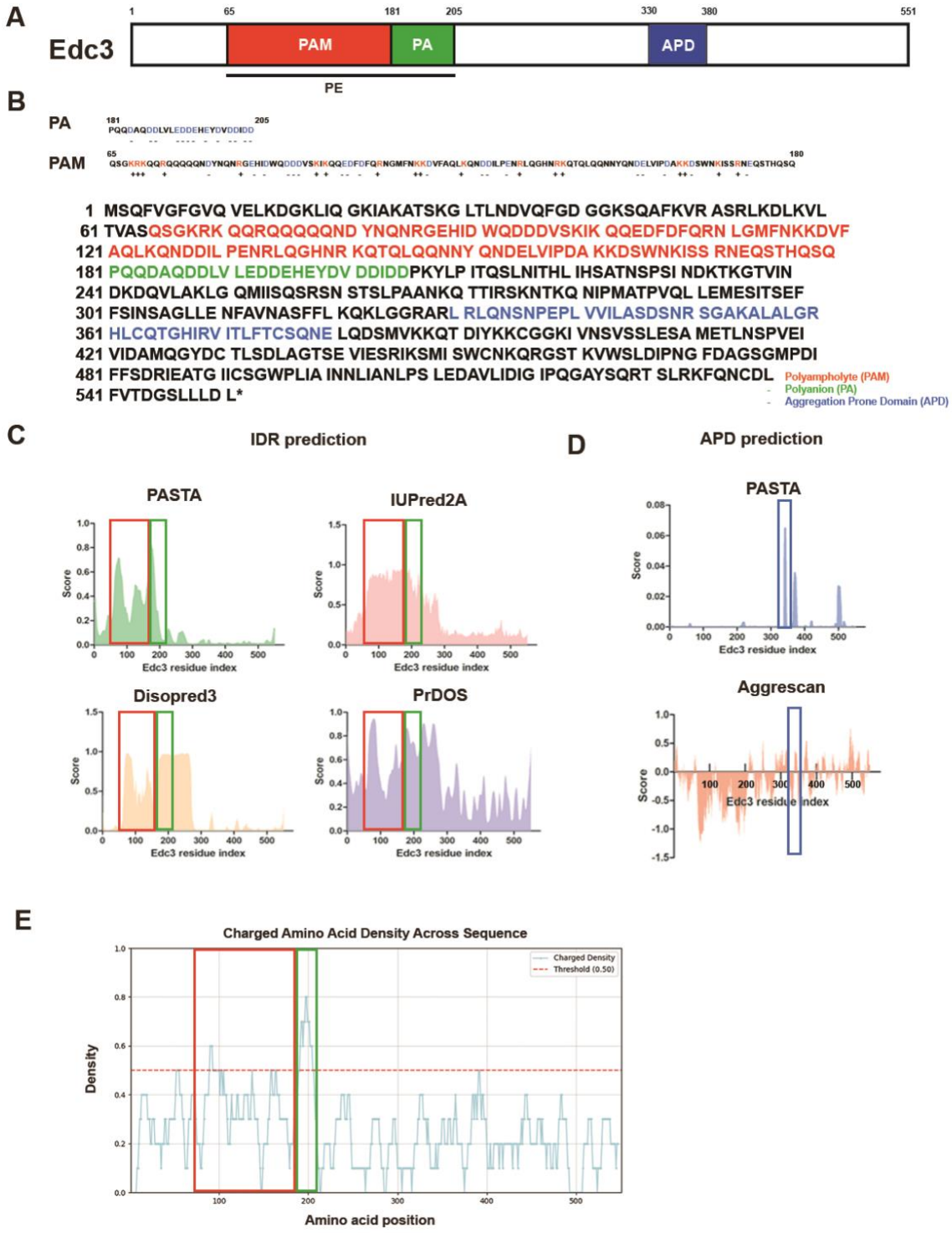

1106

1107 (A) Schematic representation of Edc3 domain organization as predicted by computational tools. The PE
1108 region (residues 65-205) is represented by a black line, whereas the PA (181-205), PAM (65-180), and
1109 APD (330-380) regions are highlighted in green, red, and blue, respectively.

1110 (B) Amino acid sequence map of Edc3, emphasizing regions rich in charged residues: the PA and PAM.
1111 The annotation of charged amino acids and the color scheme for the sequences were applied as in
1112 Supplementary Figure 1B. In the full-length amino acid sequence, the PA region is indicated in green, the
1113 PAM region in red, and the APD region in blue.

1114 (C-D) Graphical analysis and plotting were performed using GraphPad Prism 5.

1115 (C) Computational prediction of Intrinsically Disordered Regions (IDRs) in Edc3 using a suite of
1116 bioinformatics tools: PASTA 2.0 (green), IUPred2A (pink), Disopred3 (yellow), and PrDOS (purple). IDRs
1117 were defined as regions where all four algorithms consistently predicted disorder scores exceeding 0.5.
1118 The PAM and PA regions are demarcated by red and green boxes, respectively.

1119 (D) Identification of Aggregation Prone Domains (APDs) in Edc3 through analysis with PASTA 2.0 (blue)
1120 and Aggrescan (red). Regions displaying elevated positive scores were classified as APDs, highlighted by
1121 blue boxes.

1122 (E) The density of charged amino acids along the Edc3 sequence was analyzed using a sliding window
1123 approach. The detailed method is the same as described in Supplementary Figure 1E. The red and green
1124 boxes indicate the PAM and PA regions, respectively.

Supplementary Figure 3

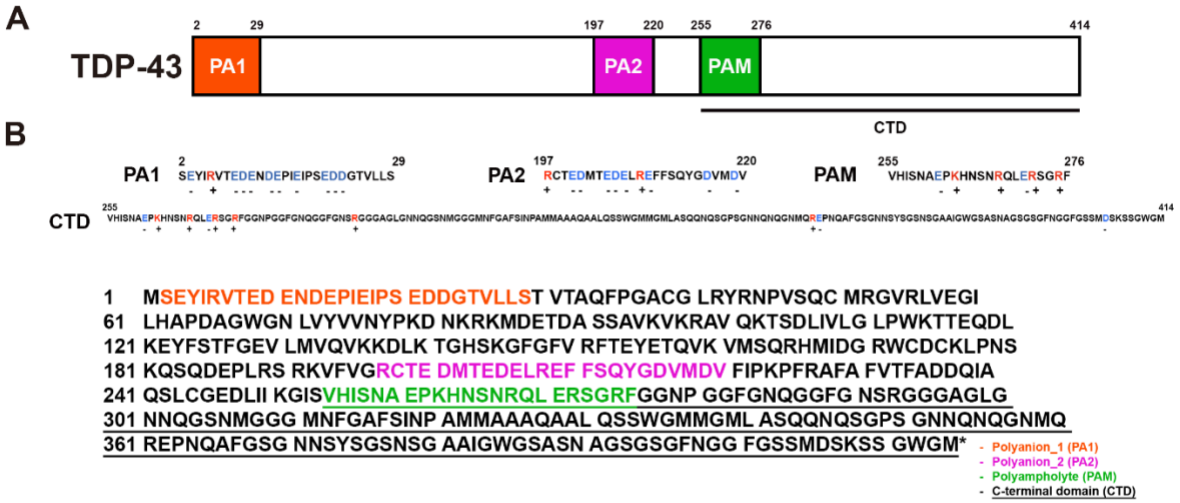

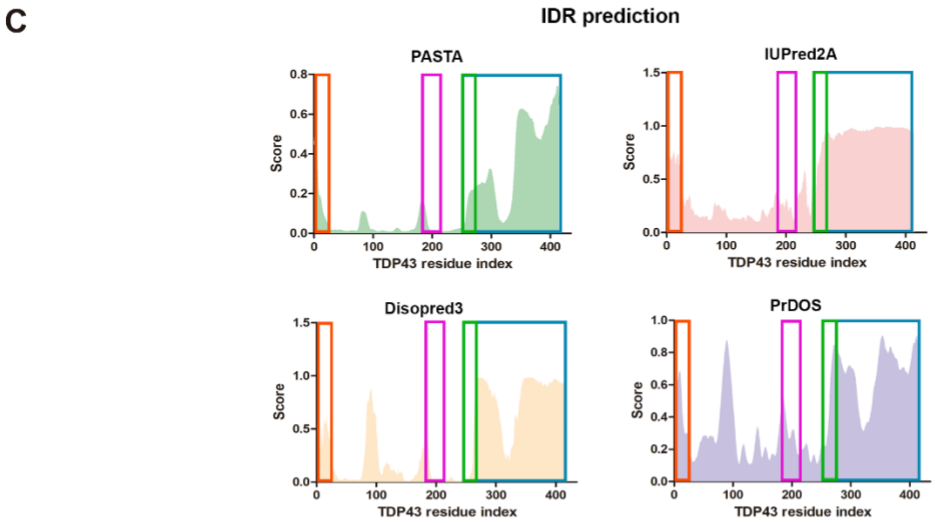

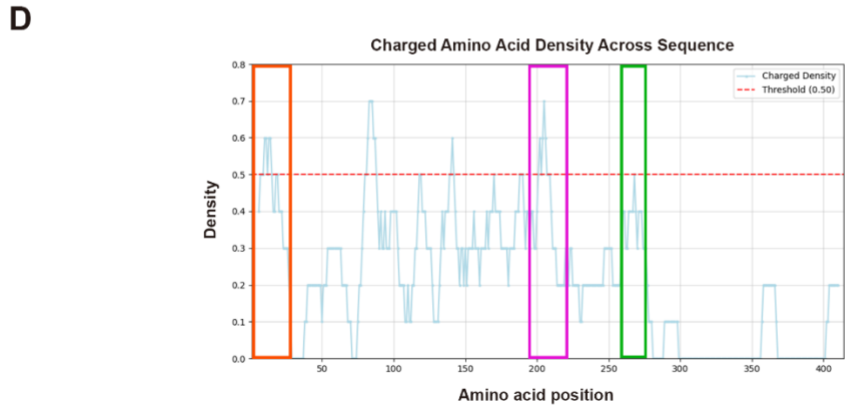

1125

1126 (A) A scheme of domain prediction of TDP-43. The CTD region, comprising residues 255–414, is depicted
1127 as a black line. The PA1 (2-29), PA2 (197-220), and PAM (255-276) regions are shown in red, pink, and
1128 green, respectively.

1129 (B) Amino acid sequence of TDP-43, highlighting the charged amino acid clusters (PA1, PA2 and PAM)
1130 and CTD. The annotation of charged amino acids was implemented in accordance with Supplementary
1131 Figure 1B. Each domain was indicated using the same box colors as in A, and the CTD is denoted with an
1132 underline.

1133 (C) Graphical representations were created and analyzed with GraphPad Prism 5. Computational analysis
1134 of Intrinsically Disordered Regions (IDRs) within TDP-43 employing multiple bioinformatics algorithms:
1135 PASTA 2.0 (green), IUPred2A (pink), Disopred3 (yellow), and PrDOS (purple). IDRs were defined as
1136 regions with disorder propensity scores above 0.2 and a high proportion of charged amino acids. The PA1
1137 region is indicated by red boxes, and the PA2 region is indicated by pink boxes. The PAM region is indicated
1138 by green box, and the CTD is indicated by blue box.

1139 (D) The density of charged amino acids along the TDP-43 sequence was analyzed using a sliding window
1140 approach. The detailed method is the same as described in Supplementary Figure 1E. The PA1 region and
1141 the PA2 region is indicated by red box and pink box, respectively, while the PAM region is indicated by
1142 green box.

Supplementary Figure 4

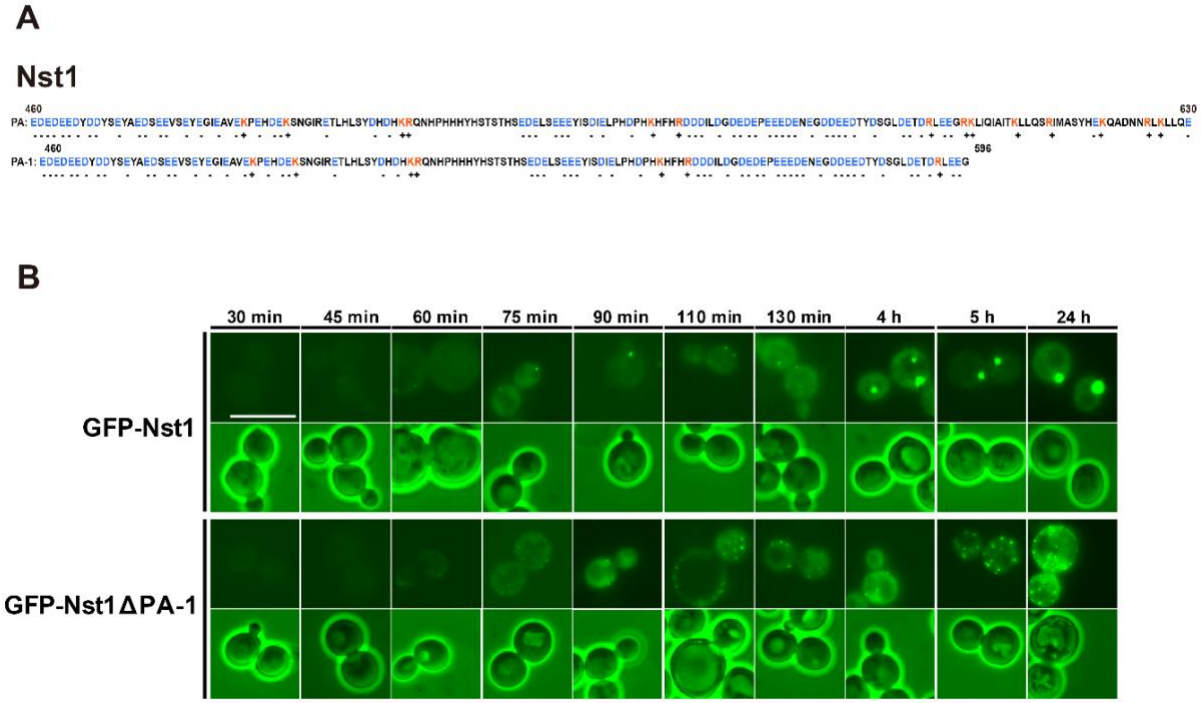

1144 (A) Sequence of PA and PA-1 domains in Nst1

1145 (B) Fluorescence microscopy images showing the formation of condensates by GFP-tagged Nst1 and
1146 Nst1ΔPA-1 in *Δnst1* (YSK3490) cells after GAL-induction. Images were acquired at the indicated time point
1147 following galactose induction. Scale bar: 10 μm.

Supplementary Figure 5

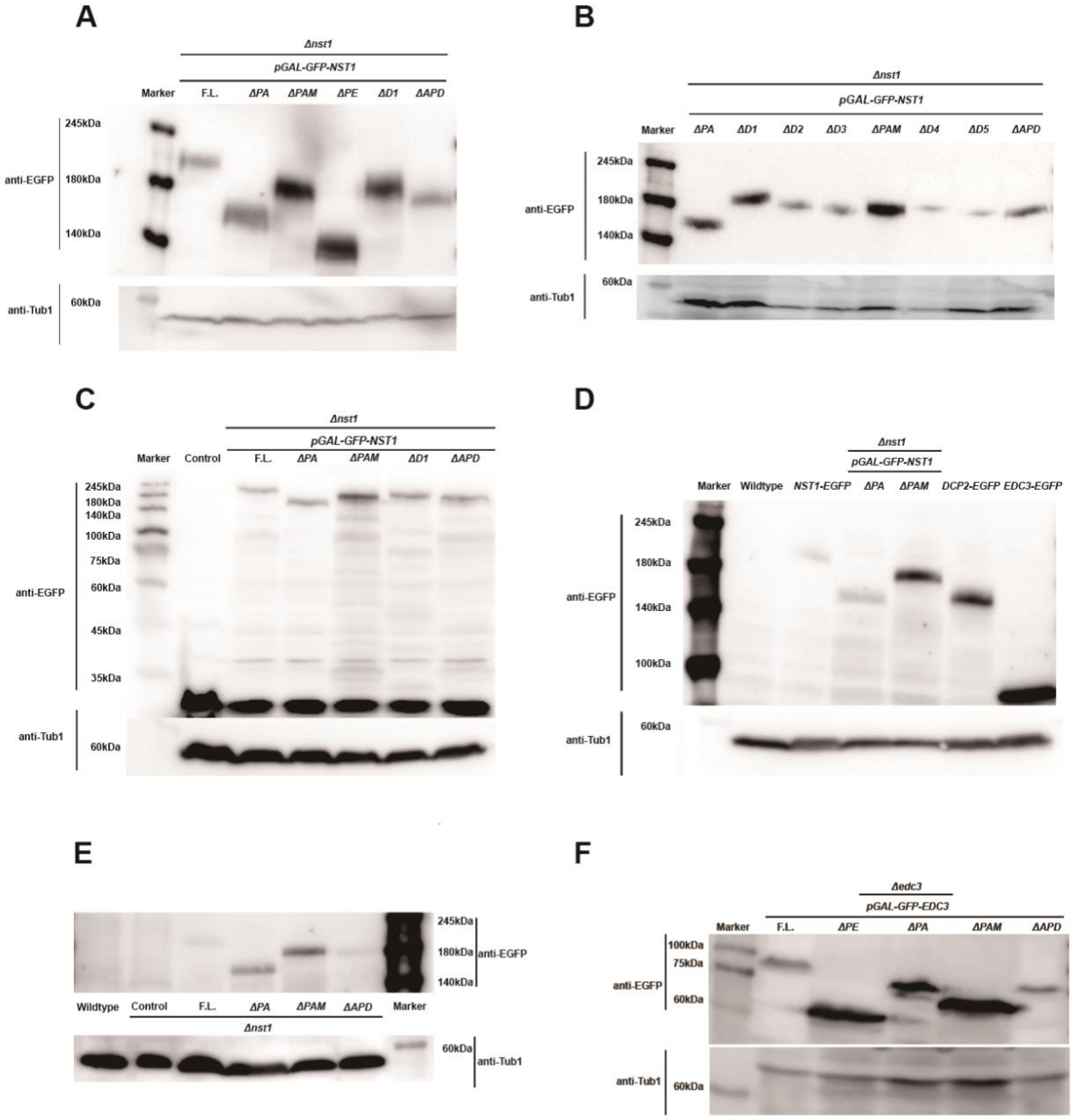

1148

Supplementary Figure 5

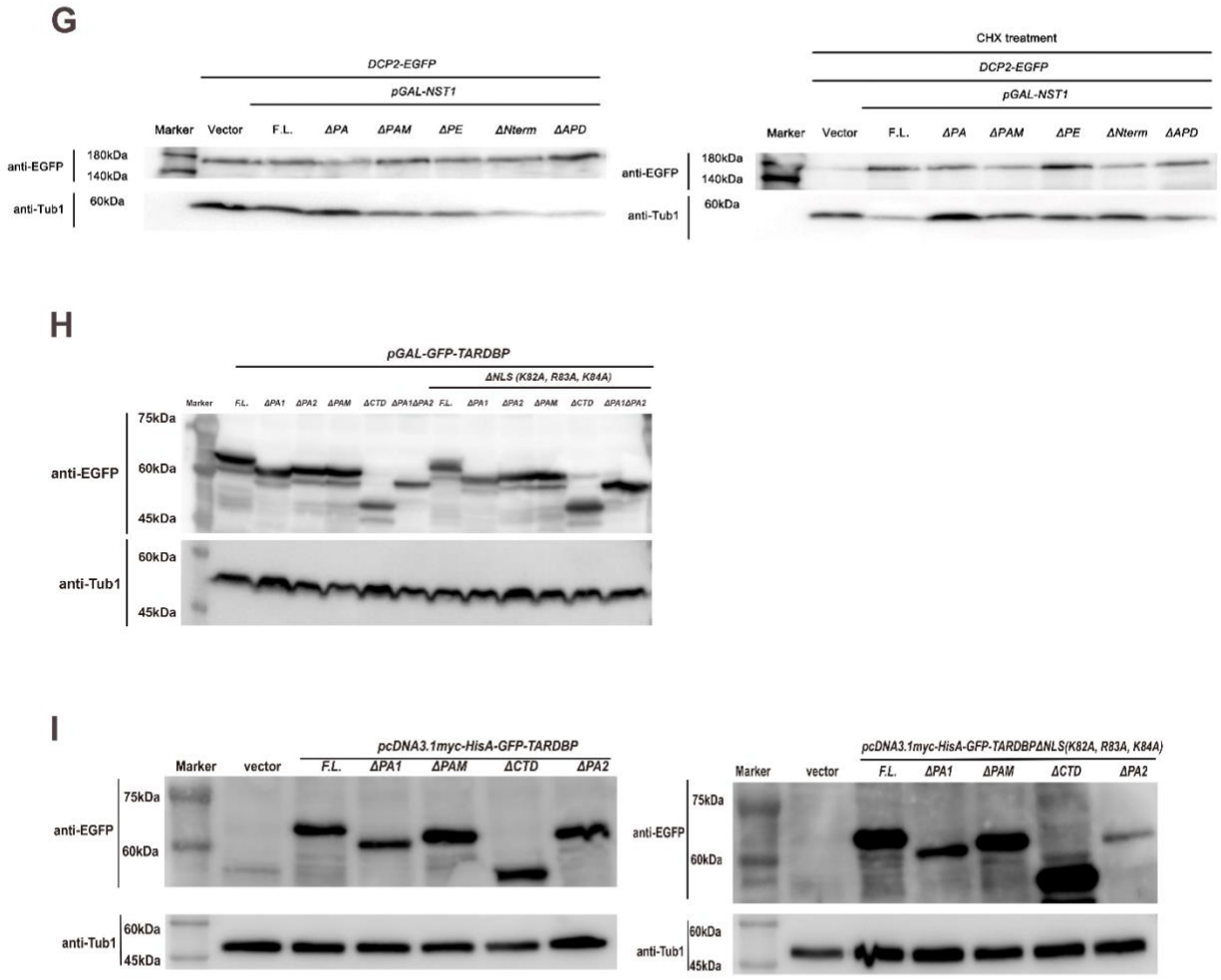

1149

1150 (A–B) Western blot analysis confirming the overexpression for GFP-tagged Nst1 domain deletion mutants,
1151 as shown in Figures 2C and 3B. Anti-GFP (600-101-215, Rockland) and anti-Tub1 (T5168, Sigma)
1152 antibodies were used to detect GFP-tagged fusion proteins and the Tub1 housekeeping protein,
1153 respectively.

1154 (A) The predicted molecular weights for Nst1 full-length, Nst1ΔPA, Nst1ΔPAM, Nst1ΔPE, Nst1ΔD1,
1155 Nst1ΔAPD, and Tub1 are 168.3 kDa, 148.1 kDa, 152.3 kDa, 132.1 kDa, 154.4 kDa, 144.1 kDa, and 49.8
1156 kDa, respectively.

1157 (B) The predicted molecular weights for Nst1 full-length, Nst1ΔPA, Nst1ΔD1, Nst1ΔD2, Nst1ΔD3,
1158 Nst1ΔPAM, Nst1ΔD4, Nst1ΔD5, Nst1ΔAPD, and Tub1 are 148.1 kDa, 154.4 kDa, 148.7 kDa, 149.6 kDa,
1159 152.3 kDa, 158.1 kDa, 149.9 kDa, 144.1 kDa, and 49.8 kDa, respectively.

1160 (C) Western blot verification of the overexpression of GFP-tagged Nst1 domain deletion mutants for FRAP
1161 analysis, as shown in Figure 4A. The predicted molecular weights for GFP (vector control), Nst1 full-length,
1162 Nst1ΔPA, Nst1ΔPAM, Nst1ΔD1, Nst1ΔAPD, and Tub1 are 26.8 kDa, 168.3 kDa, 148.1 kDa, 152.3 kDa,
1163 154.4 kDa, 144.1 kDa, and 49.8 kDa, respectively.

1164 (D) Western blot analysis verifying protein expression prior to RNase inhibitor treatment, as shown in
1165 Figures 5G and 5I. The predicted molecular weights for Nst1-EGFP, Nst1ΔPA, Nst1ΔPAM, Dcp2-EGFP,
1166 Edc3-EGFP, and Tub1 are 168.3 kDa, 148.1 kDa, 152.3 kDa, 137.2 kDa, 88.1 kDa, and 49.8 kDa,
1167 respectively.

1168 (E) Western blot analysis confirming endogenous expression of GFP-tagged Nst1 full-length and deletion
1169 mutants (ΔPA, ΔPAM, ΔAPD) in log-phase Δ*nst1* (YSK3490) cells, as shown in Figure 2H. Tub1 served as
1170 a loading control. The predicted molecular weights are: Nst1 full-length, 168.3 kDa; Nst1ΔPA, 148.1 kDa;
1171 Nst1ΔPAM, 152.3 kDa; Nst1ΔAPD, 144.1 kDa; Tub1, 49.8 kDa.

1172 (F) Western blot confirmation of the overexpression of GFP-tagged Edc3 domain deletion mutants, as
1173 shown in Figure 6B. The predicted molecular weights for Edc3 full-length, Edc3ΔPE, Edc3ΔPA,
1174 Edc3ΔPAM, Edc3ΔAPD, and Tub1 are 88.1 kDa, 71.2 kDa, 85.2 kDa, 74.2 kDa, 82.6 kDa, and 49.8 kDa,
1175 respectively.

1176 (G) Western blot analysis of Dcp2-EGFP (135.5 kDa) expression and Tub1 (49.8 kDa, loading control) in
1177 yeast cells used in Figure 5E. Cells were either untreated or treated with cycloheximide (CHX).

1178 (H) Western blot confirmation of the overexpression of GFP-tagged TDP-43 domain deletion mutants in
1179 budding yeast, as shown in Figure 6D. Constructs with intact nuclear localization signal (NLS) and
1180 corresponding NLS-deletion variants were analyzed. The predicted molecular weights are: TDP-43 full-
1181 length, 71.3 kDa; TDP-43ΔPA1, 68.1 kDa; TDP-43ΔPA2, 68.4 kDa; TDP-43ΔPAM, 68.7 kDa; TDP-
1182 43ΔCTD, 55.4 kDa. For NLS-deleted constructs: TDP-43ΔNLS full-length, 71.1 kDa; TDP-43ΔNLSΔPA1,
1183 67.9 kDa; TDP-43ΔNLSΔPA2, 68.2 kDa; TDP-43ΔNLSΔPAM, 68.5 kDa; TDP-43ΔNLSΔCTD, 55.2 kDa.
1184 Tub1 served as a loading control (49.8 kDa).

1185 (I) Western blot analysis of pcDNAmyc-hisA-GFP-*TARDBP* constructs expressed in U2OS cells, as shown
1186 in Figure 6E. Both NLS-intact and NLS-deleted variants were examined. The predicted molecular weights
1187 are: TDP-43 full-length, 71.3 kDa; TDP-43ΔPA1, 68.1 kDa; TDP-43ΔPA2, 68.4 kDa; TDP-43ΔPAM, 68.7
1188 kDa; TDP-43ΔCTD, 55.4 kDa. For NLS-deleted constructs: TDP-43ΔNLS full-length, 71.1 kDa; TDP-
1189 43ΔNLSΔPA1, 67.9 kDa; TDP-43ΔNLSΔPA2, 68.2 kDa; TDP-43ΔNLSΔPAM, 68.5 kDa; TDP-
1190 43ΔNLSΔCTD, 55.2 kDa. Tub1 served as a loading control (49.8 kDa).

Supplementary Figure 6

A Nst1

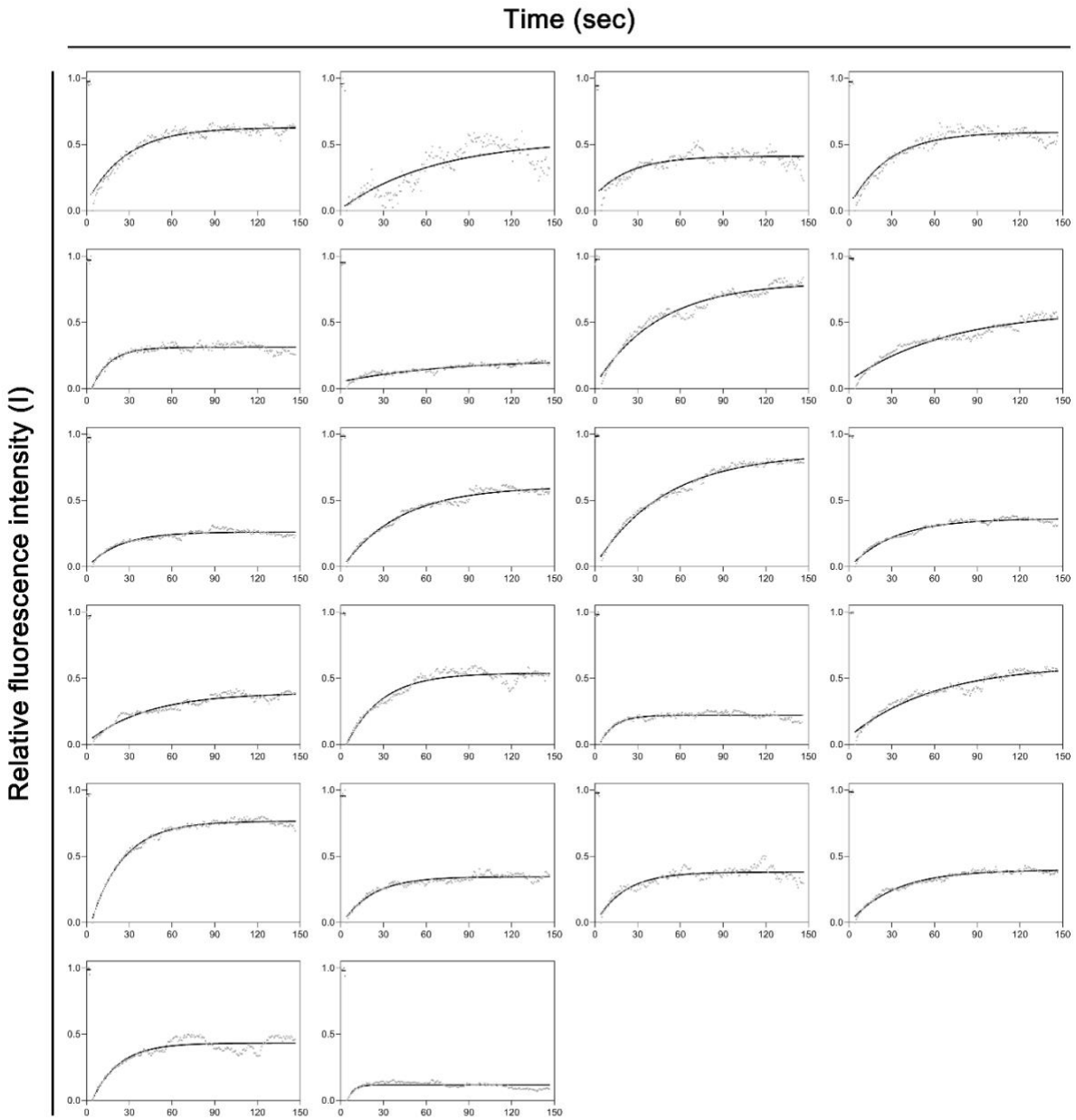

1191

Supplementary Figure 6

B Nst1ΔPA

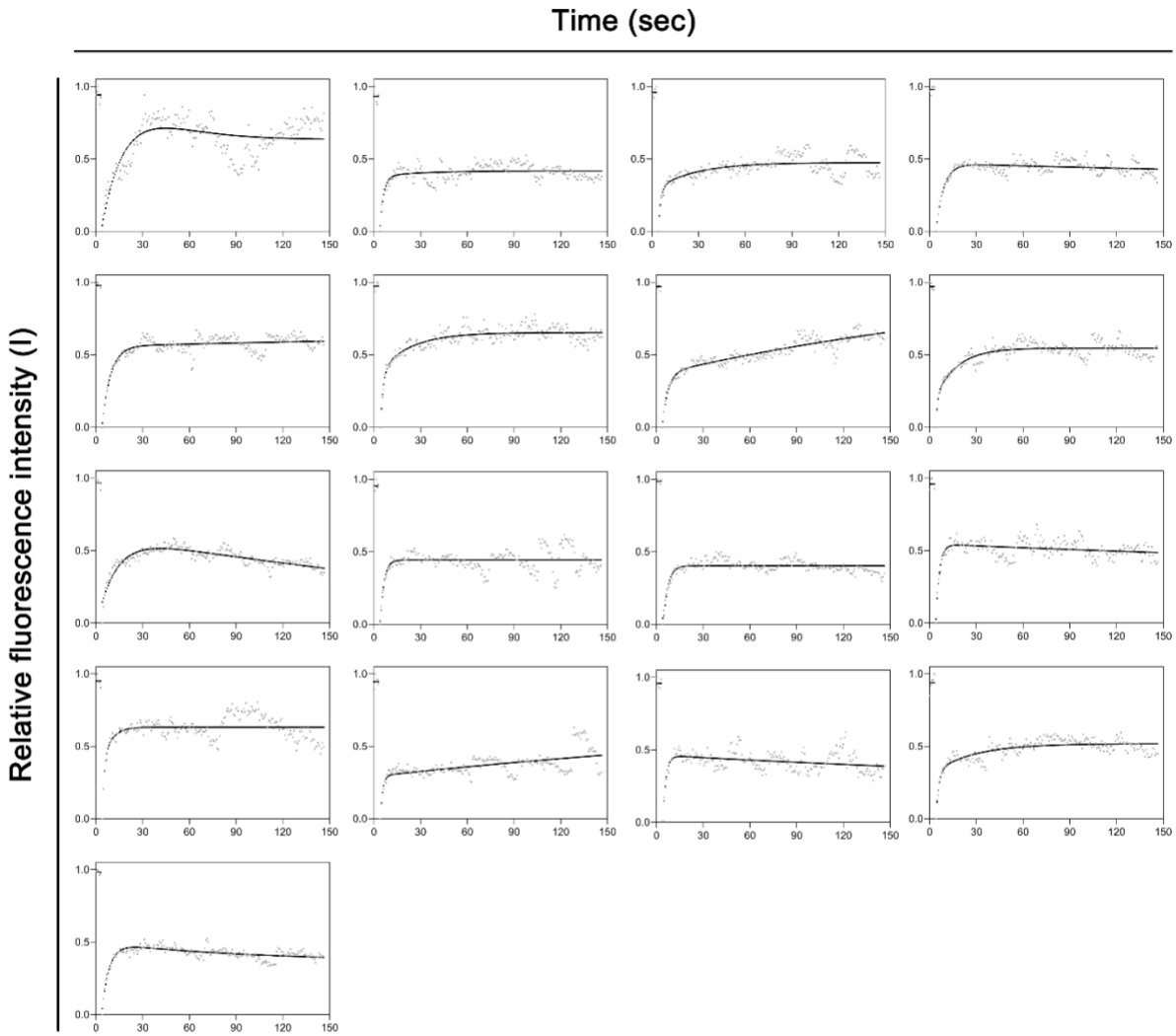

1192

Supplementary Figure 6

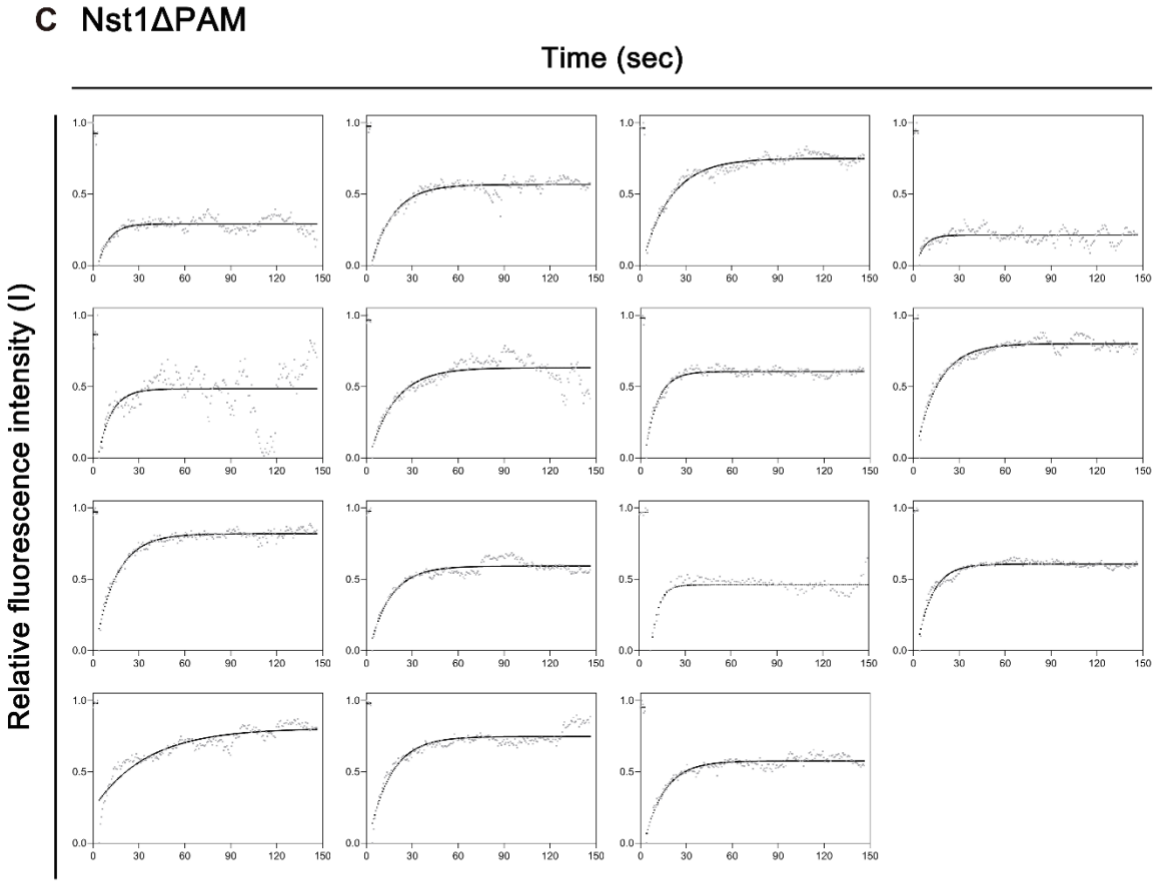

1193

Supplementary Figure 6

D Nst1ΔD1

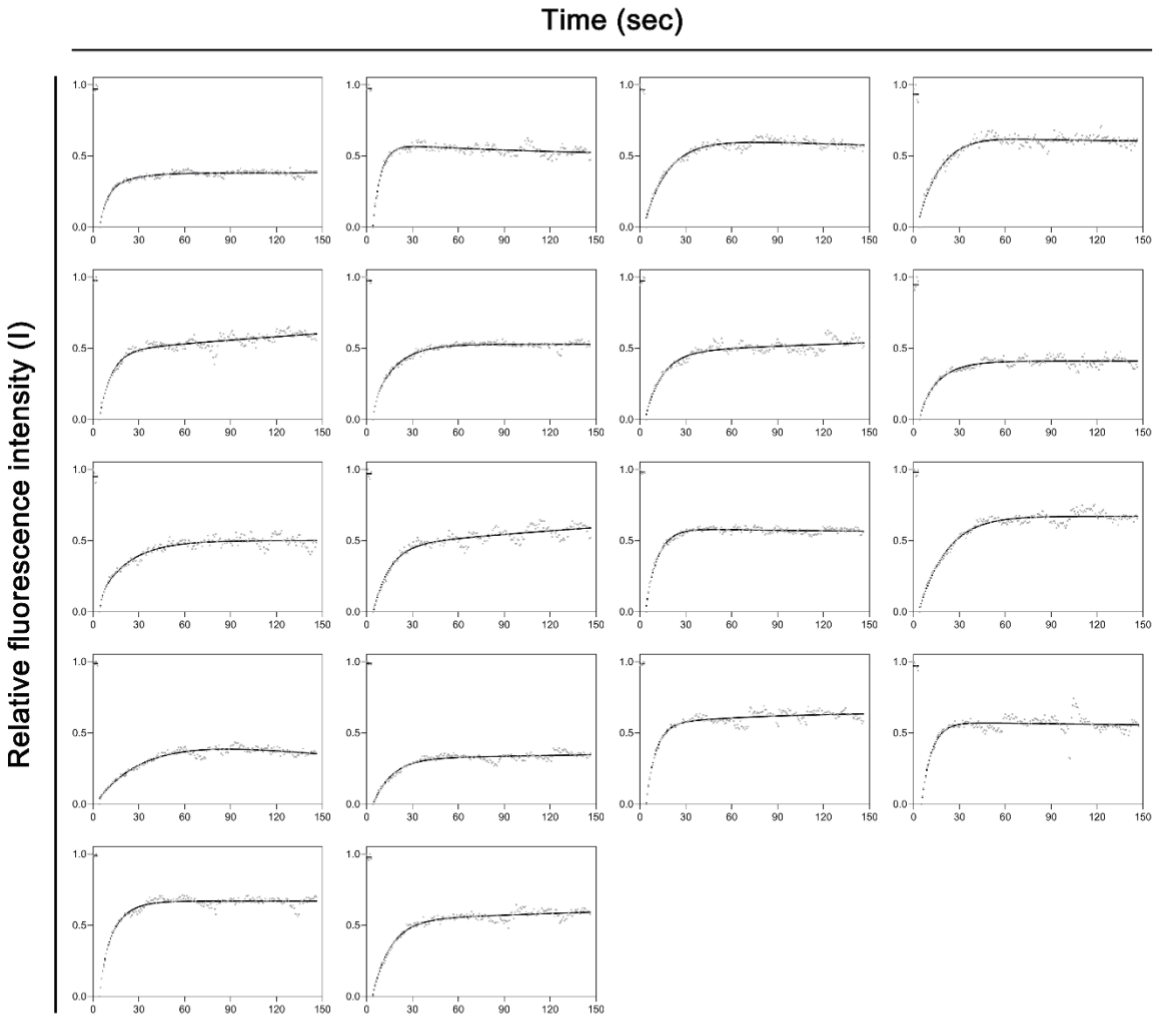

1194

Supplementary Figure 6

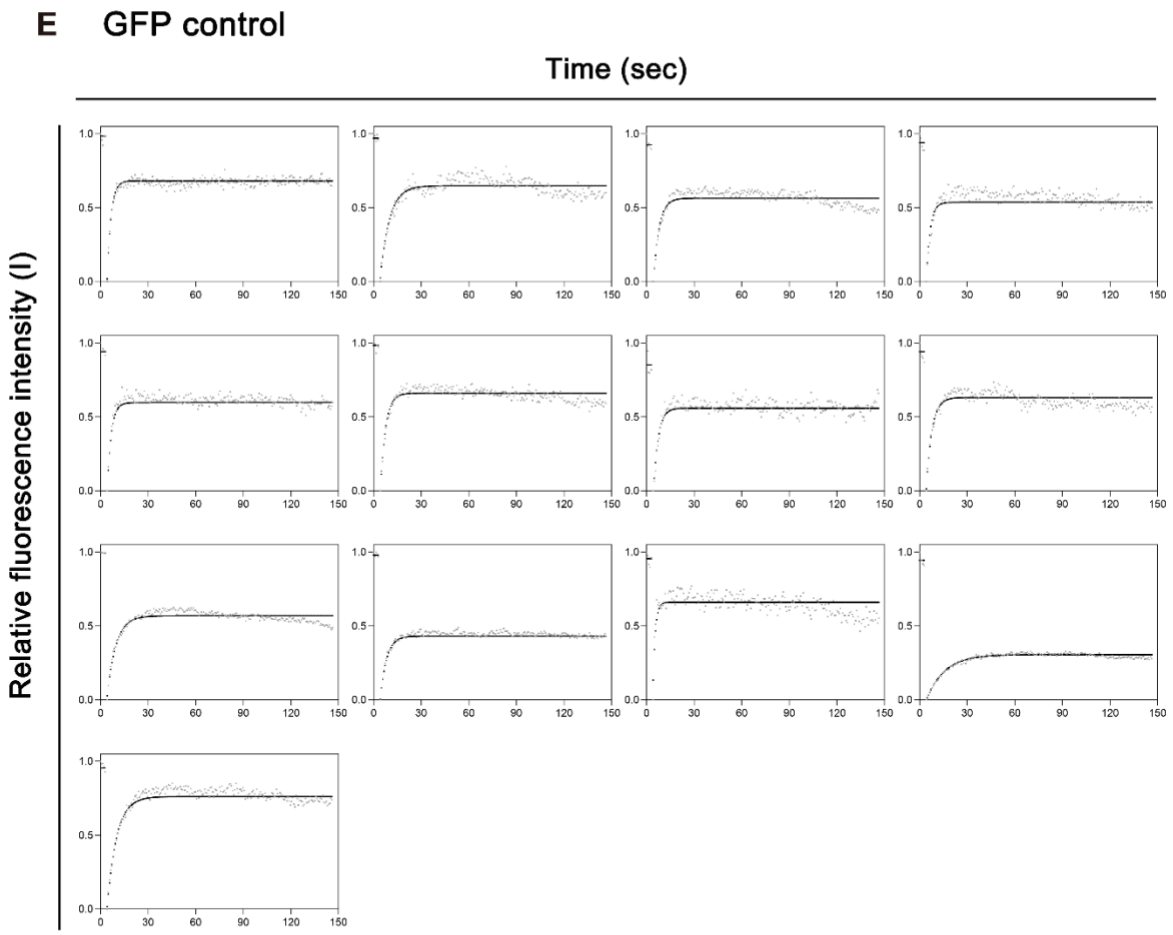

1195

Supplementary Figure 7

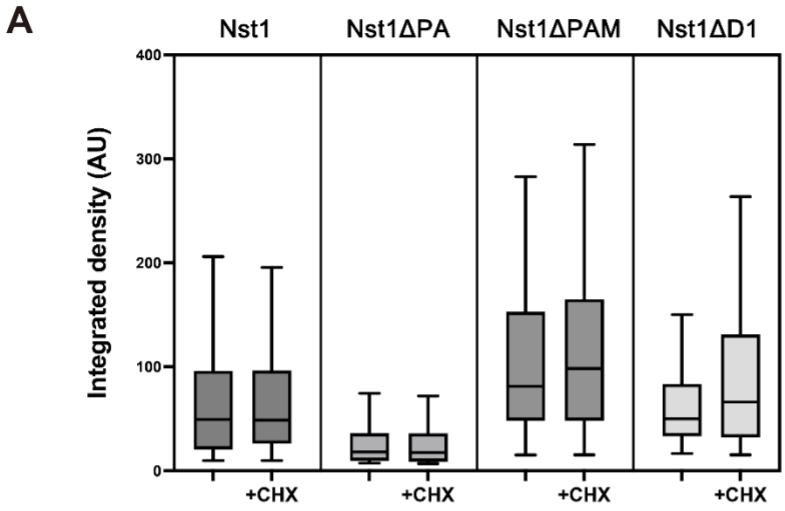

1196

1197 (A) Box plot of condensate formation, measured by integrated fluorescence intensity (Integrated Density),
1198 for condensates generated by galactose-induced, GFP-tagged Nst1, Nst1ΔPA, Nst1ΔPAM, and Nst1ΔD1
1199 before and after CHX treatment. Fluorescence microscopy images were analyzed using Fiji (ImageJ) to
1200 quantify the integrated density of condensates. Data from more than 100 cells per condition were visualized
1201 using GraphPad Prism 10.

Supplementary Figure 8

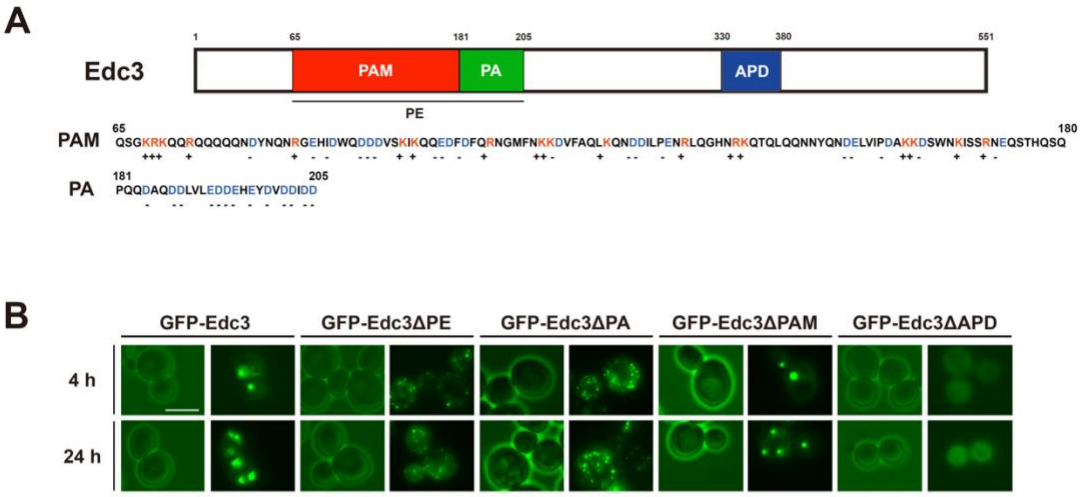

1203 (A) Schematic representation of Edc3 domain architecture. The region spanning residues 65–205 was
1204 predicted to be the PE domain using a sliding window approach and various IDR prediction tools. See also
1205 Supplementary figure 2. The region from 330–380 was identified as the APD domain based on PASTA and
1206 Aggrescan analyses. The PE domain of Edc3 was further characterized according to its charge distribution:
1207 residues 181–205 exhibited a high density of negative charges and were thus designated as the PA domain.
1208 The remaining portion of the PE segment, encompassing residues 65–180 and containing a relatively
1209 balanced proportion of positively and negatively charged amino acids, was defined as the PAM domain.
1210 The charged amino acids in the charge-rich PAM and PA sequences were annotated as described in Figure
1211 1D.

1212 (B) Fluorescence microscopy images showing condensate formation upon overexpression of Edc3,
1213 Edc3ΔPE, Edc3ΔPA, Edc3ΔPAM, and Edc3ΔAPD in *Δedc3* cells (YSK3707). Condensate formation for
1214 each Edc3 variant was imaged after 4 and 24 hours of galactose induction. For each strain and time point,
1215 representative images were selected from examinations of at least 100 cells.

Supplementary Figure 9

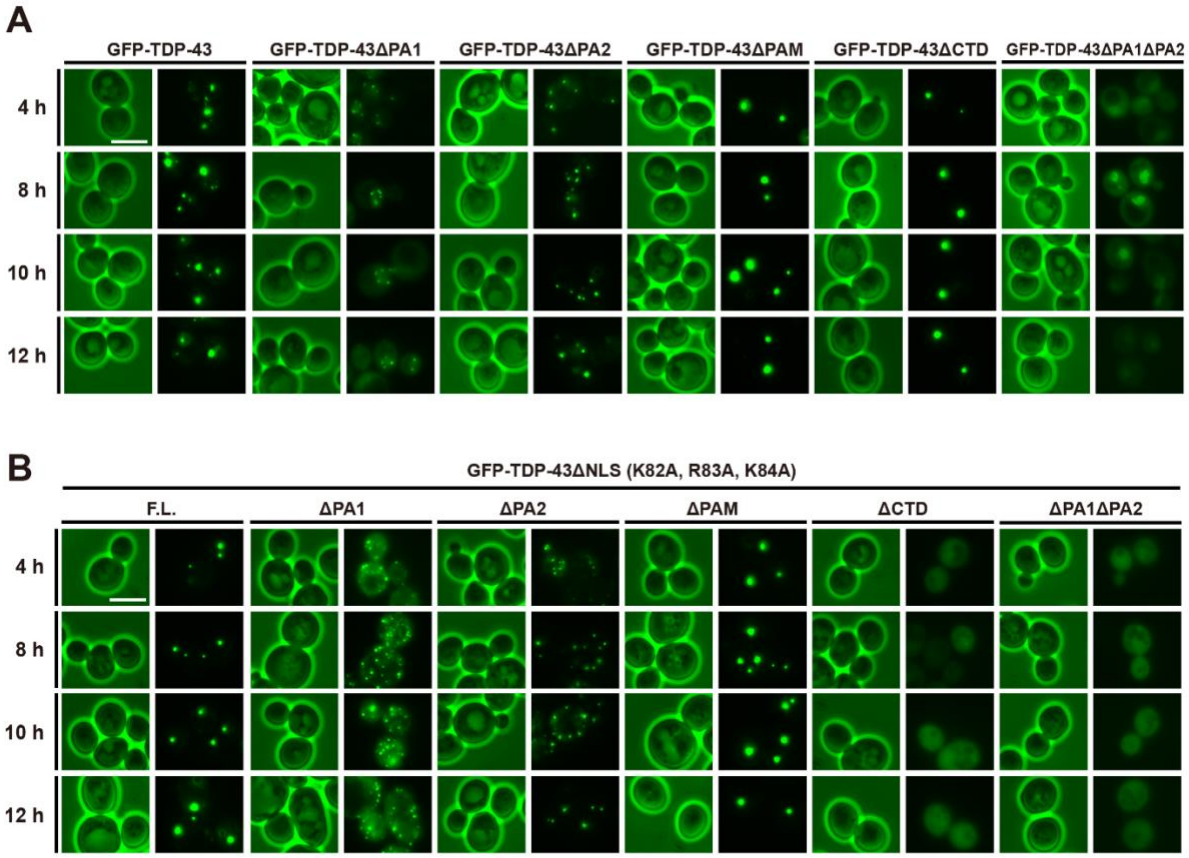

1216

1217 (A-B) Fluorescence microscopy images of budding yeast (W303a) cells after 4, 8, 10, 12 hours of
1218 overexpression of TDP-43 and its domain deletion mutants (ΔPA1, ΔPA2, ΔPAM, ΔCTD and ΔPA1ΔPA2)
1219 with or without NLS (Nuclear localization signal) sequence under a galactose-inducible promoter. Scale
1220 bar: 5 μm.